Technical University of Crete

School of Production Engineering and Management

Investigation of particles deposition on gas turbine blades

---

by

Gousopoulos Fotios

Diploma Thesis

Supervisor: Prof. Dr. Ioannis K. Nikolos

Chania, July 2019

Technical University of Crete

School of Production Engineering and Management

Investigation of particles deposition on gas turbine blades

by

Gousopoulos Fotios

Approved by:

Dr. Ioannis K. Nikolos
Professor
Technical University of Crete
School of Production Engineering
& Management

Dr. Anargyros I. Delis
Associate Professor
Technical University of Crete
School of Production Engineering
& Management

Dr. Georgios Arampatzis
Assistant Professor
Technical University of Crete
School of Production Engineering
& Management

Chania, July 2019

Acknowledgements

The conclusion of this diploma thesis is completing the cycle of my undergraduate studies. I would like to express my gratitude to my supervisor Professor I.K. Nikolos, for his excellent leadership, his ideas and his willingness to help in any difficulty occurred. I would also like to express my gratitude to the PhD candidate Leloudas Stavros and MSc student Igglezakis Dimitrios, for their help with technical and theoretical problems that arose. Also, to all the lab-mates, for all the fun during the last year.

Finally, I owe the greatest thanks to my family and the people who are close to me, for all the support they have been giving to me, each in its own way, all these years.

Table of Contents

List of Figures

List of Tables

Nomenclature

TIT	Turbine Inlet Temperature
Φ	Overall effectiveness
T_∞	Mainstream temperature
T_w	Surface temperature
T_c	Coolant temperature
H	Adiabatic effectiveness
T_{aw}	Adiabatic wall temperature
M	Blowing ratio
TBC	Thermal Barrier Coating
HPT	High Pressure Turbine
I	Momentum flux ratio
k^+	Dimensionless roughness parameter
k_s	Sandgrain diameter
u_T	Shear velocity
Y	Kinematic velocity
Re_{ks}	Roughness Reynolds number
Re_{ks}	Momentum thickness Reynolds number
Tu	Turbulence intensity
Λ_s	Roughness density parameter
S	Surface area without roughness
S_f	Total frontal surface area
A_f	Roughness element frontal area
A_s	Roughness element windward wetted area
P_{tm}	Mainflow total pressure
P_{tc}	Cooling flow total pressure
T_{tm}	Mainflow total temperature
T_{tc}	Cooling flow total temperature
DR	Density ratio
ρ_m	Mainflow density
ρ_c	Cooling flow density
Ma_m	Mainflow Mach number
Ma_c	Cooling flow Mach number
BPR	Bypass ratio
FPR	Fan's pressure ratio
HPC	High pressure compressor
HPT	High pressure turbine
MB	Main burner
OPR	Overall pressure ratio
Π	Pressure ratio
η_{hp}	High pressure turbine efficiency
η_{fan}	Fan efficiency
$T_{rec,m}$	Mainflow recovery temperature

Abstract

Turbine blades' wear is a frequent phenomenon, mainly because of the high temperatures occurring in that area (temperatures above the melting point of any metal used to make the blades), usually combined with mechanical fatigue, due to increased operating speeds of the corresponding rotors. Frequently, however, the phenomenon of premature (in some cases before 50% of the expected operating limit) irreversible wear is observed, which obviously entails considerable cost, both economically and operationally (when referred to aircraft engines or gas turbines). This phenomenon, the initial wear of the outer, usually ceramic, surface and the subsequent wear of the blade metal itself, is called erosion and its study is the purpose of this diploma thesis.

Numerous bibliographic references associate the erosion formation with the deposition of particles, transported through the air compressed by the engine, into the blades and coming either from the outside environment (dust, salt, etc.) or from the engine environment itself (combustion defects, lubricants etc.). In the first part, the mechanisms of erosion formation are presented, along with methods to prevent and partially address the phenomenon, as reflected in various bibliographical references.

In the second part, flow analysis of a typical fan-shaped cooling hole, with the use of CFD, is performed. This study is carried out for various blowing ratios, for the purpose of obtaining a more detailed view of the cooling system behavior. Afterward, a comparison of the obtained results with other similar simulation or experimental results is performed for validation purposes.

Περίληψη

Η φθορά των πτερυγίων στροβίλου είναι ένα φαινόμενο συχνό, κυρίως λόγω των υψηλών θερμοκρασιών του καυσαερίου σε εκείνη την περιοχή του κινητήρα (θερμοκρασίες υψηλότερες απο το σημείο τήξης οποιουδήποτε μετάλλου χρησιμοποιείται για την κατασκευή πτερυγίων), που συνήθως συνδυάζεται με υψηλή μηχανική κόπωση λόγω των αυξημένων στροφών λειτουργίας των περιστρεφόμενων πτερυγώσεων. Πολλές φορές παρατηρείται όμως το φαινόμενο της κατά πολύ πρόωρης (σε ορισμένες περιπτώσεις πριν συμπληρωθεί το 50% του προβλεπόμενου ορίου λειτουργίας), μη αναστρέψιμης φθοράς, που όπως είναι προφανές επιφέρει υψηλό κόστος και απο οικονομικής άποψης αλλά και απο τη πλευρά της επιχειρησιακής διαθεσιμότητας (όταν αναφερόμαστε σε κινητήρες αεροσκαφών ή επίγειους αεριοστροβίλους). Το φαινόμενο αυτό της φθοράς, πρώτα της εξωτερικής, συνήθως κεραμικής επιφάνειας, και αργότερα του ίδιου του μετάλλου των πτερυγίων, ονομάζεται διάβρωση και σκοπός της παρούσας διπλωματικής εργασίας είναι η μελέτη του.

Πληθώρα βιβλιογραφικών αναφορών συσχετίζουν τη δημιουργία διαβρώσεως με την επικάθιση σωματιδίων, που μεταφέρονται μέσω του αέρα που συμπιέζεται απο τον κινητήρα στα πτερύγια και προέρχονται είτε απο το εξωτερικό περιβάλλον (σκόνη, αλάτι, κλπ.), είτε από το ίδιο το περιβάλλον του κινητήρα (ατέλειες καύσης, λιπαντικά, κ.λπ.). Στο πρώτο μέρος της παρούσας εργασίας παρουσιάζονται οι μηχανισμοί δημιουργίας της διαβρώσεως, αλλά και τρόποι πρόληψης και μερικής αντιμετώπισης του φαινομένου, όπως έχουν αποτυπωθεί απο διάφορες βιβλιογραφικές αναφορές.

Στο δεύτερο μέρος, πραγματοποιείται η ανάλυση της ροής σε μια τυπική οπή ψύξης πτερυγίου στροβίλου (fan – shaped cooling hole) με χρήση λογισμικού υπολογιστικής ρευστοδυναμικής (CFD). Η μελέτη αυτή διεξάγεται για διάφορους λόγους μέσων ταχυτήτων αέρα ψύξης - καυσαερίων (blowing ratios), με σκοπό την όσο λεπτομερέστερη παρατήρηση της συμπεριφοράς του συστήματος ψύξης. Στη συνέχεια, πραγματοποιείται σύγκριση των αποτελεσμάτων της μελέτης με προσομοιώσεις και πειραματικά αποτελέσματα, ούτως ώστε να επιβεβαιωθεί η εγκυρότητα τους.

Chapter 1: Introduction

1.1 Introduction

Gas turbines are operated in various environments (sea, industry facilities, deserts, etc.) for different purposes (power generation, propulsion, etc.). By increasing the turbine inlet chamber temperature, an increase in engine power output can be achieved. Hence, one of the main goals of engineers is to have the highest Turbine Inlet Temperature (TIT) possible [Han, 2013]. In modern gas turbines, the inlet turbine temperature is way higher than the melting point of superalloys, used for their manufacture. For this reason, turbine blades with TBC (Thermal Barrier Coating) are utilized, which have ceramic coating on their outer surface [Han, 2013]. Moreover, cooling methods have been developed in order to extend the blades' life limits. The most common cooling method is film cooling, in which bleed air from the compressor flows through a cooling path to the internal of the blade and then is ejected through the cooling holes to the surface of the blade, creating a cooling layer (Fig. 1.1), [Han, 2013].
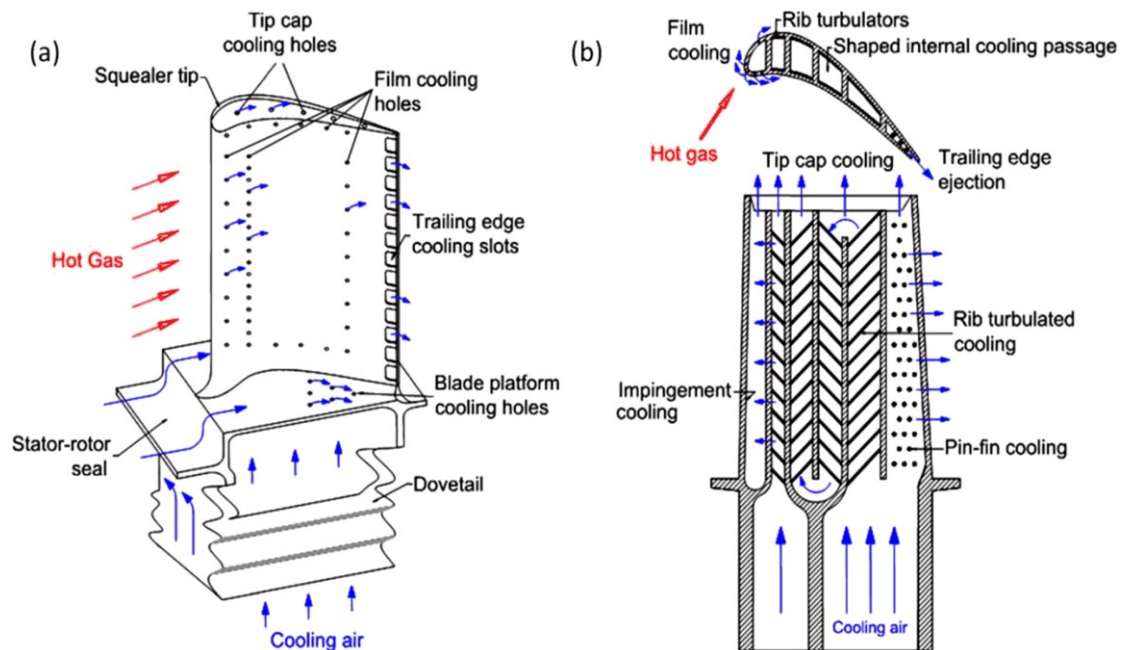
Fig. 1.1: *Blade cooling schematic: a) surface cooling, b) internal cooling [Han, 2013].*

As mentioned above, the various environments that engines are operated are sometimes harsh and aggressive, while the air ingested is many times "polluted" with particles, such as industrial pollutants, dust, salt, even volcanic ash [Yang, et al., 2014], [Wylie, et al., 2016]. Additionally, fuel combustion creates contaminants, which are also ingested into the gas main flow. The particles have the tendency to impact blades and transfer their kinetic energy, creating stress to the blades, and either deposit on the coating surface or continue their trajectory [Hamed, et al., 2004]. Sometimes, there are also chemical reactions taking place between the deposits and the coatings [Kurz, et al., 2000]. The ingestion phenomenon results in plugging of cooling holes, surface roughness increase, and eventually TBC degradation and blade erosion, which result in the reduction of turbine's life limits and the engine's performance [Suman, et al., 2016]. Examples of fouled blades can be seen in Figures 1.2, 1.3.

***Fig. 1.2:** Fouling due to deposition [Stalder, 2001].*

Fig. 1.3: *Fouling due to sand ingestion [Szczepankowski et al., 2017].*

Turbine blade erosion is an important issue, because of the resulting high maintenance cost and man-hours needed. No definite solution to the aforementioned problem has been proposed so far (for example a blade which is not susceptible to particle deposition), therefore the "solution" to the problem is prevention. The most common ways of diminishing the effects of such depositions are **air filtration** and **turbine cleaning** [Suman, et al., 2016].

1.2 Deposition resulting from environment ingested particles

Many studies have been published about particles ingested from the environment that gas turbines operate. Table 1.1, published in [Shi, et al., 2016], summarizes the size of various kinds of particles ingested by gas turbines.

In [Tabakoff, 1988], using the Cincinnati erosion wind tunnel, a test facility in which many turbine erosion tests have been conducted, supported that erosion rate increases with increasing flow temperatures, as well as the velocities of particles ingested. He also created a semi-empirical erosion equation, for predicting erosion rates. The graph in Fig. 1.4 confirms that temperature is very crucial to deposit formation. It can be seen that the net capture efficiency, which represents the quantity of particles deposited per time divided by the total amount of particles per hour added to the flow, increases exponentially with temperature rise. Impingement angles have also been proved very crucial to the increasing of erosion rate (maximum erosion values were noticed at 20 and 30 degrees impingement angle in Tabakoff's research).

Table 1.1: Size of particles ingested [Shi, et al., 2016].

Type	Particles Information	
	Type of particles	*Size (μm)*
F1	Ground-dust	1∼300
F2	Oil smokes	0.02∼1
F3	Fly ash	1∼200
F4	Salt particles in mist	Less than 10
F5	Smog	Less than 2
F6	Fume	Less than 1
F7	Clay	Less than 2
F8	Rosin smoke	0.01∼1
F9	Coal dust	1∼100
F10	Metallurgical dusts and fumes	0.001∼100
F11	Ammonium	0.1∼3
F12	Carbon black	0.01∼0.3
F13	Contact sulphuric mist	0.3∼3
F14	Paint pigments	0.1∼5
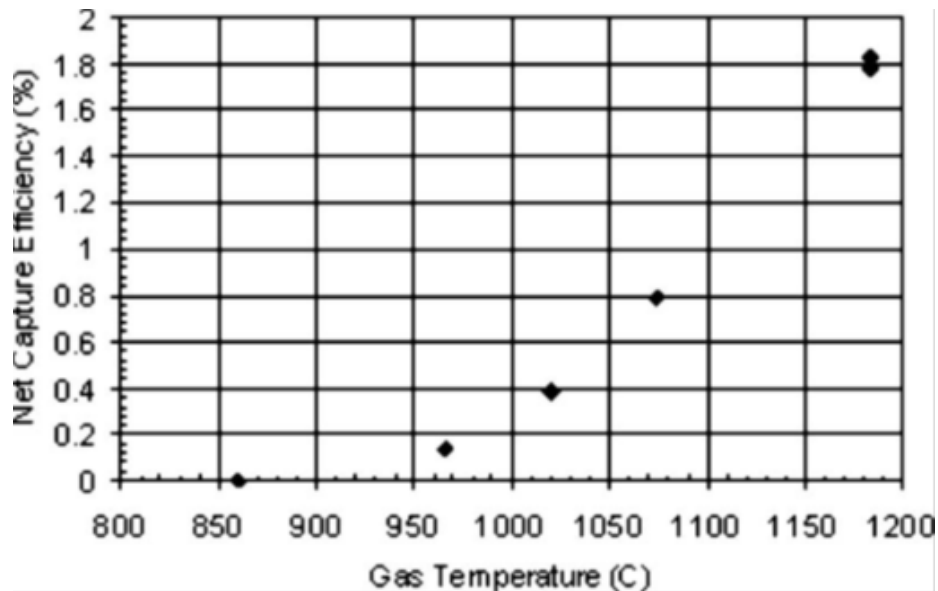
Fig. 1.4: Turbine gas temperature effect on net capture efficiency (net capture efficiency is the mg/h of deposit divided by mg/h of particulate added to the flow) [Crosby, et al., 2008].

One of the variables that define the effectiveness of a turbine blade is overall cooling effectiveness [Maikell, et al., 2011]

$$\varphi = \frac{T_\infty - T_w}{T_\infty - T_c} \tag{1}$$

where φ is overall effectiveness, T_∞ is mainstream temperature, T_w is surface temperature, and T_c is coolant temperature. Many experiments were based on the calculation of φ on various types of blades under specific conditions. Such is the example in [Maikell,et al., 2011], where they studied the leading edge of turbine blades by using non-TBC and TBC leading edge blades. A total of four blade leading edge samples, with single row cooling or three row cooling across the stagnation line, were used to calculate φ on a closed-loop wind tunnel, in different angles of attack (0 degrees to 5 degrees) and *Biot* number, matching the real engine conditions when operating (Bi=1.8). The results that emerged were the expected ones: the three row model had more increased φ than the single row model. Also, the angle of attack up to 5 degrees didn't seem to have any impact in TBC three row model performance. Another variable that is often examined in turbine blade studies, is [Maikell, et al., 2011]

$$\eta = \frac{T_\infty - T_{aw}}{T_\infty - T_c} \tag{2}$$

where η is adiabatic effectiveness, T_∞ is mainstream temperature, T_c is coolant temperature, and T_{aw} is adiabatic wall temperature. Murata et al. [Murata, et al., 2012] performed an experiment where they calculated η for various types of blade trailing edges, for different blowing ratios. The result was that up to M=1.5, η was increasing. For blowing ratios above 1.5, film cooling effectiveness increase was small.

A subject that concerns many engineers about deposition is the trajectories of the particles, as well as the quantity that gets melted and deposited. The areas that have the thickest deposits are the leading edge area and the pressure side. Hamed et al. [Hamed,et al., 2004], utilized the Cincinatti wind test facility and additionally conducted computational simulations. They found that in multistage turbines, smaller particles (30 microns) tend to impact the vane surface and then, due to the gas flow, impact the rotor blade suction side and then continue their trajectories. However, larger particles (1500 microns) impact the rotor blades area near leading edge,

resulting in bouncing back to the vanes trailing edge. In simple words, larger particles cause more impacts, therefore higher erosion and surface roughness rates (Fig. 1.5). However, even the smallest particles are prone to causing deposition, according to [Crosby, et al., 2008], who conducted a series of tests. This means that solutions like air filtration systems cannot entirely solve the problem.
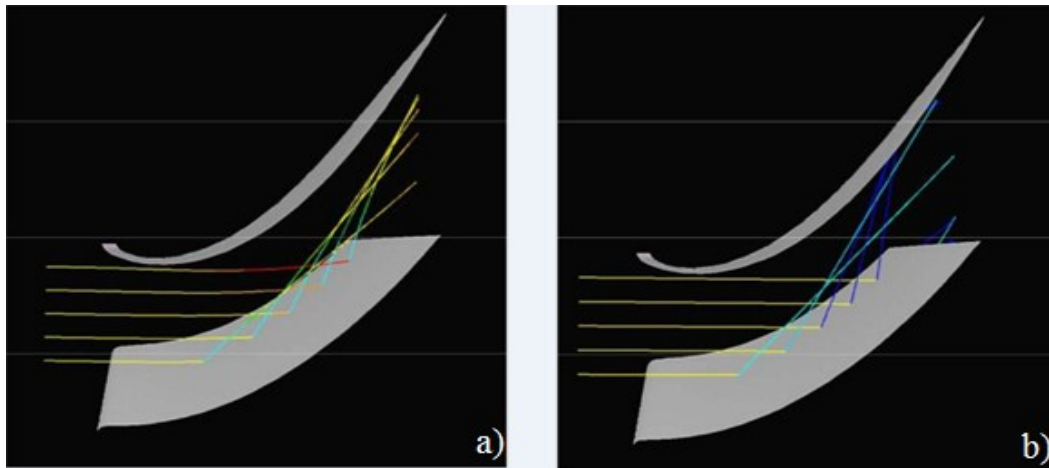
Fig. 1.5: *Vane impact trajectories, a) for small particles, b) for bigger particle) [Hamed,et al., 2004].*

Computational simulations were also conducted by [Ghenaiet, 2014], who performed a two stage axial turbine CFD simulation to compute ingested particle trajectories. He predicted erosion areas using a code similar to the Lagrangian tracking model along with the finite element method. The studied two-stage turbine was the one used on CF6-80A3 turbofan. The results of expected erosion rates are shown in Fig. 1.6 through Fig. 1.9.

Casari et al. [Casari, et al., 2017], noticed that the blade geometry changes because of the deposits accumulated on the surface, therefore the flow field was affected. Murugan et al. [Murugan, et al., 2017] observed that stator vanes had higher rate of deposition than rotor blades. Furthermore, they described sand particles' deposit mechanism: sand particles fully melt during the combustion, therefore most of their kinetic energy fades away. Consequently, they stick to the blade surface, causing deposition. The most important observation however, was that the bleed air used for internal cooling is also polluted with sand (Fig. 1.10).
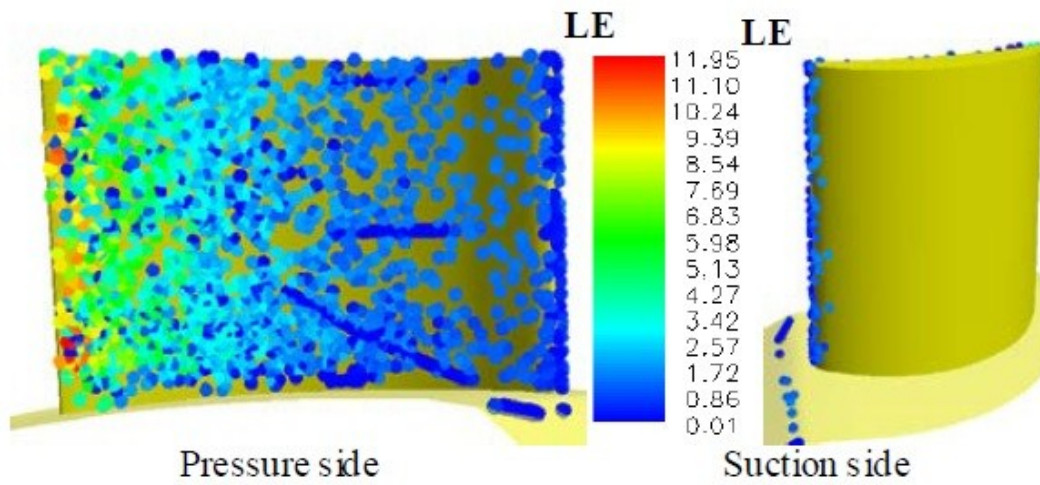
Fig. 1.6: *Sample of local erosion rates (mg/g) in 1ˢᵗ NGV [Ghenaiet, 2014].*
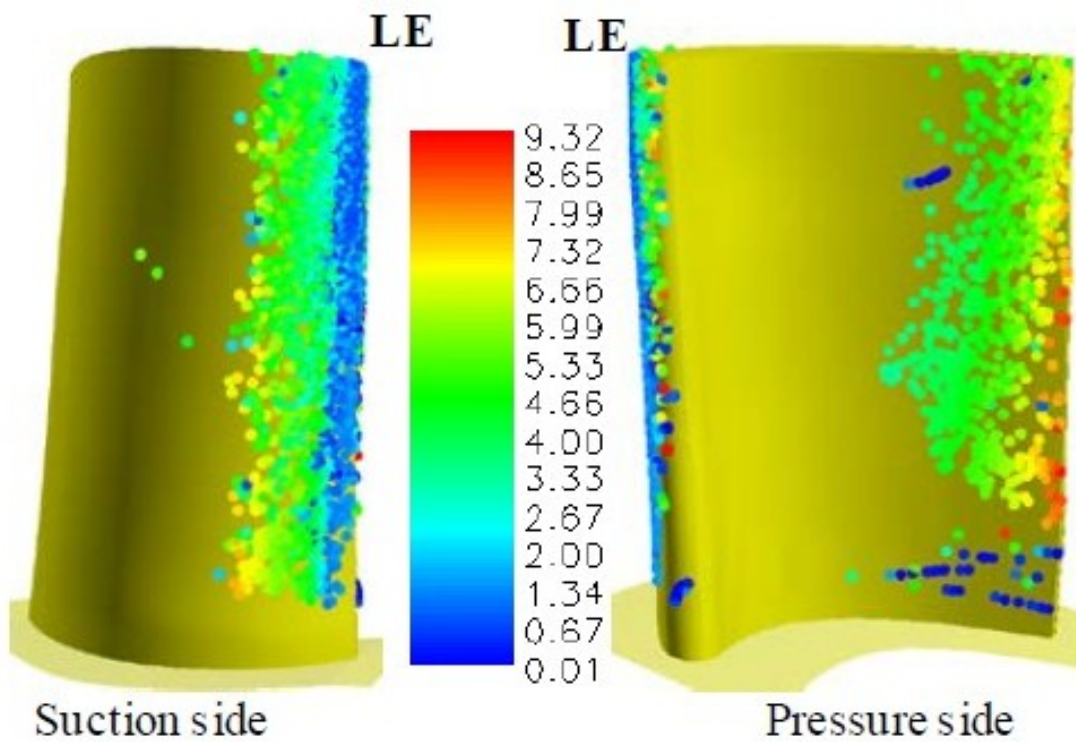
Fig. 1.7: *Sample of local erosion rates (mg/g) in 1ˢᵗ rotor [Ghenaiet, 2014].*
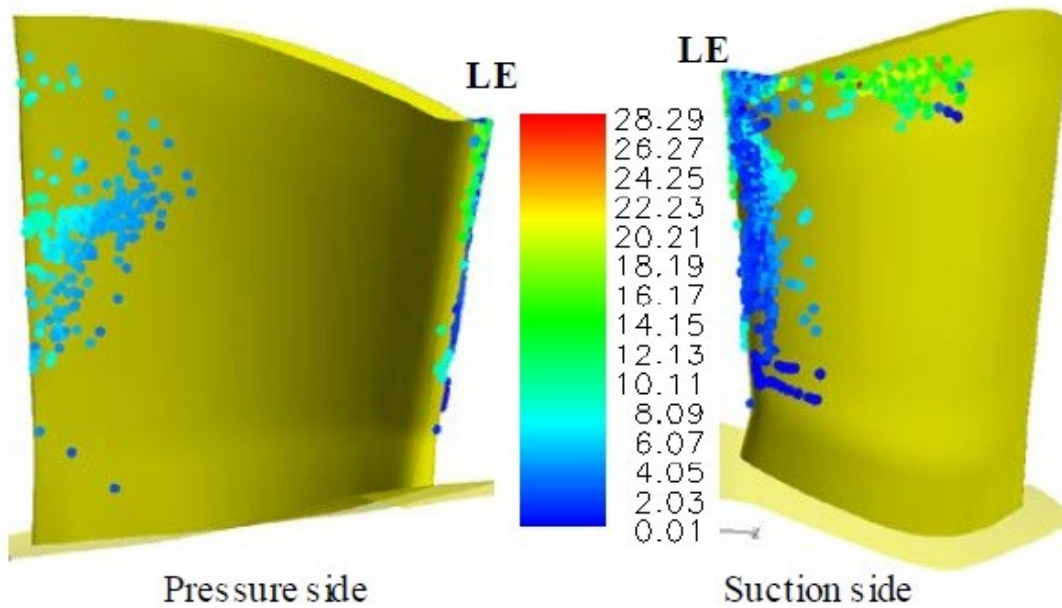
Fig. 1.8: *Sample of local erosion rates (mg/g) in 2nd NGV [Ghenaiet, 2014].*
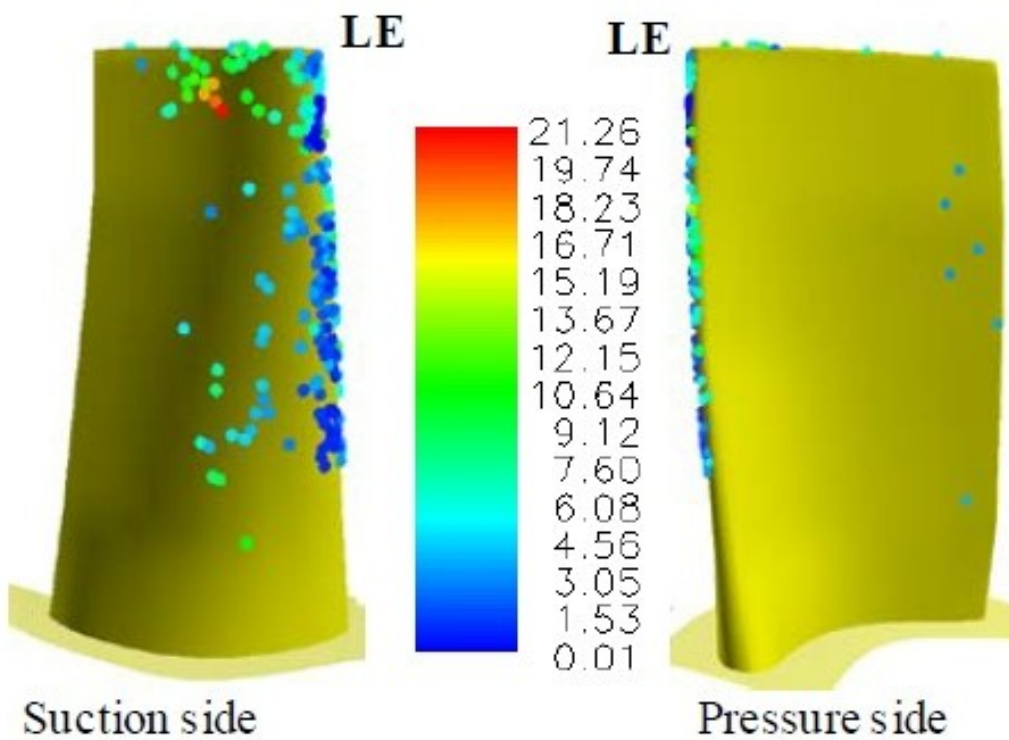
Fig. 1.9: *Sample of local erosion rates (mg/g) in 2nd rotor [Ghenaiet, 2014].*

- 24 -
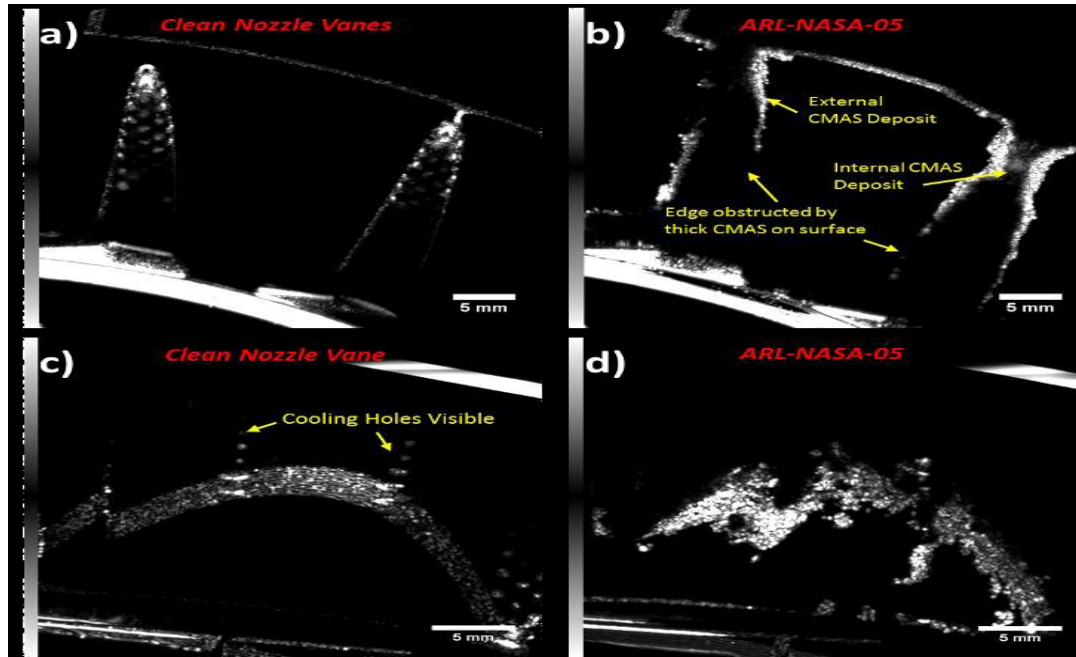
Fig. 1.10: *Scanning acoustic microscopy (SAM) of turbine vane a),b) leading edge c), d) pressure side [Murugan, et al., 2017].*

1.3 Deposition coming from environment ingested particles

Deposition from fuel purifications is similar to the deposition caused by particles as sand. Webb et al. [Webb, et al., 2013] studied the effect of ash deposits on nozzle guide vanes. Four different coal ash species, found in operating power plants (bituminous, lignite ash, etc.), were tested in an accelerated test facility. They concluded that most of the deposits were on the pressure side of the vane, including leading edge and trailing edge, as the same happens in dust polluted turbines. However, deposition formation was different on each coal ash type, therefore it can be assumed that some ash types cause thicker deposits, hence they decrease cooling effectiveness rapidly. This study also showed that surface temperature is very crucial (likewise in environment ingested particles) on the deposition formation, a conclusion that was also made in [Albert, et al., 2012], [Albert, et al., 2013] too.

1.4 Cooling hole blockage

A common effect caused by particles' ingestion, is the plugging of cooling holes and clogging of the cooling path, which may be internal, external or both internal and external. Apparently, the areas more vulnerable to clogging are pressure side, leading edge and trailing edge. Leading edge and pressure side, as mentioned above, have the highest deposits accumulation. Trailing edge is an area where cooling holes

dimension is relatively small, because it is a thin area and structural problems would emerge if they were wider. Moreover, temperature inside the hot section is over 1200 $^{\circ}$C, which makes almost all particles melt and stick to the blade surface and cooling holes. This effect reduces overall effectiveness, as well as adiabatic effectiveness dramatically. Ogiriki et al. [Ogiriki, et al., 2015] found that HPT (High Pressure Turbine) blade creep life can be reduced up to 79% from its reference creep life. Moreover, decrease of TBC thickness could halve creep life.

It has been mentioned from several sources that the cooling hole blockage strongly depends on the cooling holes geometry. Some cooling hole geometries are more susceptible to plugging than others. Also, blowing ratio (*M*) is important too. In almost every case, increase of blowing ratio prevents or diminishes plugging. Nevertheless, in real time operation, there is definitely a decrease in turbine's performance due to the increase of bleed air used for cooling.

In order to investigate cooling hole blockage, Cardwell et al. [Cardwell, et al., 2010] tested 4 coupons with both impingement (internal cooling holes) and film cooling holes, commonly called as double wall, which had different arrangement and diameter of holes. By injecting sand particles in a wind tunnel, they concluded that regardless of the arrangement and dimensions, in all 4 types pressure ratio rose, thus blockage occurred. A remarkable notice was that blockage was less in the coupon types, where impingement flow was higher, i.e. where internal flow rate was more increased. Endwall film cooling was tested by Sundaram et al. [Sundaram, et al., 2007], [Sundaram, et al., 2008], for different blowing ratios. They concluded that even a single hole blocked had a decrease in 10% in cooling effectiveness, which shows how important is clogging of cooling holes. In Fig. 1.11 we can see the experimental results for an endwall cooling, with and without upstream slot coolant flow.
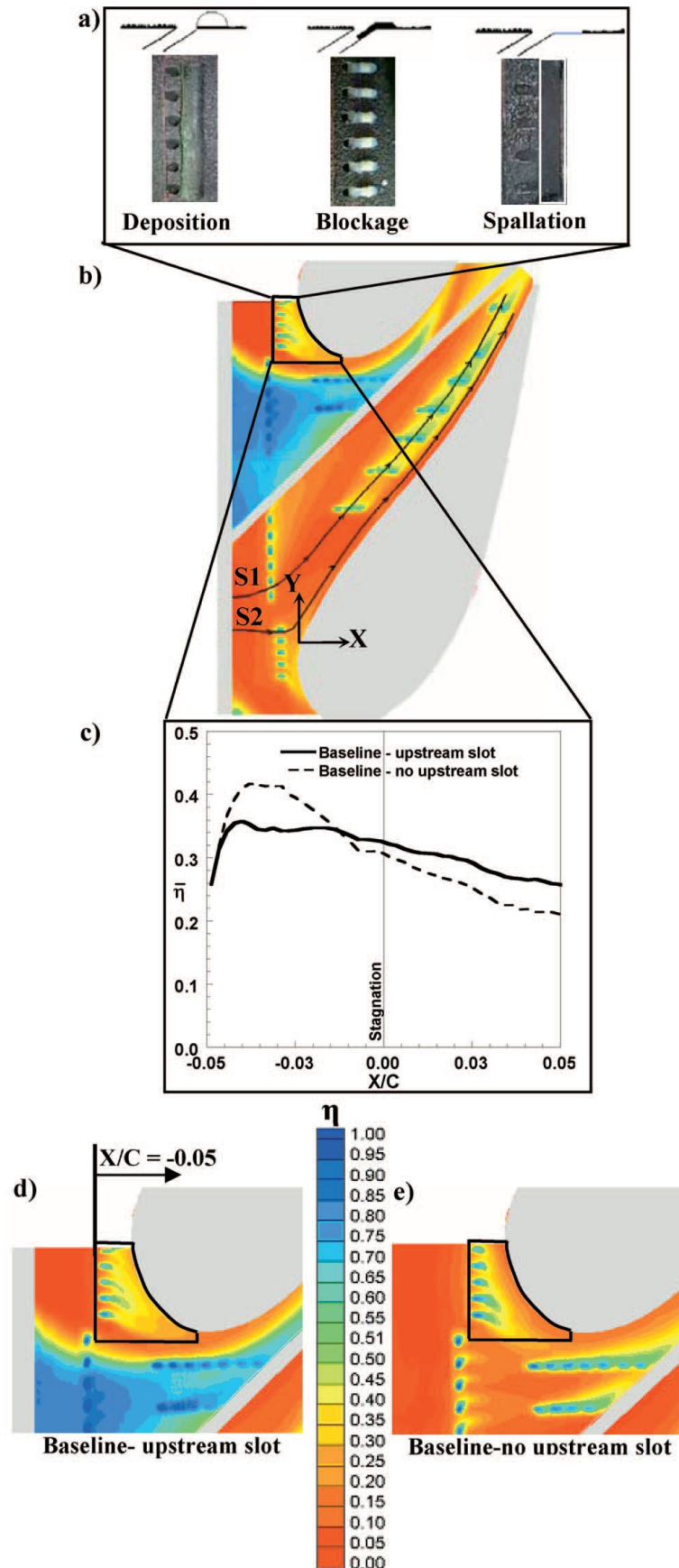
Fig. 1.11: *Vane endwall cooling with and without upstream coolant flow [Sundaram, et al., 2007].*

Lawson et al. [Lawson, et al., 2011], injected wax particles at momentum flux ratios $I = 0.23, I = 0.5, I = 0.95$, and with the use of a FLIR P20 IR camera, they acquired a temperature map (Fig. 1.12). In that way, they were able to measure adiabatic effectiveness. In general, adiabatic effectiveness was reduced with deposition. In 2012, with an almost similar procedure, deposition on showerhead [Lawson, et al., 2012c] (Fig. 1.13), on endwall film cooling with transverse trenches [Lawson, et al., 2012b] (Fig. 1.14), and on endwall film cooling [Lawson, et al., 2012a], (Fig. 1.15), were studied. As a result, trench mitigates the negative effects of blockage. This was also confirmed by the study of [Kistenmancher, et al., 2014]. A schematic of various trench configurations can be seen in Fig. 1.16.

Ai et al. [Ai, et al., 2012] studied how blowing ratio can affect particle deposition. They used bare metal and TBC coupons with different kind of cooling holes (cylindrical and shaped). The results showed that increased blowing ratio decreased deposition. Also, different types of cooling holes geometry had different deposition rates on the same blowing ratios. The most important observation however, was that the deposit growth rate is nonlinear through time (Fig. 1.17), which means that *the deposit layer on the surface increased deposition rate.*
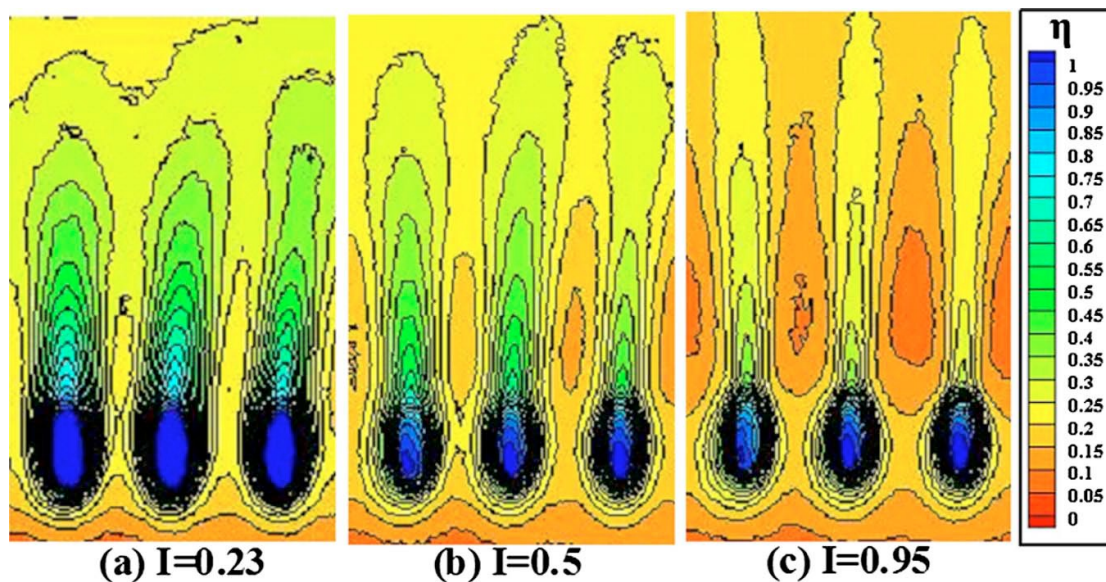
Fig. 1.12: *Adiabatic effectiveness on cooling holes in different momentum flux ratios [Lawson, et al., 2011].*
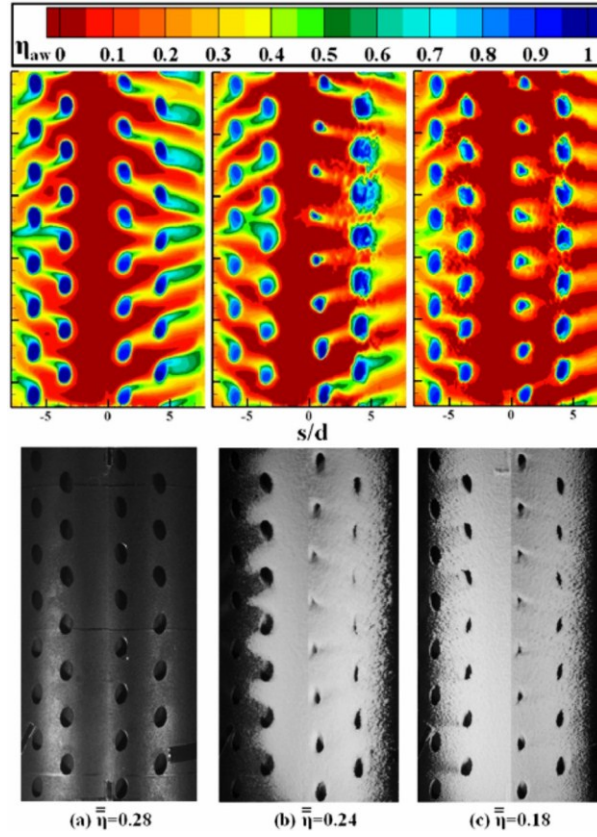
Fig. 1.13: *Temperature map of the adiabatic effectiveness on showerhead cooling holes [Lawson, et al., 2012c].*
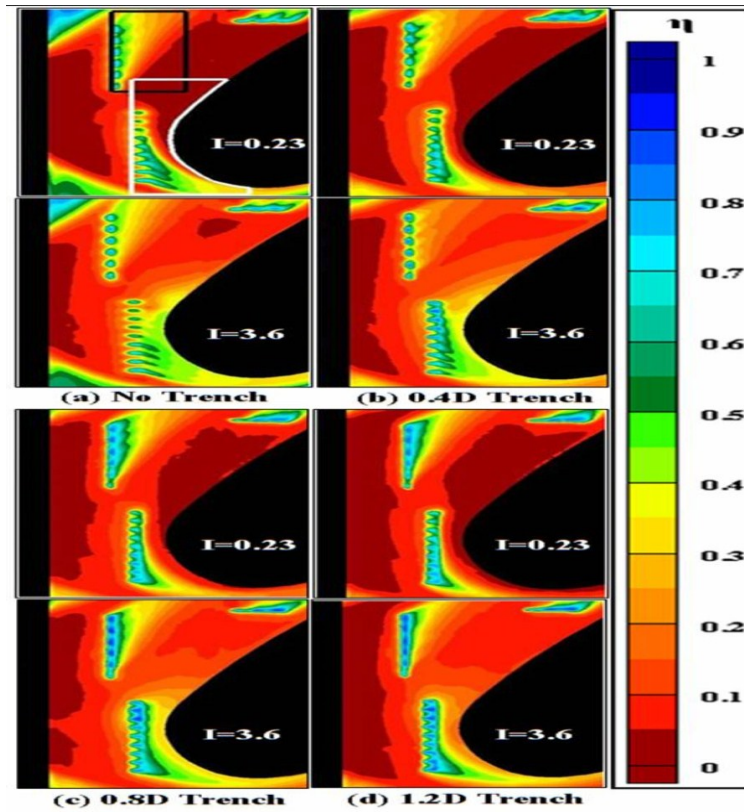
Fig. 1.14: *Adiabatic effectiveness with trench [Lawson, et al., 2012b].*
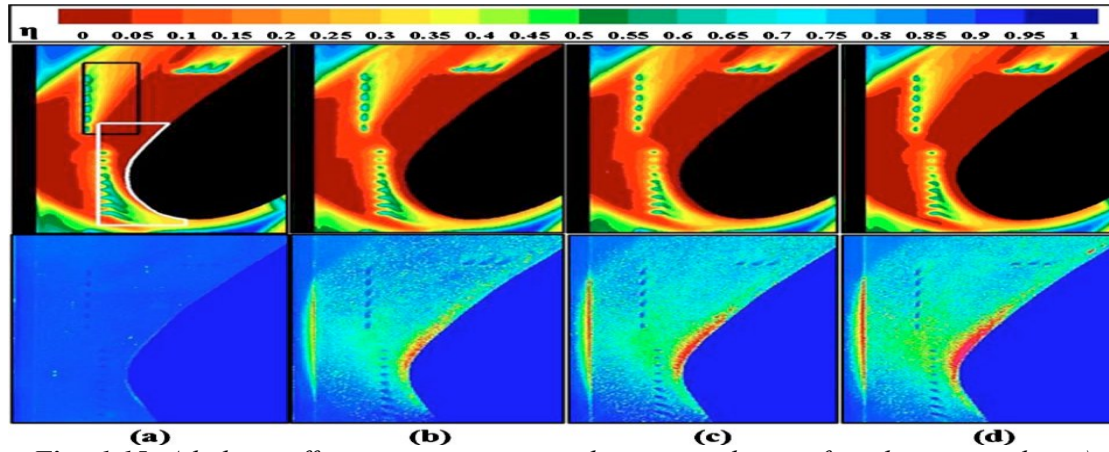
Fig. 1.15: *Adiabatic effectiveness contours and corresponding surface deposition plots a) before deposition, b) after 300 g, c) after 600 g, and d) after 900 g of wax injection at I=0.23 [Lawson, et al., 2012a].*
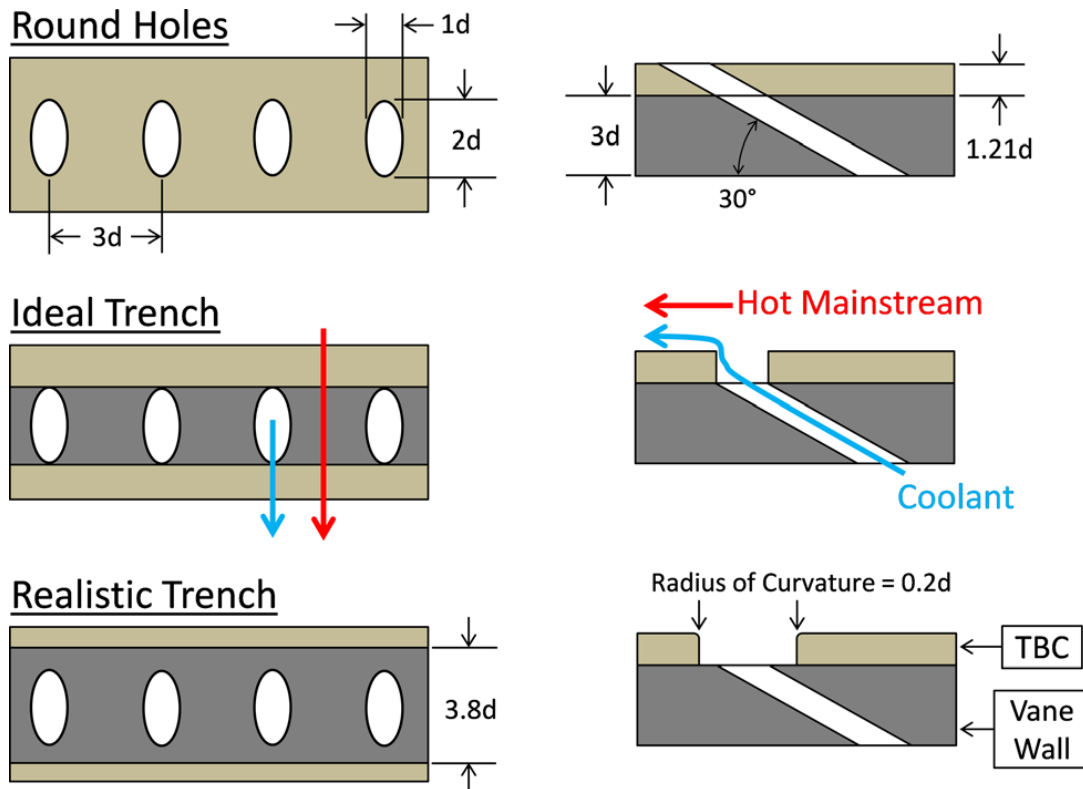
Fig. 1.16: *Schematic of trench in film cooling [Kistenmacher, et al., 2014].*
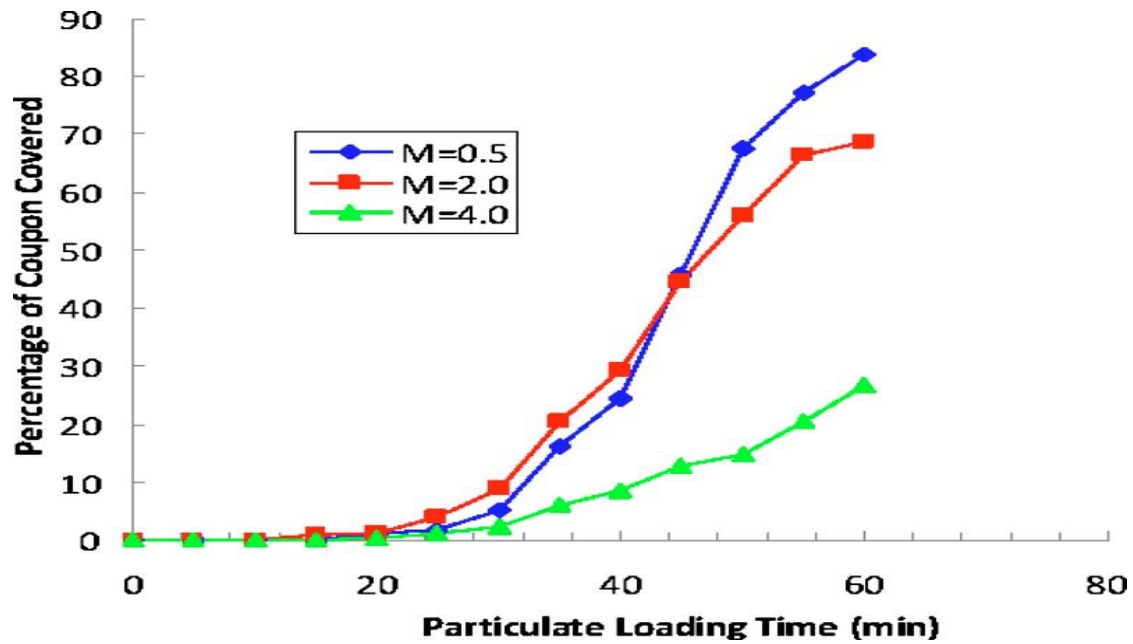
Fig. 1.17: *Percentage of deposition through time in a coupon for different blowing ratios [Ai, et al., 2012].*

Unfortunately, there are not many studies in the open literature about internal cooling passage plugging. Lau et al. [Lau, et al., 2008], by conducting naphthalene sublimation experiments, using a test section simulating internal cooling of a gas turbine airfoil near trailing edge for various Reynolds numbers (5000 to 36000), concluded that heat transfer was enhanced up to 70% with cooling hole blockage and that for higher Reynolds numbers, the heat transfer enhancement was reduced.

1.5 Turbine blade surface roughness

Surface roughness is created from the deposits of various particles in turbine blades. Due to the fact that temperatures are high in turbine inlet, deposit formation is enhanced, causing many side-effects in the efficiency. For that reason, many investigations have been conducted about HPT surface roughness. However, direct measurements are difficult to be taken in the hot section, where temperatures are above 1200 °C, hence few are the studies referred to real turbine operations. One of the first variables used to measure roughness, was [Nikuradse, 1950]

$$k^+ = \frac{k_s * u_T}{v} \tag{3}$$

where, k_s is sandgrain diameter, u_T is shear velocity, and v is kinematic viscosity. It is used for the measurement of shin friction of a rough surface [Bons, 2010], [Nikuradse, 1950] and it is one of the most used variables for measures of that kind. Additionally, many different relations have been developed to match the conditions of operating turbines and the main reason according to [Bons, 2010] is because roughness is referred with many different terms, such as sandgrain, arrays of cone elements, etc.

The most crucial effects of turbine roughness are two: increase of heat transfer (due to the fact that molten particles stick to the surface and enhance conductive heat transfer) and aerodynamic losses. The heat transfer increase results in decreasing of TBC thickness. Several times, removal of TBC is observed and, as a result, bare metal is exposed to the heat (TBC spallation). Bogard et al. [Bogard,et al., 1998], took 2 vane samples coming from engines operating in different environmental conditions. After measuring their roughness (which was apparently different), they constructed samples of them which were tested on a wind facility with Reynolds roughness number $Re_{ks} = 60$ and $Re_{ks} = 120$. Another parameter they set was momentum thickness Reynolds number $Re_\theta = 320$. The equation they used to measure roughness density parameter Λ_s was taken from [Sigal, et al., 1990]:

$$\Lambda_s = \frac{S}{S_f} * \frac{A_f}{A_s}^{-1.6} \tag{4}$$

where S is surface area without roughness, S_f is total frontal surface area, A_f is roughness element frontal area, A_s is roughness element windward wetted area. For rough surface, an increased heat transfer 50% to 60% relatively to the smooth surface was observed. In high turbulence, (turbulence intensity 10% to 17%) there was a 15% to 30% increase in heat transfer for smooth surface and a 100% increase for rough surface.

Regarding aerodynamic losses, roughness tends to make the flow turbulent across the surface and many times boundary layer separation has been observed, which leads to decreased turbine efficiency and sometimes even stall. Casari et al. [Casari, et al., 2017] presented a model implemented in a 3D Navier-Stokes solver and they confirmed that flow path changes when in roughened blades. Somawardhana et al.

[Samawardhana, et al., 2009] conducted an experiment where they tested how roughness affects cooling holes, for smooth and rough surface. Initially, it was noticed that in cylindrical holes, effectiveness degrades in low blowing ratios (M<1.0). On the contrary, in high blowing ratios (M>1.0), adiabatic effectiveness increases. Afterwards, obstructions were placed on the upstream area of the cooling holes, downstream of cooling holes, and then on both directions. The highest degradation (up to 50%) was due to the upstream obstruction of cooling holes (Fig. 1.18). In the downstream obstruction scenario, adiabatic effectiveness was increased to all the blowing ratios tested (Fig. 1.19).
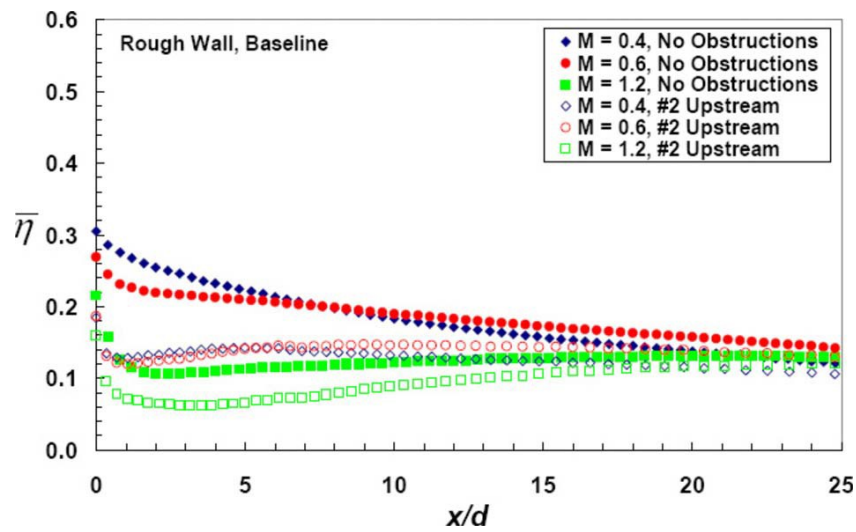
Fig. 1.18: *Adiabatic effectiveness with a rough wall and upstream obstructions [Samawardhana, et al., 2009].*
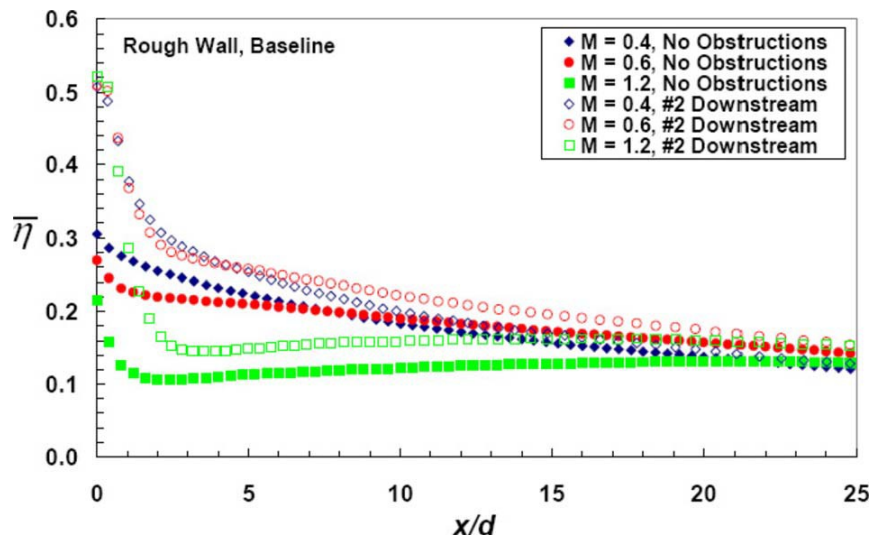
Fig. 1.19: *Adiabatic effectiveness with a rough wall and downstream obstructions [Samawardhana, et al., 2009].*

Moreover, in [Stripf, et al., 2005] it was noticed that roughness surface moves the laminar-turbulent transition upstream, therefore turbulent heat transfer increases. Also, roughness doesn't seem to affect the pressure side in laminar turbulence. Yun, et al. [Yun, et al., 2005] performed tests in a single stage turbine. They calculated a dimensionless roughness parameter $k^+= 30$ for transitional roughness and a $k^+=149.2$ for full turbulence roughness. As it can be seen in Fig. 1.20, there is a loss of 2% on the pressure side of turbine stator and 6% on the suction side, when roughness exists. When either rotor or stator blades are roughened, there is a loss of 4% and 8% on the pressure and suction sides, respectively. Finally, when both stator and rotor are roughened, the loss is 8% and 19% on the surfaces previously mentioned (Fig. 1.21, Fig. 1.22, Fig. 1.23). As a conclusion, roughness of stator affects turbine performance way more than rotor. From Yun's research, it can also be noticed that the area affected most is suction side, something that is commonly accepted and repeatedly proven in many researches. Rutledge et al. [Rutledge, et al., 2006], who also investigated suction side, came to the same conclusion. The use of trench improves and mitigates the roughness effects too, as was done in cooling hole blockage (Fig. 1.24).
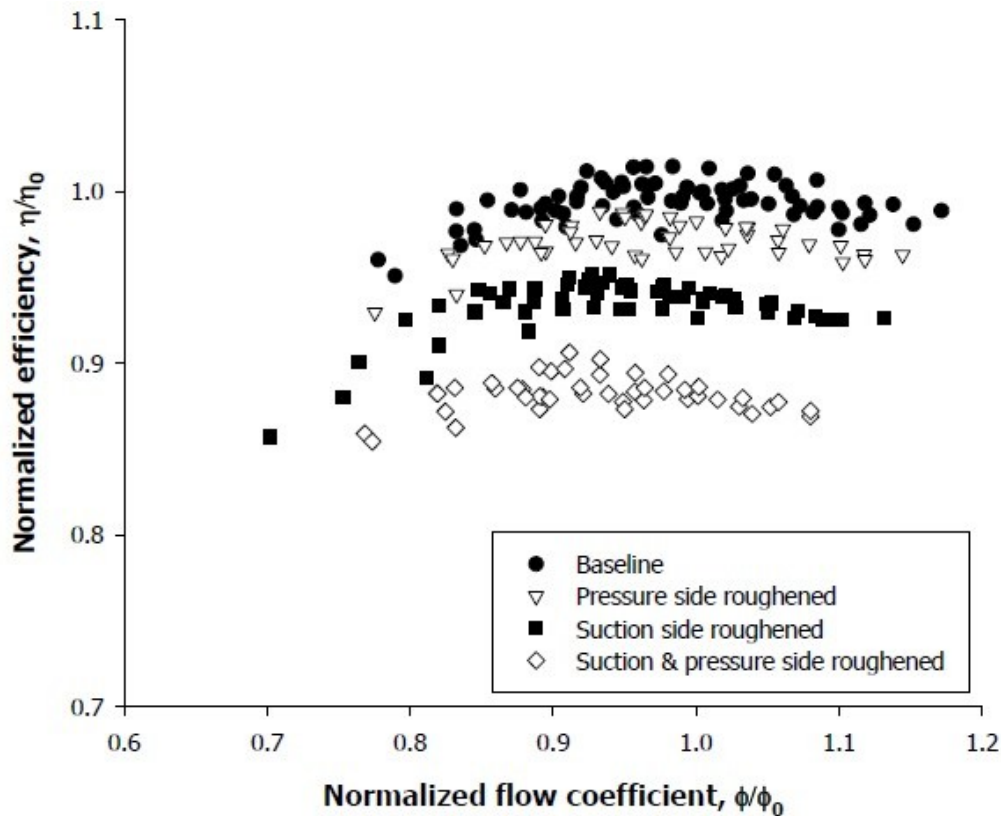
Fig. 1.20: *Fully roughened stator (k_s=400μm or k^+=149.2) [Yun, et al., 2005].*

Fig. 1.21: *Transitional roughness stator and rotor (k_s=106μm or k^+=30) [Yun, et al., 2005].*

Fig. 1.22: *Transitional roughness stator and rotor (k_s=106μm or k^+=30) [Yun, et al., 2005].*

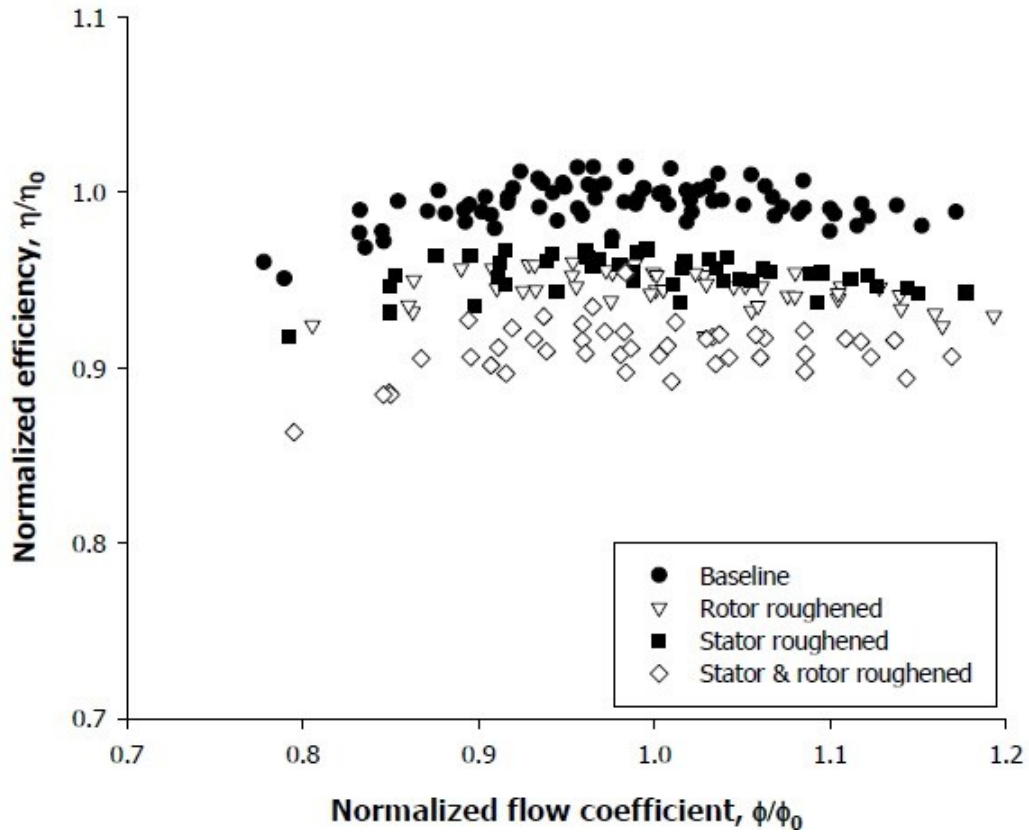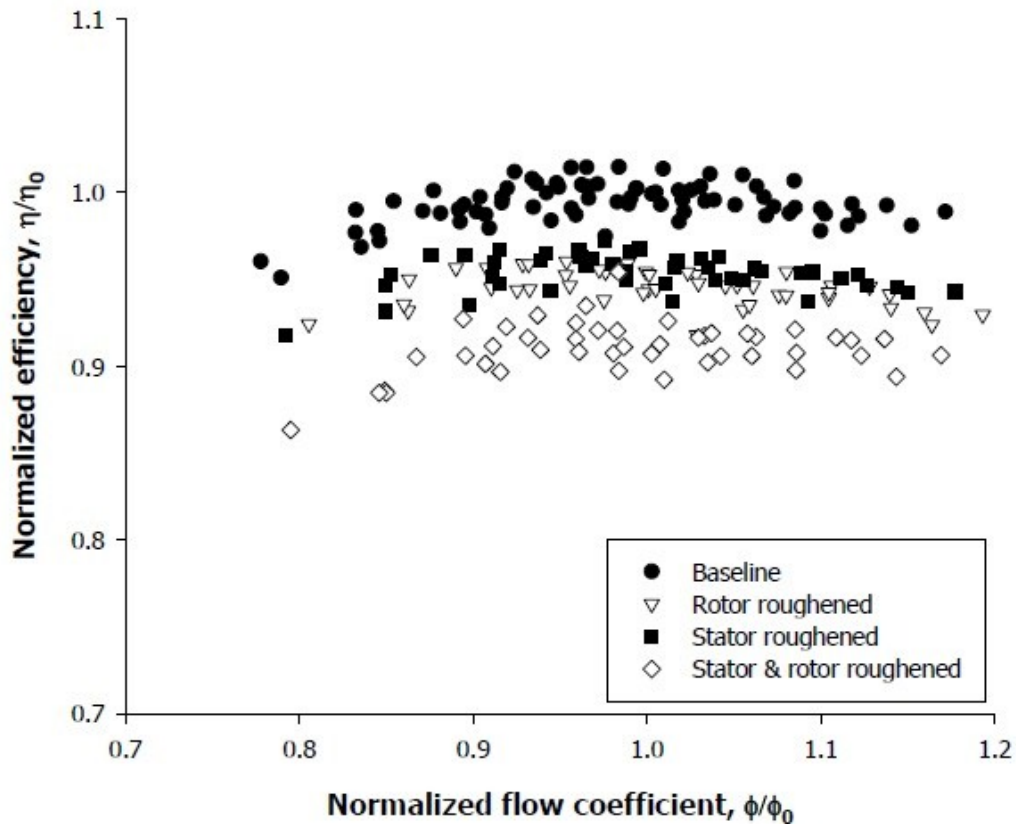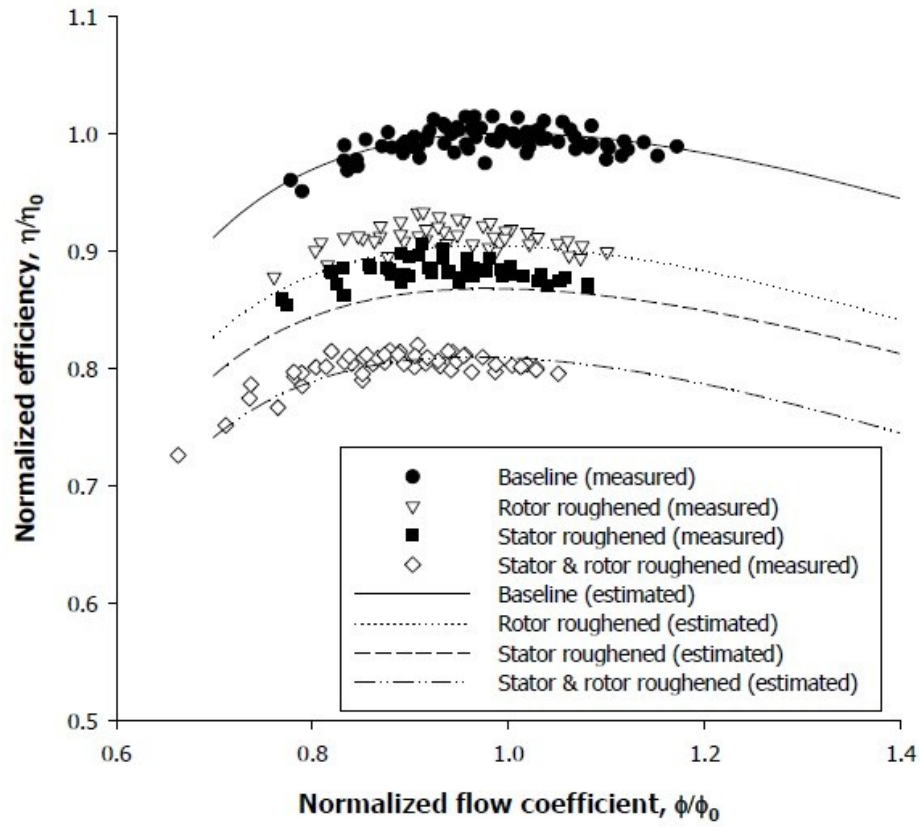**Fig. 1.23:** *Full roughness stator-rotor (k_s=400μm or k^+=149.2) [Yun, et al., 2005].*
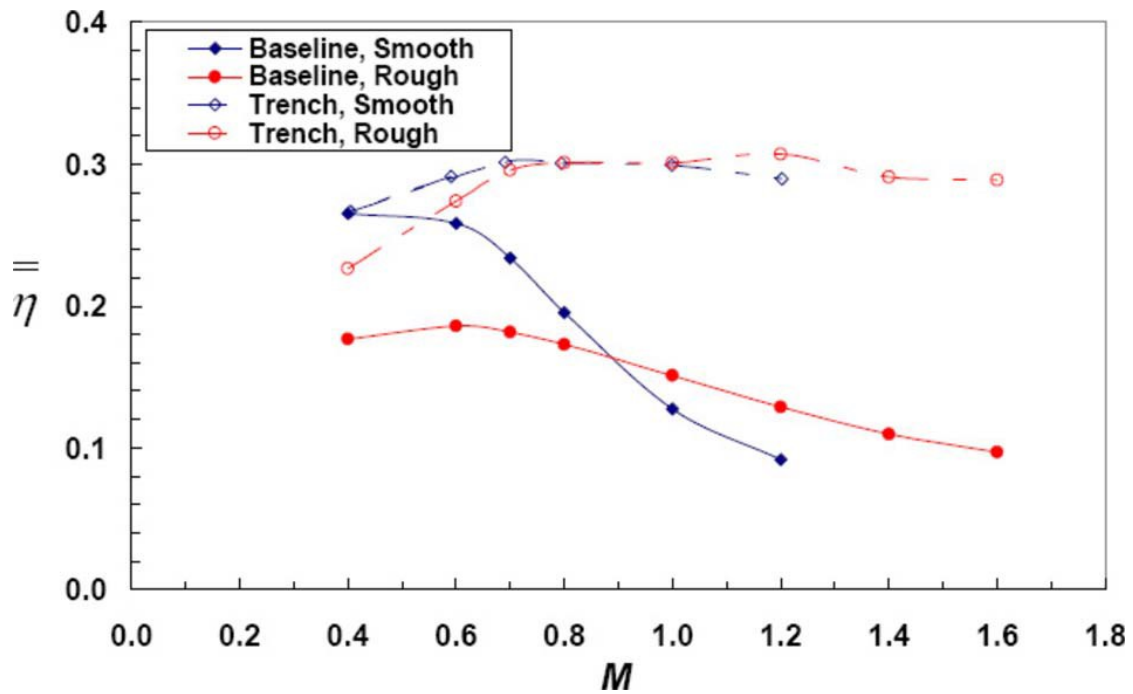

Fig. 1.24: *Adiabatic effectiveness tests with and without trench [Samawardhana, et al., 2009].*

1.6 Gas turbine washing

Washing has been proven to be a fruitful method of fouling removal in the engine's compressor and turbine. Efficiency that was lost due to deposition is gained back, according [Roupa, et al., 2013]. Not only efficiency increases, but also degradation caused by ingested particles ceases to spread.

Demineralized water and solvents are the most common fluids used for engine washing. Water is used for water soluble particles, such as dirt or salt and solvents, and can be used either hot or cold. When hot, the removal of deposits is apparently easier, but the drawback is that a lot of energy is required in order the water to be heated [Stadler, et al., 2001]. Also, the preparation time for engine wash is also increased, which means that the cost might increase radically if the engine produced energy and has shutoff in order to be washed. Regarding the solvent use, it is for mostly oil deposits or impurities coming from non-water soluble materials. It is of big importance that the chemical solvent use is not very aggressive, because corrosion might be created in the blades.

According to [Madsen, et al., 2014], the water-to-air ratio injected to the engine is very important for the cleaning and safe operation of the engine. It was proven that higher water-to-air ratio was more effective in cleaning and restoring of lost efficiency. Specifically, tests were conducted in a LM2500 engine. Low water to air ratio was 0.45% and 18 liters/min water flow rate, whereas high water rate was 0.75% with 30 liters/min water rate. Also, temperature and pressure were measured during operation, because extreme temperature drop might result in flameout and extreme pressure might even cause erosion or corrosion or damage to the rotors due to stress. As mentioned above, the high water rate proved to be more efficient. Last, another parameter that results in efficient engine wash is droplet size, where it should clean the whole blade adequately, not partially. That of course differs from engine to engine, so there hasn't been recorded an "optimum" dimension for droplet size.

There are two kinds of engine washing: on-line washing and off-line or crank washing. On-line washing is performed when engine operates and shutoff isn't needed. It is applied mainly in power-plants and industrial engines. The cleaner mostly used is sprayed water. On-line washing is efficient when it is used very often, even every day if needed. It is a cheap solution, because engine doesn't need to shutoff, which in power plants for example would cost a lot. On-line water tests

[Syverud, et al., 2007] showed that efficiency degradation rate is decreased. Off –line washing is more efficient, but engine shutdown is required. That makes it automatically a more expensive solution than on-line washing. It is usually conducted when efficiency levels are the lowest allowable, so that engine can return almost to 100% of his initial performance. However, according to [Basendwah, et al., 2006], it was noticed that efficiency was dropped about 1% - 2% after each washing interval, probably due to the engine's aging of the components. Off-line washing can be used to every engine, even aircraft engines.

In order the washing to be efficient, there needs to be designed a certain schedule. Haub et al. [Haub, et al., 1990] tried to combine offline washing and online washing procedures. The results are show in Fig. 1.25.

Omar Hill Unit "A" Performance Loss Cycle
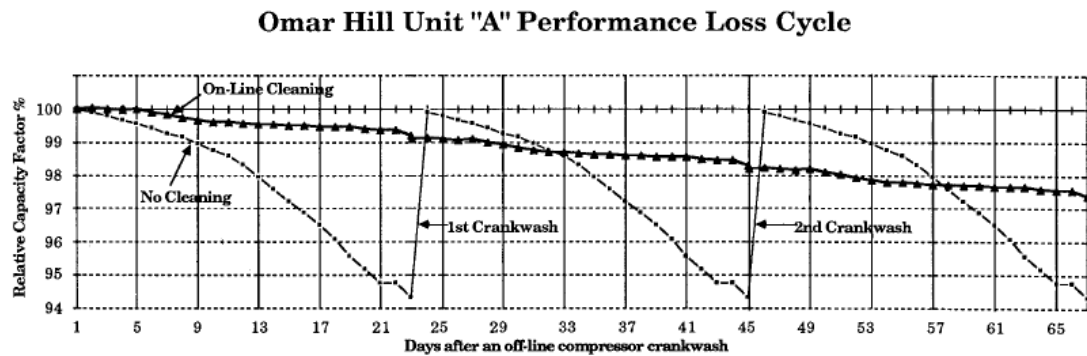
Fig. 1.25: *On-line and off-line washing results [Haub, et al., 1990].*

Madsen et al. [Madsen, et al., 2014] also tried many washing scenarios and also found that the best solution was daily off-line washing and interval crankwash every 4 months with high water rate (30 l/min). The results were that there was a drop in 2% in efficiency until next interval crank wash, while there was a 3% drop in low rate washing (Fig. 1.26, Fig. 1.27).

From all above, it can be concluded that a cost-benefit approach is needed in order the exact interval times to be decided. This approach will not be analyzed, as it is beyond the scope of this work.
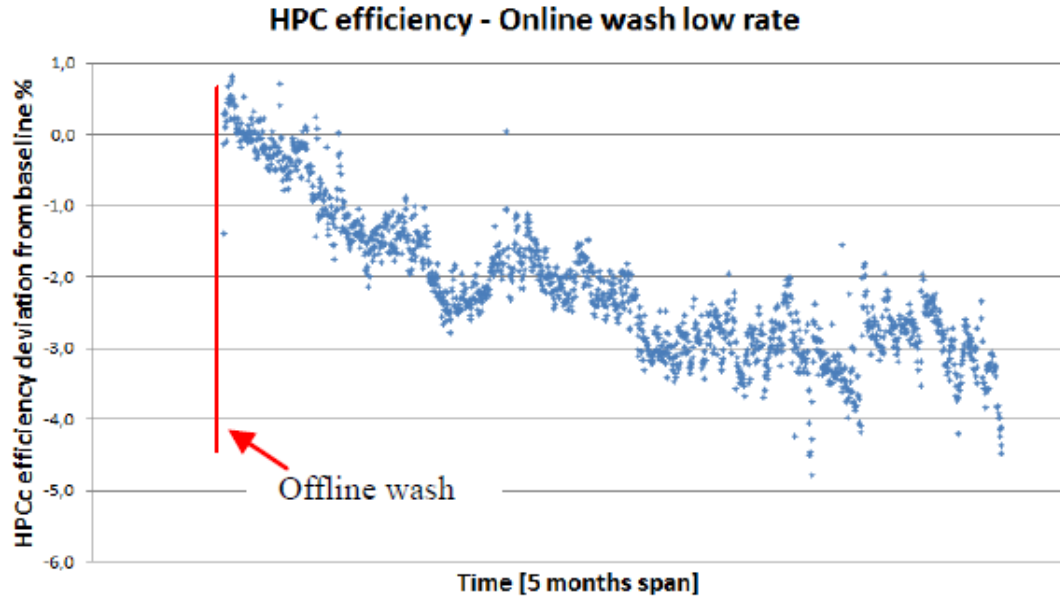
Fig. 1.26: *HPC efficiency - online wash low rate [Madsen, et al., 2014].*
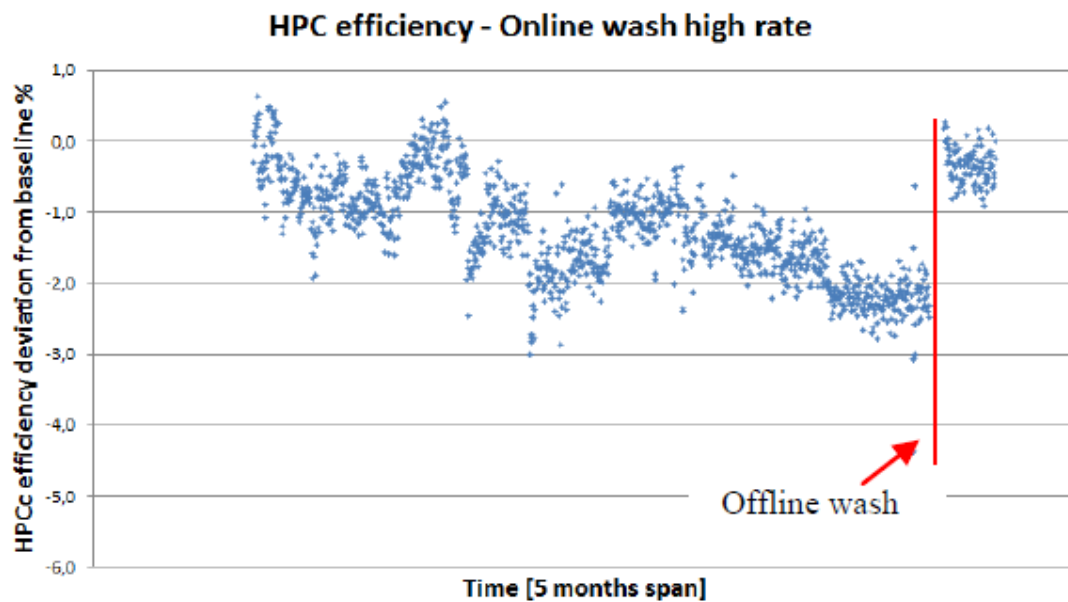
Fig. 1.27: *HPC efficiency - online wash high rate [Madsen, et al., 2014].*

1.7 Air filtration

Air filtration is a very effective way of reducing fouling occurring by air contaminants such as dust, salt, humidity, etc. A filtration system is placed upstream engine inlet, so the air ingested is not "polluted" (Fig. 1.28). Many publications refer to engine filtration systems. Though, in this work only the basic principles of air filtration will be described.

Fig. 1.28: *Schematic of an air filtration system [Wilcox, et al., 2010].*

The most common filtration systems are two-stage and three-stage systems. The first stage is usually for preventing various environmental factors, such as rain, ice, fog, etc., from entering the following stages. In that way, filtration gets more efficient. The following stages most commonly contain high-efficiency filtration elements, which prevent even the smallest particles from entering the engine inlet.

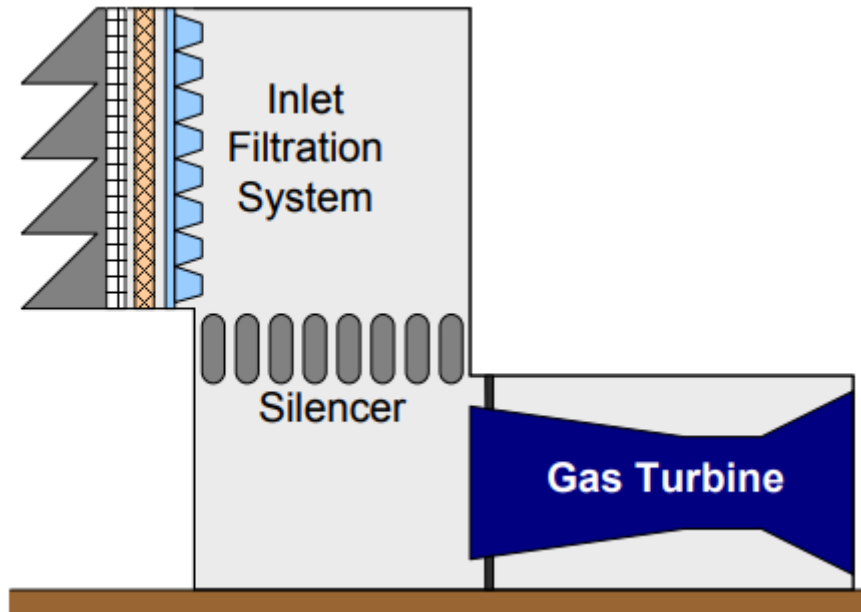As referred above, operational environments vary from region to region. As a result, different filtration elements and technologies are required in order the gas turbine's operation to be efficient. In table 1.2, we can see the characteristics of various environmental conditions. Goulding et al. [Goulding, et al., 1990] concluded that depending on the conditions, customizations in the filtration systems are needed (anti-ice system, salt removal, insect strainers, etc.), in order to be more effective.

The main drawback of filtration is that the gas turbine inlet air pressure drops significantly. This results in power output decrease. Moreover, with adding more filtration stages, pressure drops even more (Fig. 1.29). Therefore, the goal is to achieve the highest filtration efficiency with the lowest pressure drop. In order this to be accomplished, system shall be remained cleaned constantly, so as pressure drops to be minimized. The most common cleaning system is air injection that comes from engines' bleed system.

Table 1.2: *Environmental conditions in various geographic areas [Goulding, et al., 1990].*

GEOGRAPHIC AREA, ENVIRONMENT AND FAULT CHART

Geographic Area	Environmental Conditions	Particle Concentration Mg/m^3	Particle Size range in microns	Fault
URBAN (Major metropolitan areas with heavy industry)	Rain, fog, smog, some snow. 28° F. to 100° F. (-1° C. to +40° C.) Corrosive chemicals, hydrocarbons, dry corrosive, gummy soot particles, dried salt.	50-175	0.01 - 30	Fouling Erosion Corrosion
RURAL/ARCTIC (Forest, tundra, agriculture)	Snow, freezing rain, hoarfrost. -40° F. to 90° F. (-40° C to +31° C.) Dry, non-corrosive, fibrous particles and blowing dust.	<135	0.01 - 10	Fouling
OFF-SHORE & MARITIME	Wet and dry salt, corrosive particles. 0° F. to 90° F. (-18° C. to +31° C.) Blowing rain, sea spray, fog, snow, ice.	<135	0.01 - 5	Fouling Corrosion
DESERT	Dry, sunny. 30° F. to 120° F. (0° C. to +50° C.) Sand storms, whirlwinds, dry corrosive particles, salt.	>350	0.01 - 100	Fouling Erosion Corrosion
TROPICAL	Heavy rainfall. 40° F. to 120° F. (+5° C. to +50° C.) Fibrous, non-corrosive particles, insects.	<135	0.01 - 10	Fouling

Air filtration prevents the engine deterioration and has been proven to be a good option for harsh operational environments for power gas turbines. However, we should keep in mind that there can't be 100% of air filtration, at least with the current filtration technologies, so internal engine wash might be needed occasionally for the power output to be maximized.
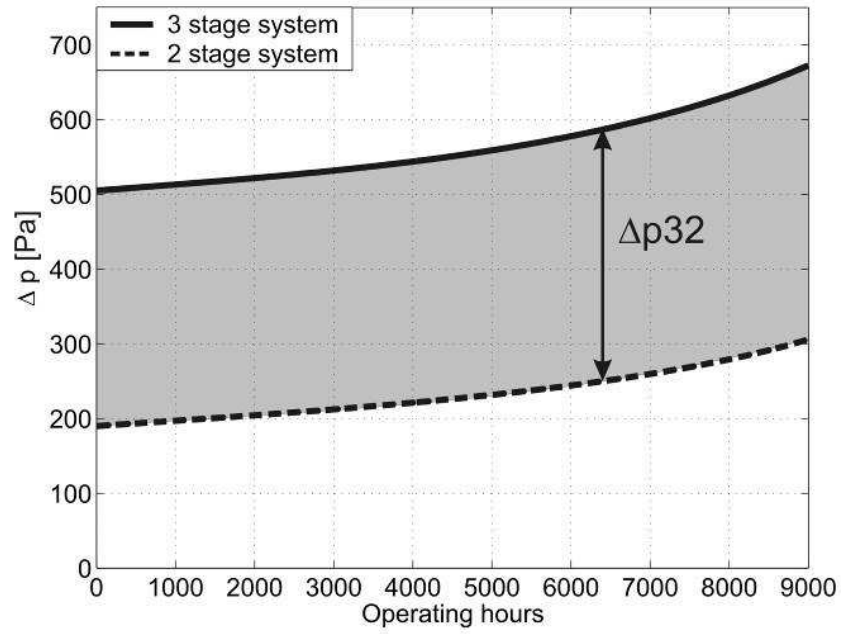
Fig. 1.29: *Difference in pressure drop between 3 stage and 2 stage systems [Schroth, et al., 2008].*

Chapter 2: Cooling Hole Design

2.1 Introduction to CAD

Computer-aided design (CAD) is the use of computers to aid in the creation, modification, analysis, or optimization of a design [Narayan, et al., 2008]. CAD software is used to increase the productivity of the designer, improve the quality of design, improve communications through documentation, and to create a database for manufacturing [Narayan, et al., 2008], CAD output is often in the form of electronic files for print, machining, or other manufacturing operations. The term CADD (for Computer Aided Design and Drafting) is also used [Duggal, et al., 2000].

Its use in designing electronic systems is known as electronic design automation (EDA). In mechanical design, it is known as mechanical design automation (MDA) or computer-aided drafting (CAD), which includes the process of creating a technical drawing with the use of computer software [Madsen, et al., 2012].

CAD software for mechanical design uses either vector-based graphics to depict the objects of traditional drafting, or may also produce raster graphics, showing the overall appearance of designed objects. However, it involves more than just shapes. As in the manual drafting of technical and engineering drawings, the output of CAD must convey information, such as materials, processes, dimensions, and tolerances, according to application-specific conventions. CAD may be used to design curves and figures in two-dimensional (2D) space; or curves, surfaces, and solids in three-dimensional (3D) space [Farin, et al., 2002].

CAD is an important industrial art, extensively used in many applications, including automotive, shipbuilding, and aerospace industries, industrial and architectural design, prosthetics, and many more. CAD is also widely used to produce computer animation for special effects in movies, advertising and technical manuals, often called DCC (Digital Content Creation). The modern ubiquity and power of computers means that even perfume bottles and shampoo dispensers are designed using techniques unheard of by engineers of the 1960s. Because of its enormous economic importance, CAD has been a major driving force for research in computational geometry, computer graphics (both hardware and software), and discrete differential geometry [Pottmann, et al., 2007].

2.2 Design procedures

The cooling hole was designed, according to Fig. 2.1 [Saumweber, et al., 2008], using the CAD software CATIA V5R19 and the model was designed parametrically (based on the diameter D of the cooling hole), so that it can be modified easily.
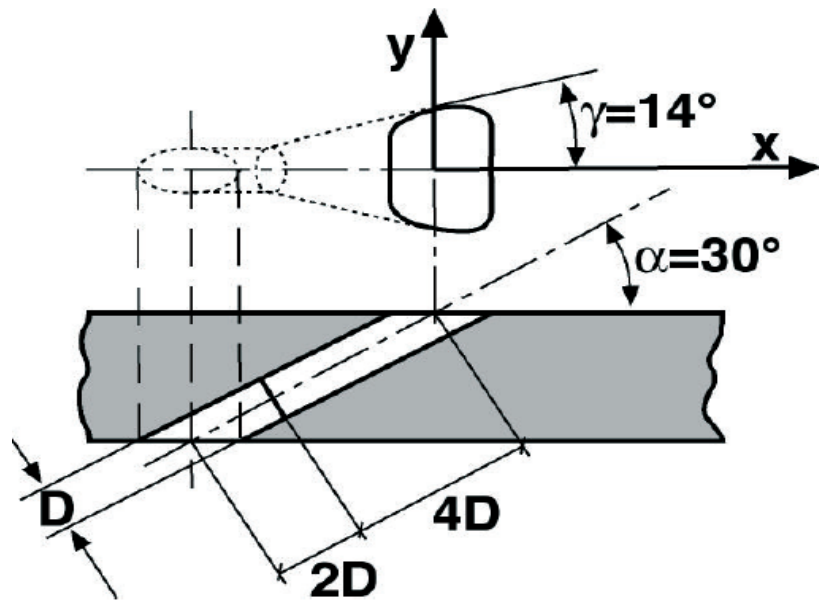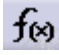

Fig. 2.1: *Cooling hole schematic [Saumweber, et al., 2008].*

   Initially, a diameter D of 1.2 mm was defined, a value close to the diameter of the actual gas turbine cooling holes (Fig. 2.2). Then, plane 1 was created with the **plane** command, defining as the **plane type** the *offset from plane* command and as **reference**, the *xy plane* with **offset** *0 mm* (Fig. 2.3). At next, point 1 was set with **point** command at (*0, 0, 0) coordinates* (Fig. 2.4), while afterwards the spine was created in the following way:

- With the **sketch** command and the *zx plane* as a **reference**, a line was created with *point 1* so as to form an angle of *30 degrees* with the horizontal axis.
- Two points were definedon the spine with distances *4D* and *2D* respectively (Fig. 2.5), using the **formula** $f_{(x)}$ command.

- Constraints were created for all points and dimensions, using the **constraints** command, so that they are completely defined (Fig 2.6).
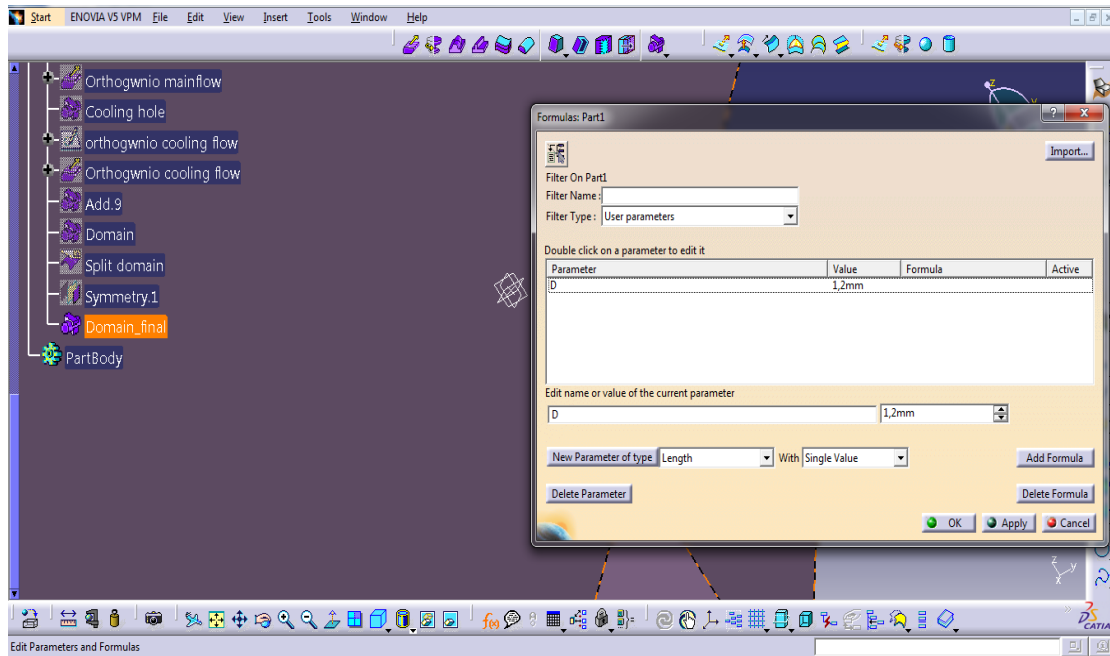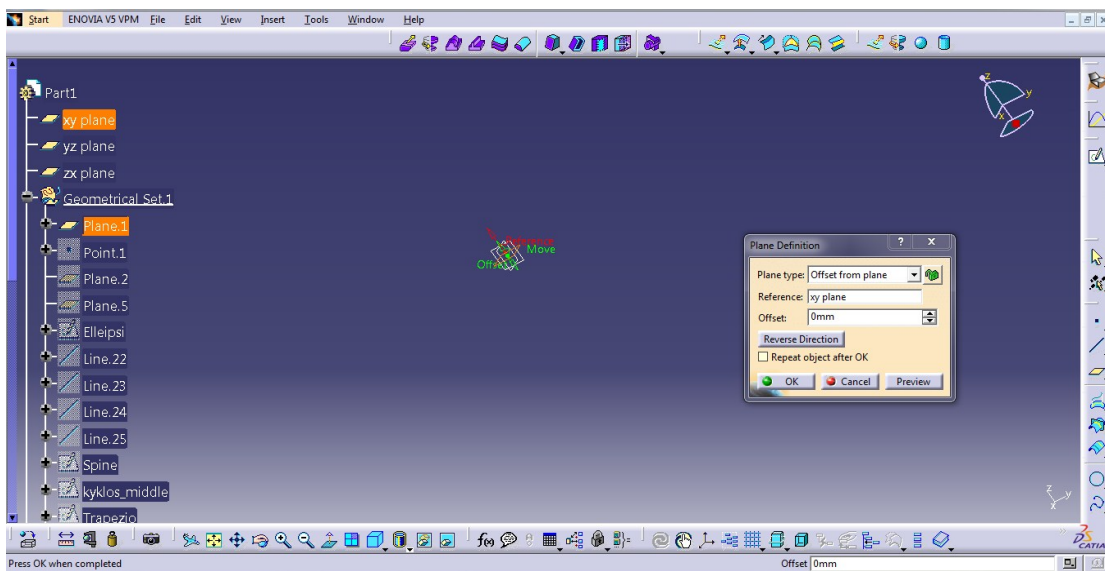

Fig. 2.2: *Definition of diameter D.*

Fig. 2.3: *Plane 1 definition.*
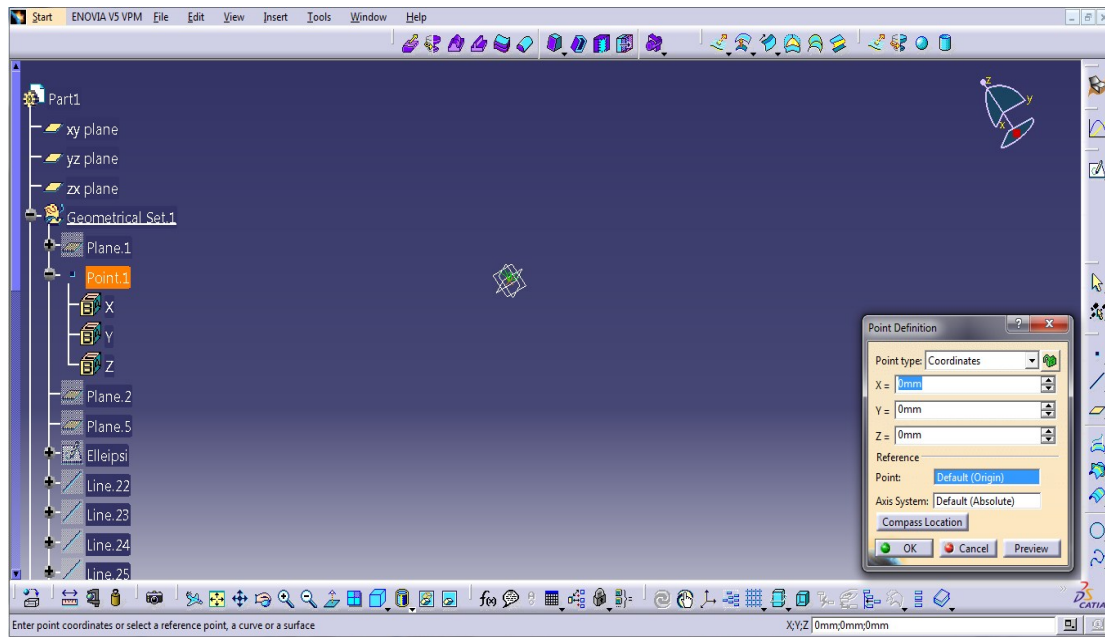
Fig. 2.4: *Point 1 definition.*
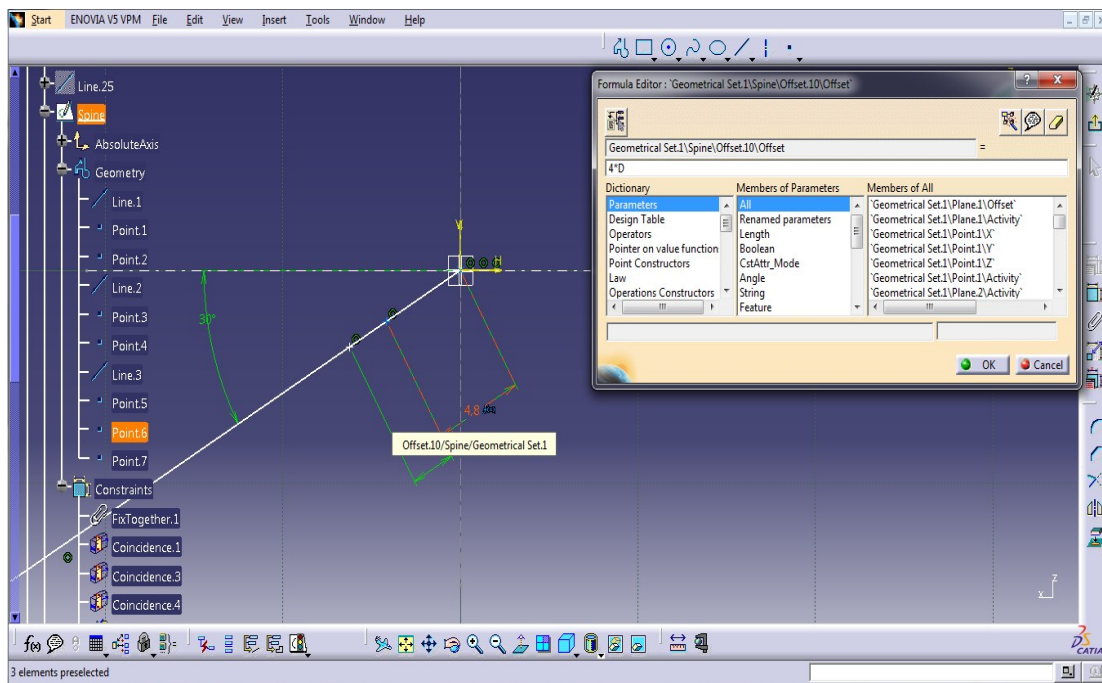
Fig. 2.5: *Spine dimension 4D set.*
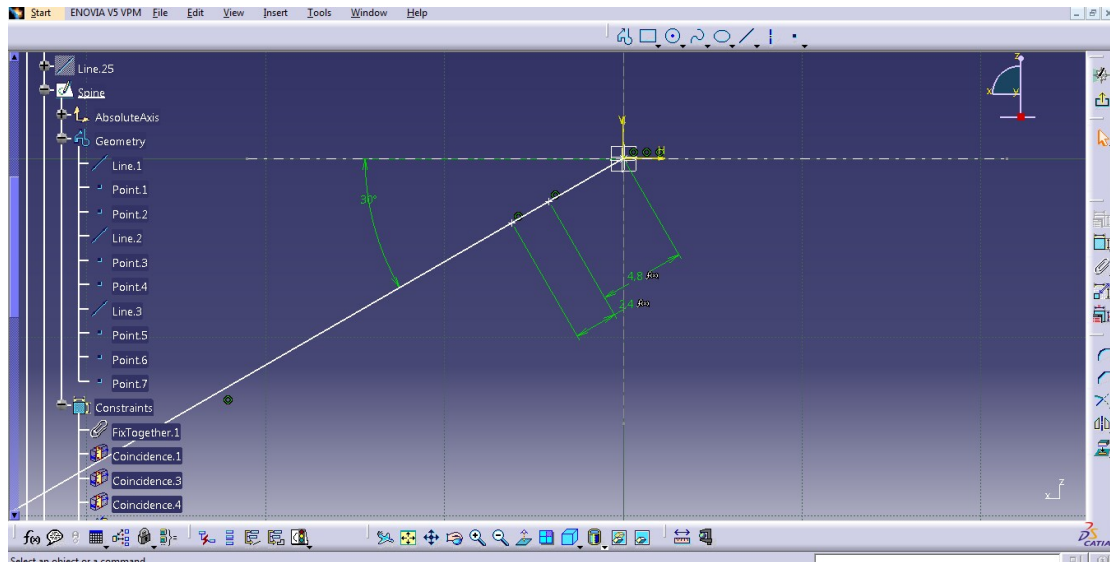
Fig. 2.6: *Spine schematic.*

Thereafter, plane 2 and plane 3 were created as follows:

- Plane 2 was created by selecting **normal to curve** option, *selecting spine* as the **curve** selection and *point 2* as **point** selection (Fig 2.7).

- Plane 3 was created with a **parallel through point**, selecting as a **reference plane 1** and as **point**, *point 3* (Fig. 2.8, Fig. 2.9).
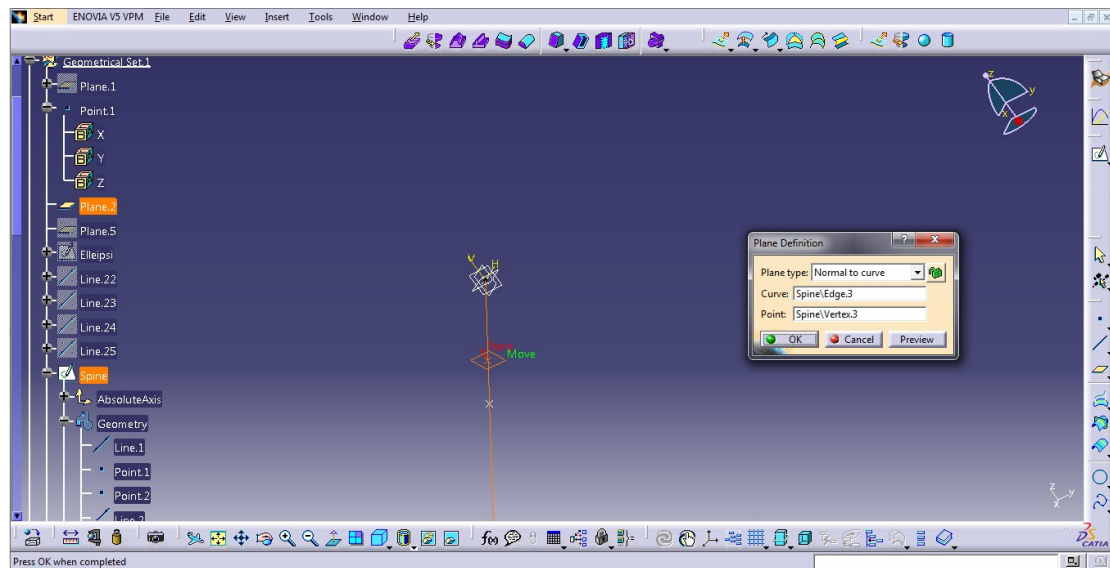
Fig. 2.7: *Plane 2 definition.*

Fig. 2.8: *Plane 3 definition.*

Fig. 2.9: *Spine with planes.*

In plane 3 an *ellipse* (Fig 2.10) was defined, in plane 2 a *circle* (Fig 2.11) and in plane 1 a *trapezoid* (Fig. 2.12). Specifically for the trapezoid, the **join** command was used after the design to join its sides.
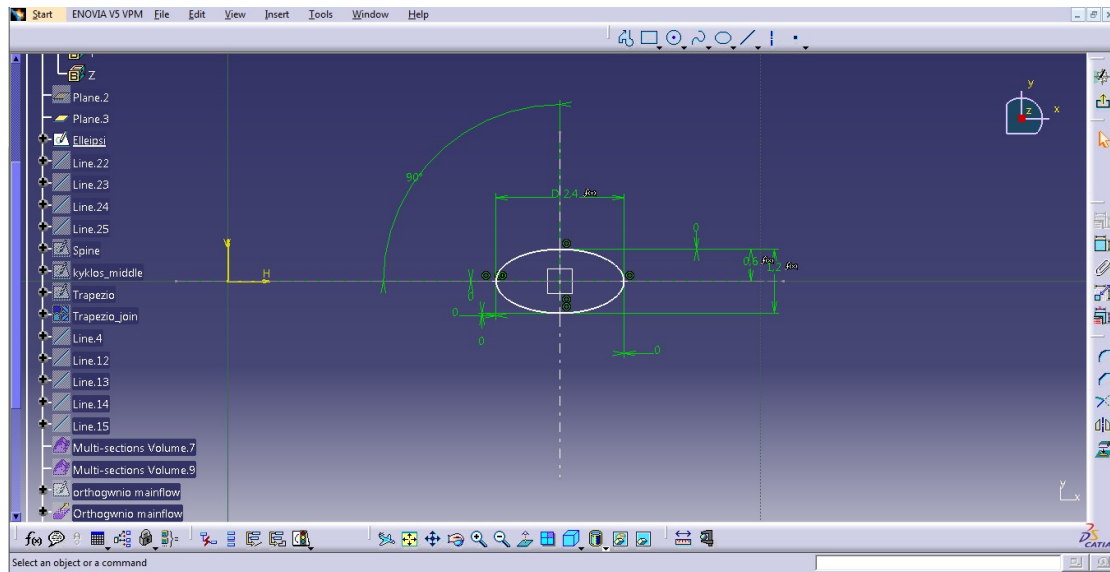
Fig. 2.10: *Ellipse schematic.*
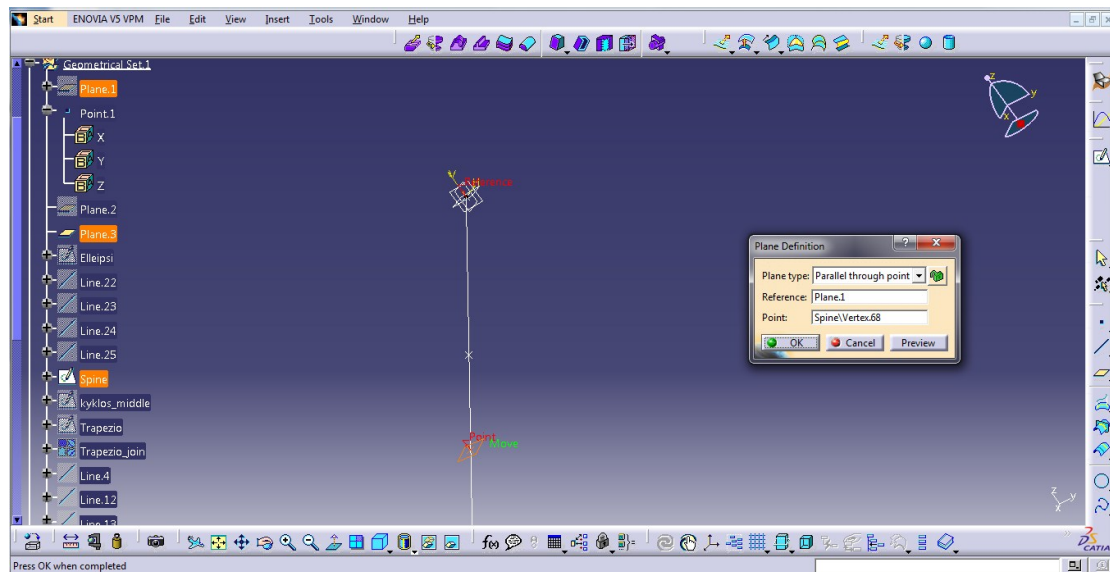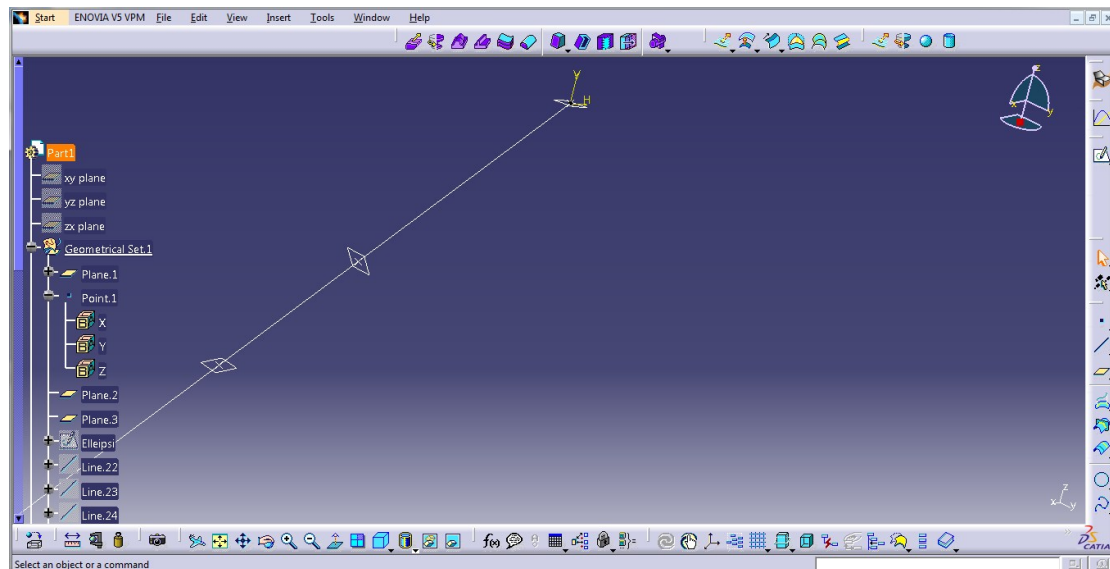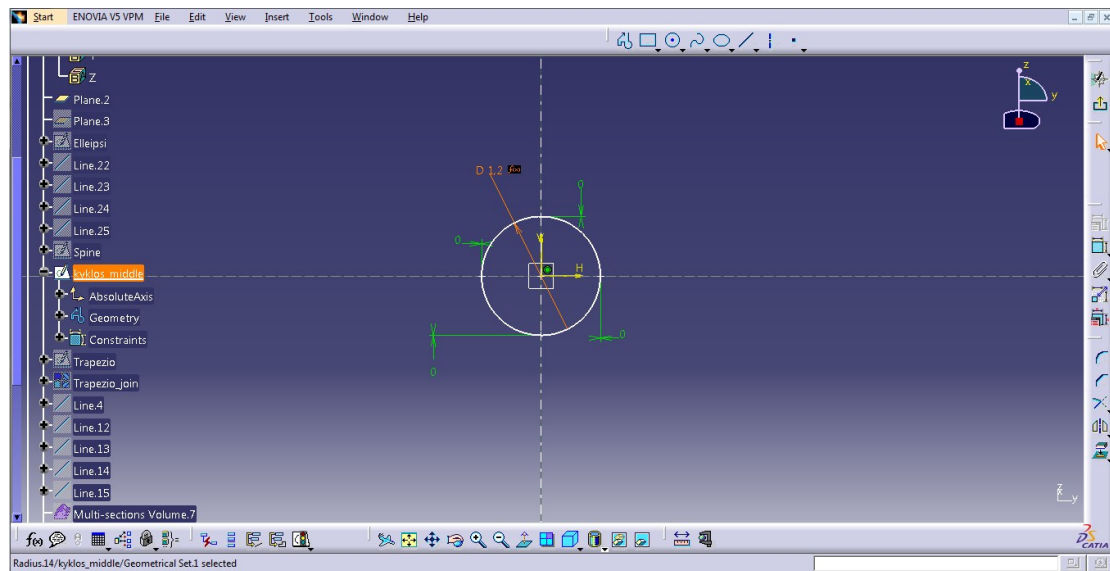

Fig. 2.11: *Circle schematic.*
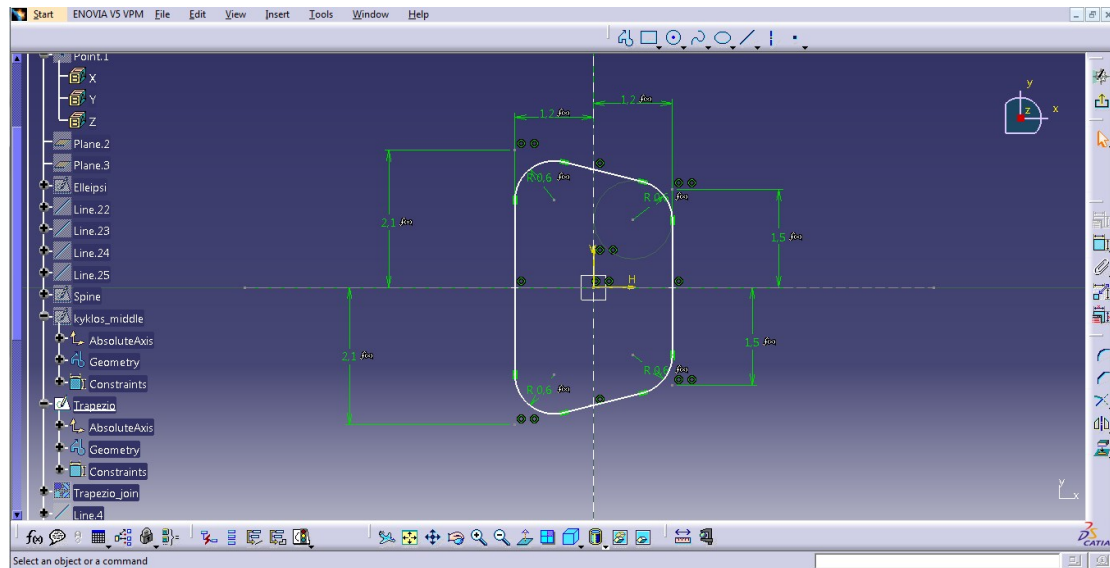
Fig. 2.12: *Trapezoid schematic.*

Finally, to create the cooling hole, *four points* were defined in each of the intersections (Fig. 2.13, Fig. 2.14, Fig. 2.15), which were joined with the **line** command, so as to be used as *guides* (Fig. 2.16, Fig. 2.17). The final cooling hole was created with the **multisections volume** command as follows:

- Initially, the *circle of plane 2* and the *trapezoid* were selected by using the guides defined above (Fig. 2.18).

- The *ellipse of plane 3* and the *circle of plane 2* were selected.

- The two created volumes were joined with **Add** command, thus creating the 3D model of the cooling hole (Fig. 2.19).
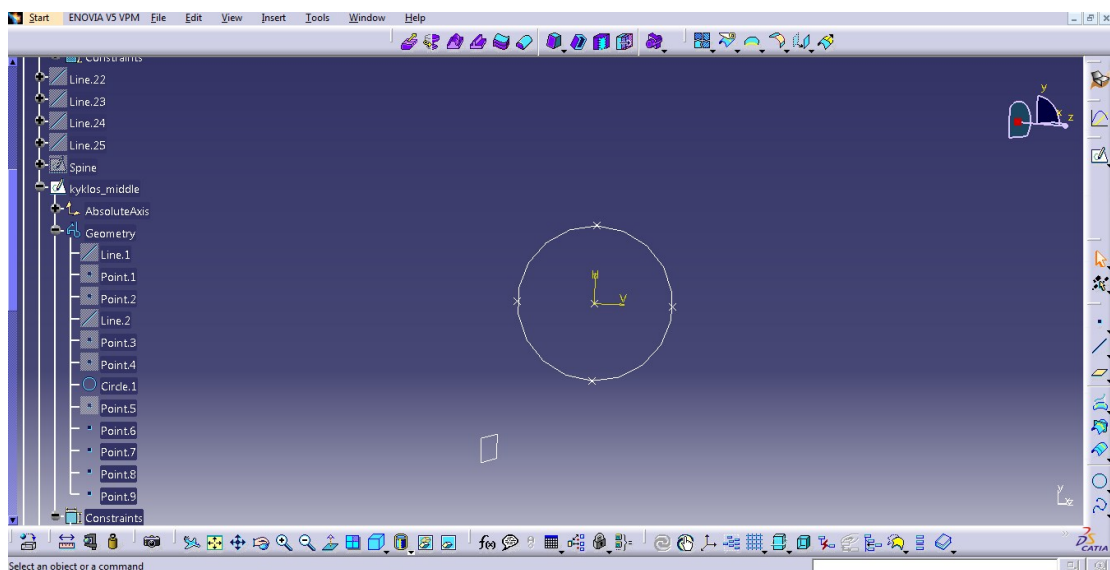
Fig. 2.13: *Four points on circular intersection.*
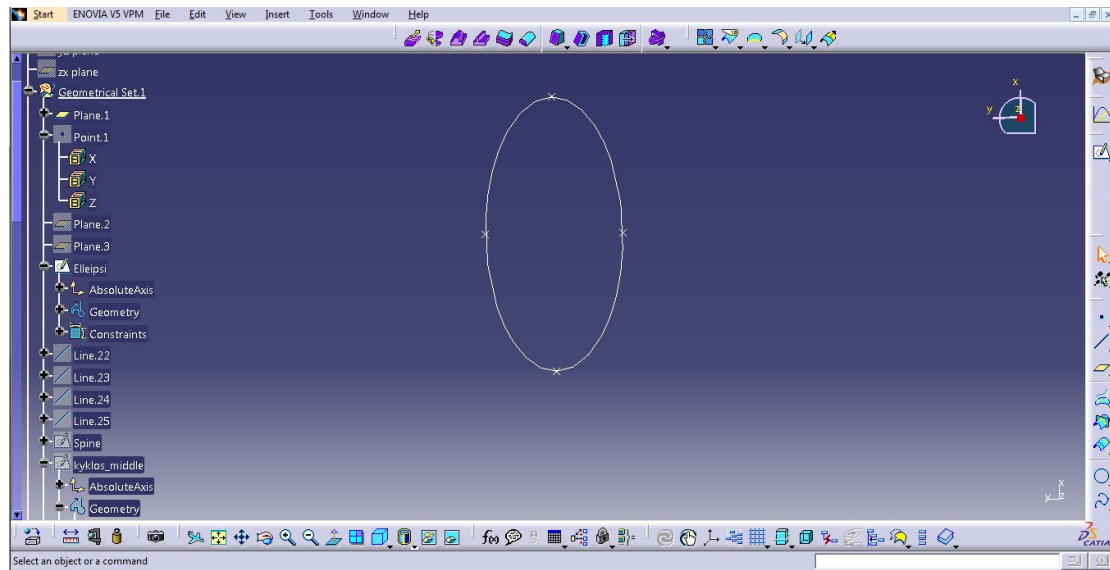
Fig. 2.14: *Four points on elliptical intersection.*
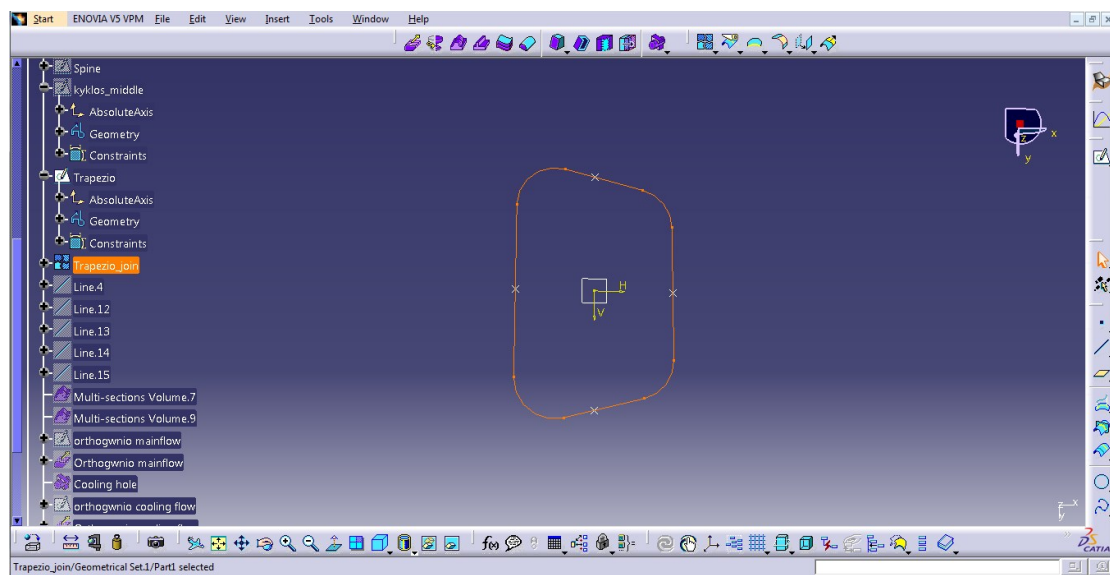
Fig. 2.15: *Four points on trapezoidal intersection.*
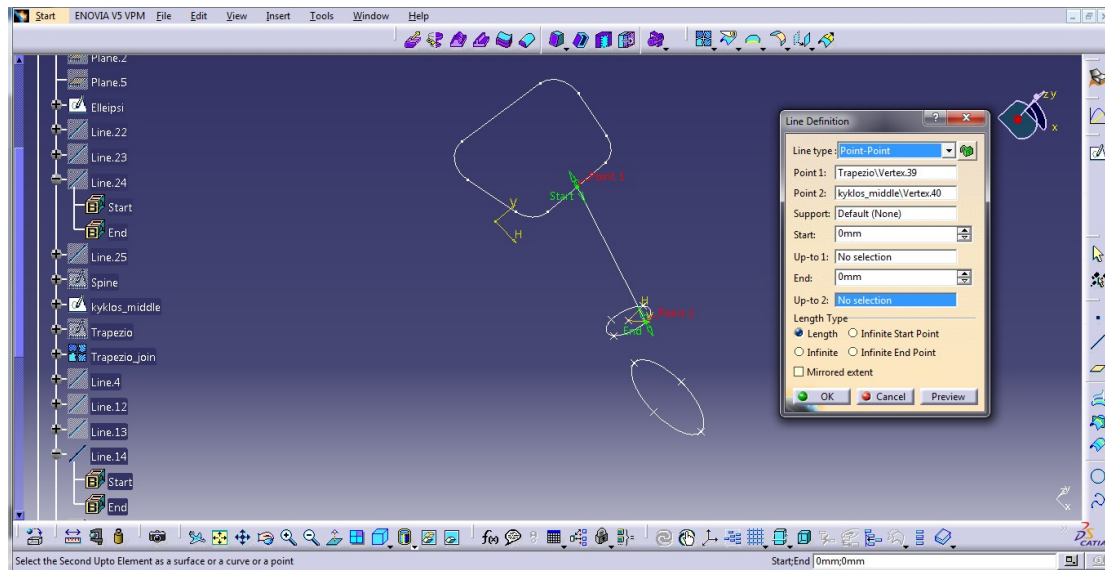
Fig. 2.16: *Line definition.*
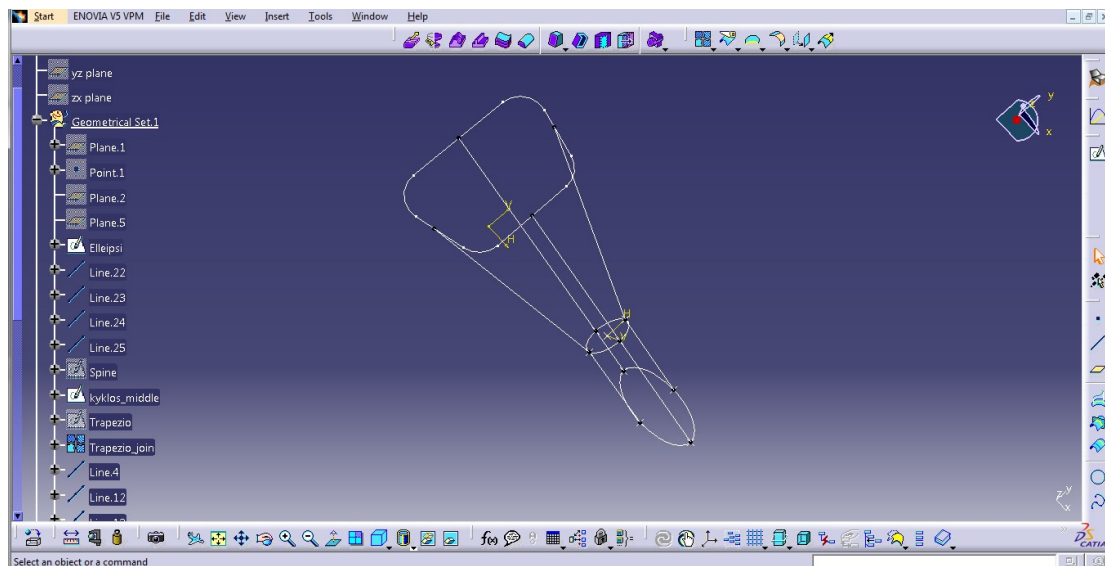
Fig. 2.17: *Guide lines.*
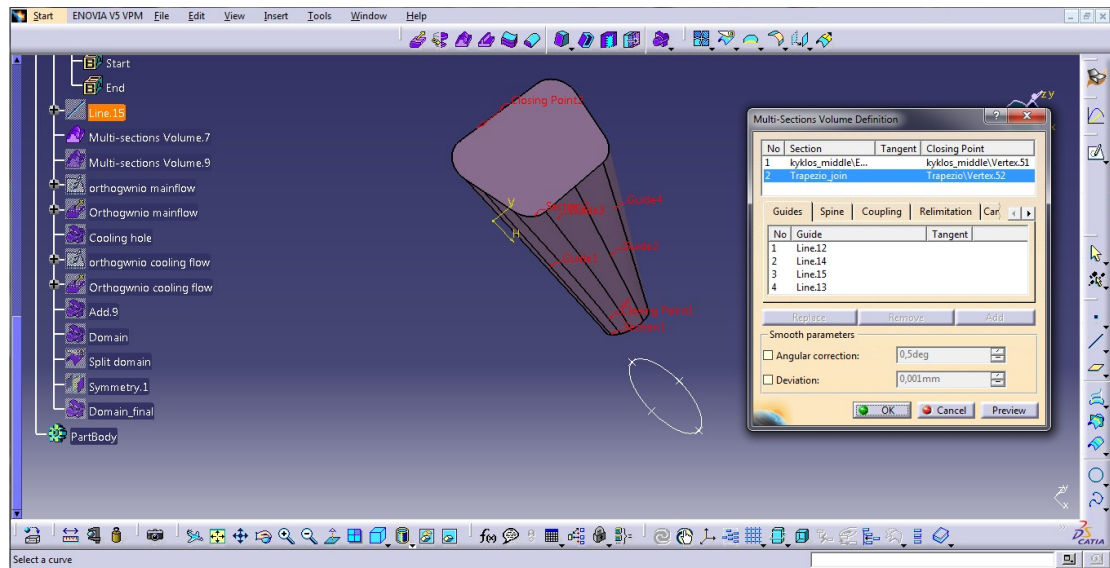
Fig. 2.18: *Multisection volume definition of circle and trapezoid.*
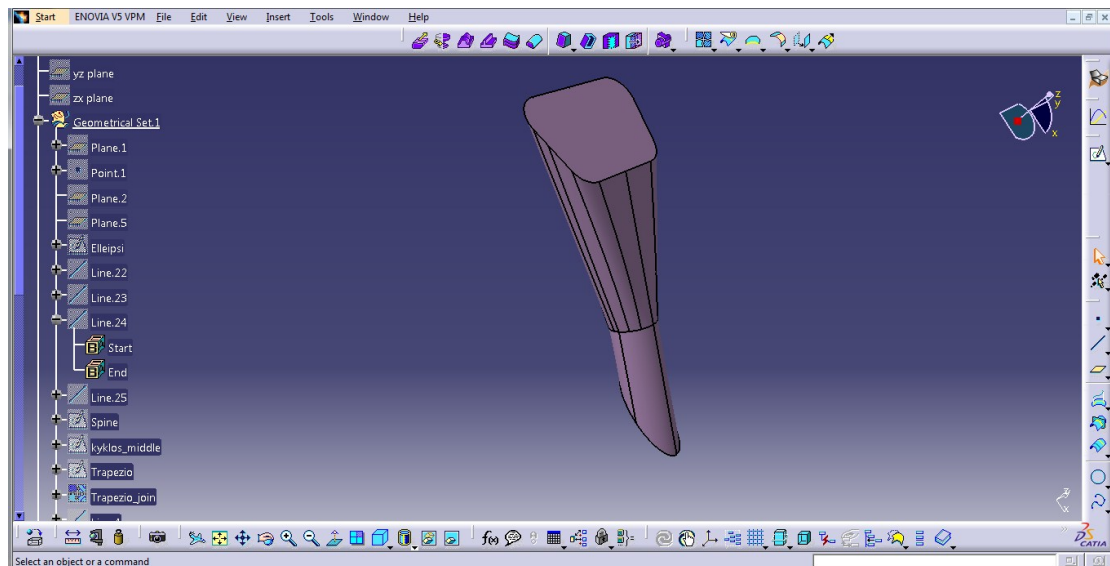
Fig. 2.19: *Cooling hole graphic.*

2.3 Final Domain Design

In order to create the final domain, two rectangular domains were created, one at the entrance and one at the outlet of the cooling hole (i.e. the intersections of the ellipse and the trapezoid respectively) in the following way:

- A rectangle with dimensions 50D upstream of the cooling hole, 110D downstream, 34D width and 35D height was created on plane 1, using the **volume extrude** command (Fig 2.20).

- Correspondingly, a rectangle with dimensions of 35D length, 30D width and 15D height was defined on plane 3 (Fig. 2.21).

- Both domains were joined with the cooling hole using the **add** command, forming the final domain (Fig. 2.22).
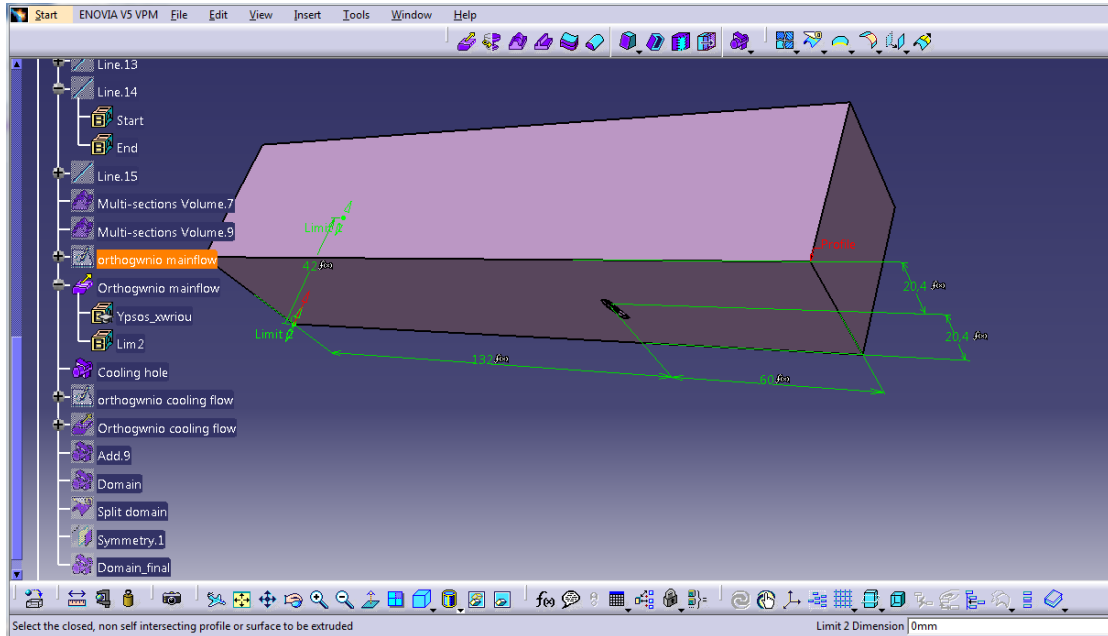
Fig. 2.20: *Mainflow domain.*
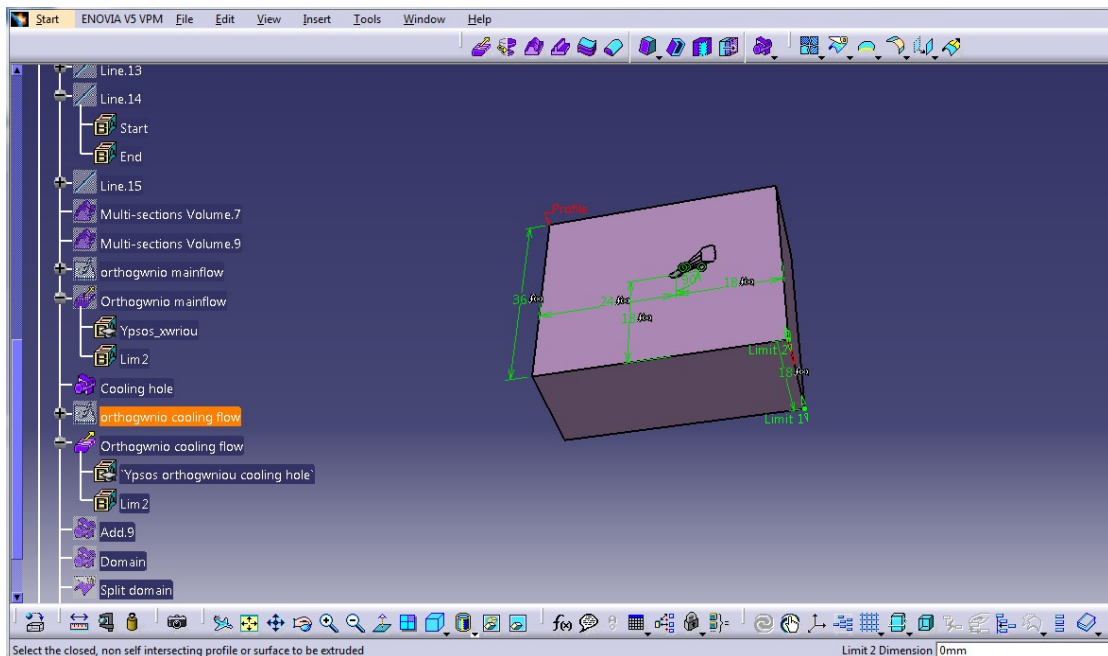
Fig. 2.21: *Cooling flow domain.*

Chapter 3: CFD Simulation

3.1 Introduction to Computational Fluid Dynamics (CFD)

For many years, computers have been used to solve fluid flow problems, with great success. Various commercial and academic programs have been developed to solve various fluid dynamics problems. From the mid-1970s, the required mathematical methodologies began to be understood, and various CFD solvers were developed and appeared in the early 1980s. They actually required the most powerful computers of the era, a deep knowledge of fluid dynamics, and large amounts of time to set up simulations. Consequently, CFD was a tool used almost exclusively in research [ANSYS Inc., 2013].

Recent advances in computing power, along with powerful graphics and interactive 3D manipulation of models, have accomplished the creation of a CFD model and results' analyses in much less time and cost. Advanced solvers enable robust solutions of the flow field in a reasonable time [ANSYS Inc., 2013].

As a result, CFD is now an established and widespread industrial analysis, design and optimization tool, helping to reduce design time and improve processes throughout all the engineering disciplines. CFD provides a cost-effective and accurate alternative to scale model testing, with variations on the simulation being performed rapidly [ANSYS Inc., 2013].

3.2 The Mathematics of CFD

The set of partial differential equations (PDEs) that describe the flow of viscous fluids (compressible or incompressible) are known as the Navier-Stokes equations. These partial differential equations were derived in the early nineteenth century and have no known general analytical solution but can be discretized and solved numerically, with proper numerical methods [ANSYS Inc., 2013].

Equations describing other processes, such as combustion, or other chemical reactions, can also be solved in conjunction with the Navier-Stokes equations. Often, an approximating model is used to derive these additional equations, such as turbulence models. There are a number of different discretization methods, which are

used in CFD codes. The most common, and the one on which ANSYS CFX solver is based, is known as the Finite Volume (FV) method [ANSYS Inc., 2013]. The discretization methods are used in order to transform the partial differential equations to a large set of linear algebraic equations, which can be solved by a computer. In FV technique the region of interest is divided into small sub-regions, called Control Volumes, constructed through the procedure of mesh generation. The equations are discretized and solved iteratively for each Control Volume. As a result, an approximation of the value of each variable at specific points throughout the domain can be obtained. [ANSYS Inc., 2013]. CFD is currently used by engineers and scientists in a wide range of fields. Typical applications include [ANSYS Inc., 2013]:

- **Process industry:** Mixing vessels, chemical reactors.
- **Building services:** Ventilation of buildings.
- **Health and safety:** Investigating the effects of fire and smoke.
- **Motor industry:** Combustion modeling, car aerodynamics.
- **Electronics:** Heat transfer within and around circuit boards.
- **Environmental:** Dispersion of pollutants in air or water.
- **Power and energy:** Optimization of combustion processes.
- **Medical:** Blood flow through grafted blood vessel.

3.3 CFD Methodology

CFD can be used to determine the performance of a component at the design stage, or it can be used to analyze problems with an existing component and lead to its improved design. The process of performing a single CFD simulation is split into the following procedures [ANSYS Inc., 2013]:

- Creating the Geometry and the Computational Mesh.
- Defining the Physics of the Model.
- Solving the CFD Problem.
- Visualizing the Results in the Postprocessor.

Creating the Geometry and the Computational Mesh

The objective of this procedure is to produce a computational mesh inside the flow (computational) domain, for input to the physics preprocessor. Before a mesh can be produced, a closed geometric solid is required to be defined (using CAD tools). The

geometry and mesh can be created in the Meshing application or any of the other geometry/mesh creation tools. The basic steps involve:

- Defining the geometry of the region of interest.
- Creating regions of fluid flow, solid regions and surface boundary names.
- Setting properties for the mesh.

Defining the Physics of the Model

This interactive process is the second pre-processing stage for a CFD simulation and is used to create the proper input data required by the solver. The mesh files are loaded into the physics preprocessor (CFX-Pre in our case). The physical models that are to be included in the simulation are selected. Fluid properties and boundary conditions are also defined [ANSYS Inc., 2013].

Solving the CFD Problem

The program that solves the CFD problem is called the solver; within the solver, the discretization of the PDEs is performed, along with the solution of the resulting system of algebraic equations. It produces the required results in a non-interactive/batch process. More specifically, a CFD problem is solved as follows [ANSYS Inc., 2013]:

- The PDEs are integrated over all the Control Volumes inside the discretized computational domain. This is equivalent to applying a basic conservation law (for example, for mass or momentum) to each control volume (its integral form).
- These integral equations are converted to a system of algebraic equations by generating a set of approximations for the terms in the integral equations.
- The algebraic equations are subsequently solved in an iterative manner.

The iterative approach is required because of the nonlinear nature of the corresponding PDEs, and as the solution approaches the exact solution, it is said to converge. For each iteration and for each family of equations, a residual is reported as a measure of the overall conservation of the flow properties [ANSYS Inc., 2013].

Visualizing the Results in the Postprocessor

The postprocessor is the component used to visualize, analyze and present the results interactively with the user. Examples of some important features of postprocessors are [ANSYS Inc., 2013]:

- Visualization of the geometry and control volumes.
- Vector plots, showing the direction and magnitude of the flow.
- Visualization of the variation of scalar variables (variables that have only magnitude, not direction, such as temperature, pressure and speed) through the domain.
- Quantitative numerical calculations.
- Animation.
- Charts showing graphical plots of variables.
- Hard copy and online output.

3.4 Overview of ANSYS CFX

ANSYS CFX [ANSYS Inc., 2013] is a general purpose Computational Fluid Dynamics (CFD) software suite, which combines an advanced solver with powerful pre-processing and post-processing capabilities. It includes the following features:

- An advanced coupled solver that is both reliable and robust.
- Full integration of problem definition, analysis, and results presentation.
- An intuitive and interactive setup process, using menus and advanced graphics.

ANSYS CFX is capable of modeling:

- Steady-state and transient flows.
- Laminar and turbulent flows.
- Subsonic, transonic and supersonic flows.
- Heat transfer and thermal radiation.
- Buoyancy.
- Non-Newtonian flows.
- Transport of non-reacting scalar components.
- Multiphase flows.
- Combustion.
- Flows in multiple frames of reference.

- Particle tracking.

ANSYS CFX consists of four software modules that take a geometry and mesh and pass the information required to perform a CFD analysis (Fig. 3.1).
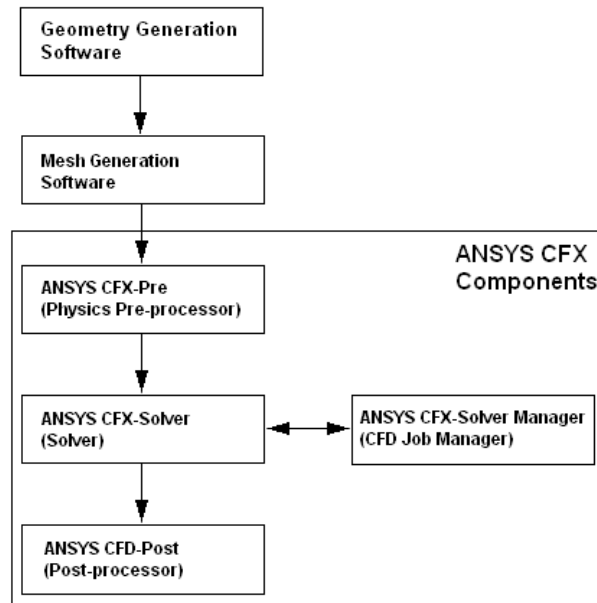

Fig. 3.1: *ANSYS CFX flow chart [ANSYS Inc., 2013].*

3.5 Design Modeler

In the ANSYS CFX Workbench, by clicking the *Import Geometry* and inserting the "stp" file, the Cooling hole domain geometry is imported. The *DesignModeler* starts by clicking *the Edit Geometry **in** DesignModeler* option. Finally, by selecting the **Generate** ⚡ Generate command, the geometry is displayed in the DM.

In order for the simulation results to be more accurate, a local increase in mesh densification should be made at some points considered to be more "critical", e.g. the boundary layer formation area. For this reason, new volumes within the domain should be defined, where increased densification will be applied. In this work, 4 new volumes will be defined within the flow domain.

For creating the first volume at the cooling hole, the following procedure was followed:

- By using the **sketch** 📷 command and **line** command, the schematic was designed (Fig. 3.2).

- The dimensions H1 and H2 were created with the **Horizontal dimension** ⊢⊣ Horizontal command.

- Using the **extrude** command, and by clicking the **generate** button, the final volume was created (Fig. 3.3).

The other three volumes at the main flow and the cooling flow were created following a similar procedure (Fig. 3.4-3.9). Finally, the inlet, outlet, surface and wall surfaces were defined using the **Named selection** command (Fig. 3.10-3.16).
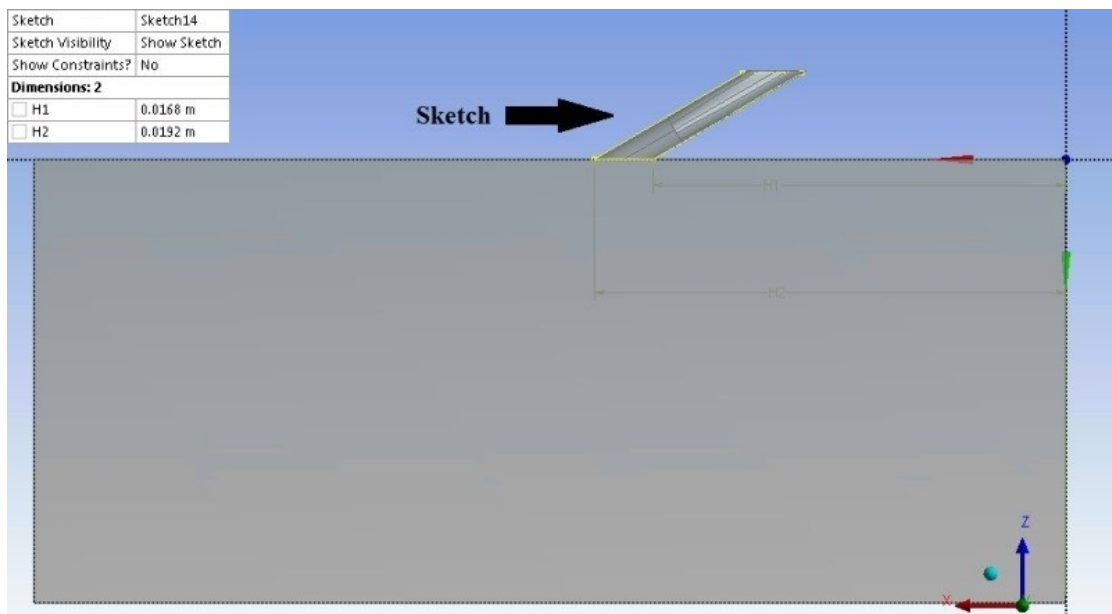
Fig. 3.2: *Cooling hole volume using the **sketch** command.*
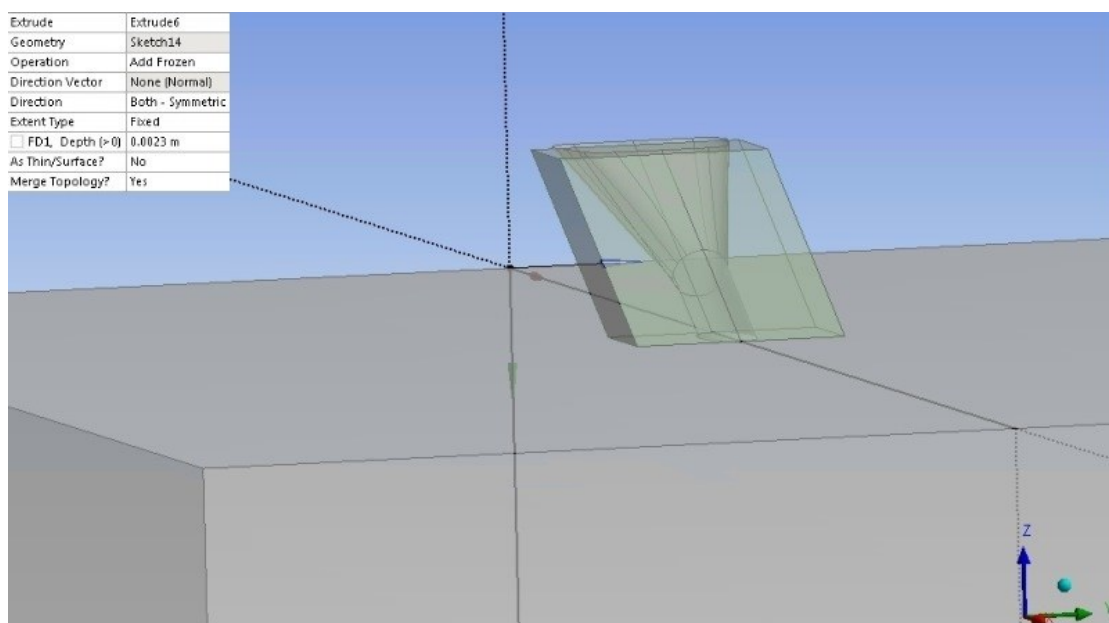
Fig. 3.3: *Cooling hole final volume creation, using **extrude** command.*

H1	0.06 m
H2	0.135 m
V3	0.015 m
V4	0.03 m

Fig. 3.4: *Mainflow volume schematic.*

Extrude	Extrude4
Geometry	Sketch1
Operation	Add Frozen
Direction Vector	None (Normal)
Direction	Normal
Extent Type	Fixed
FD1, Depth (> 0)	0.025 m
As Thin/Surface?	No
Merge Topology?	Yes

Fig. 3.5: *Mainflow volume extrude.*

H5	0.06 m
H6	0.135 m
V7	0.009 m
V8	0.018 m
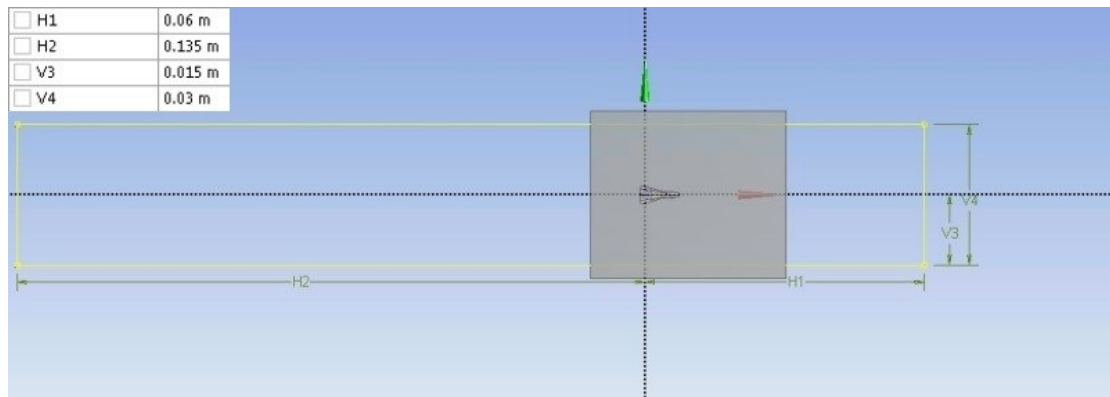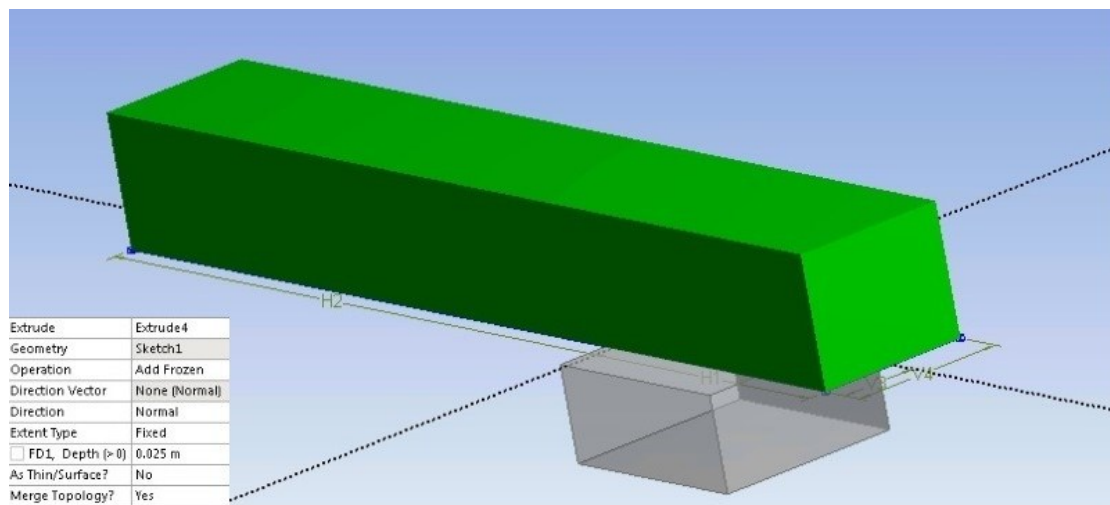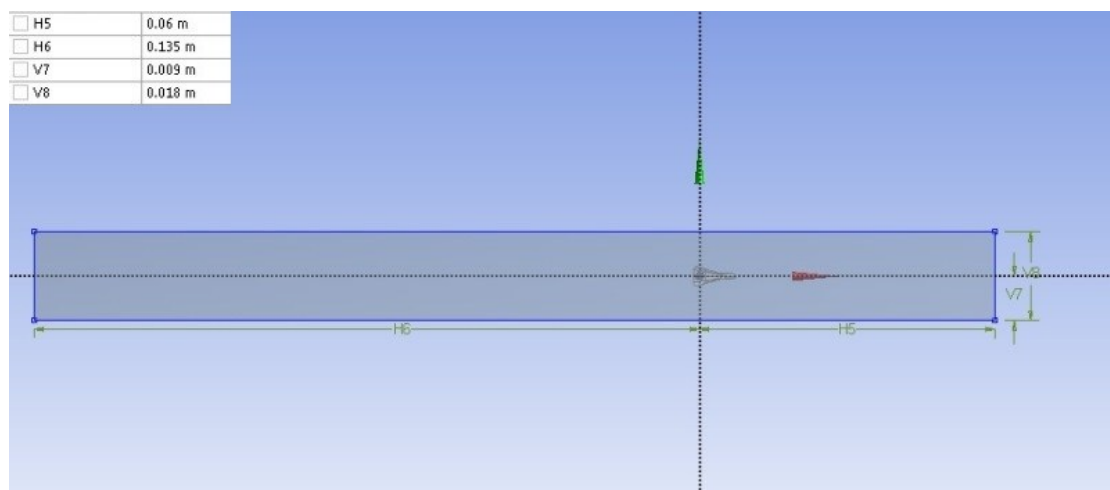
Fig. 3.6: *Second mainflow volume schematic.*
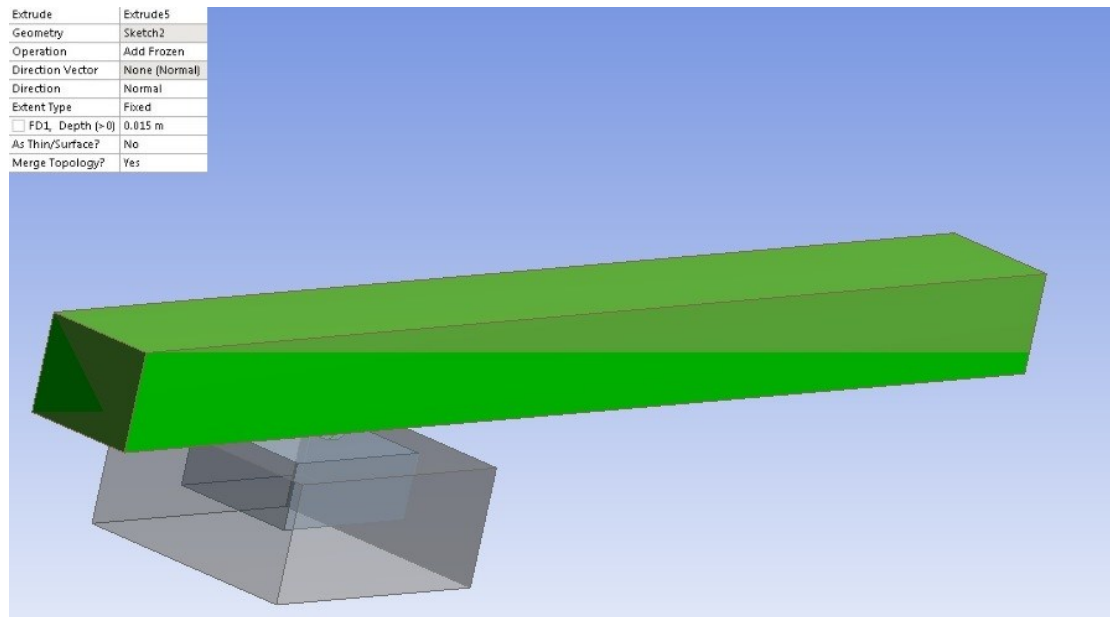
Fig. 3.7: *Second mainflow volume extrude.*
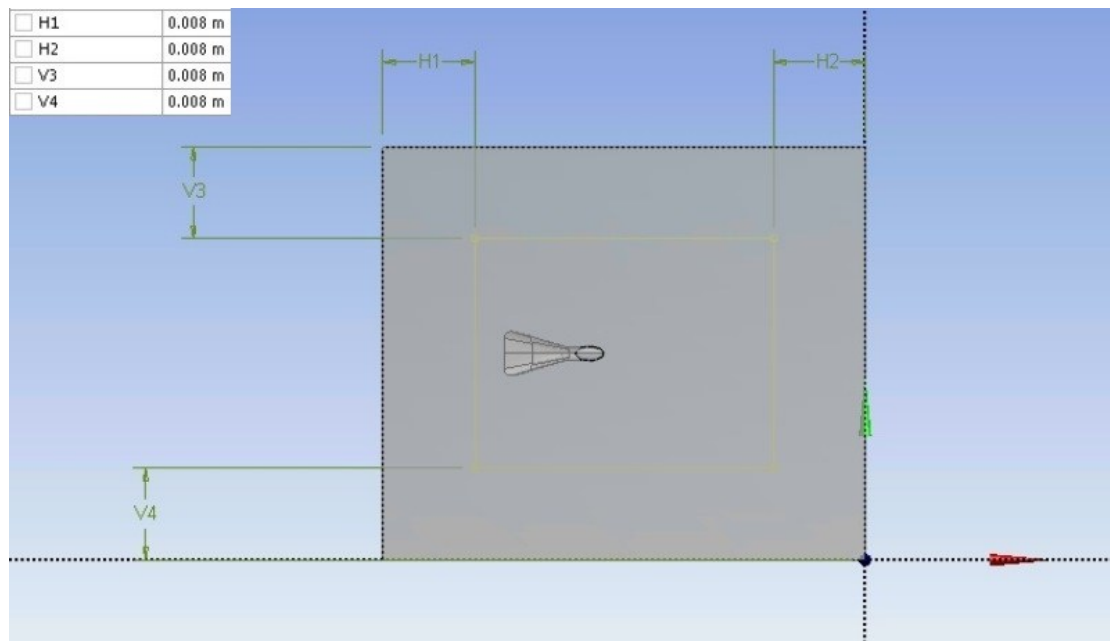
Fig. 3.8: *Cooling flow volume schematic.*

Extrude	Extrude1
Geometry	Sketch5
Operation	Add Frozen
Direction Vector	None (Normal)
Direction	Reversed
Extent Type	Fixed
☐ FD1, Depth (> 0)	0.01 m
As Thin/Surface?	No
Merge Topology?	Yes
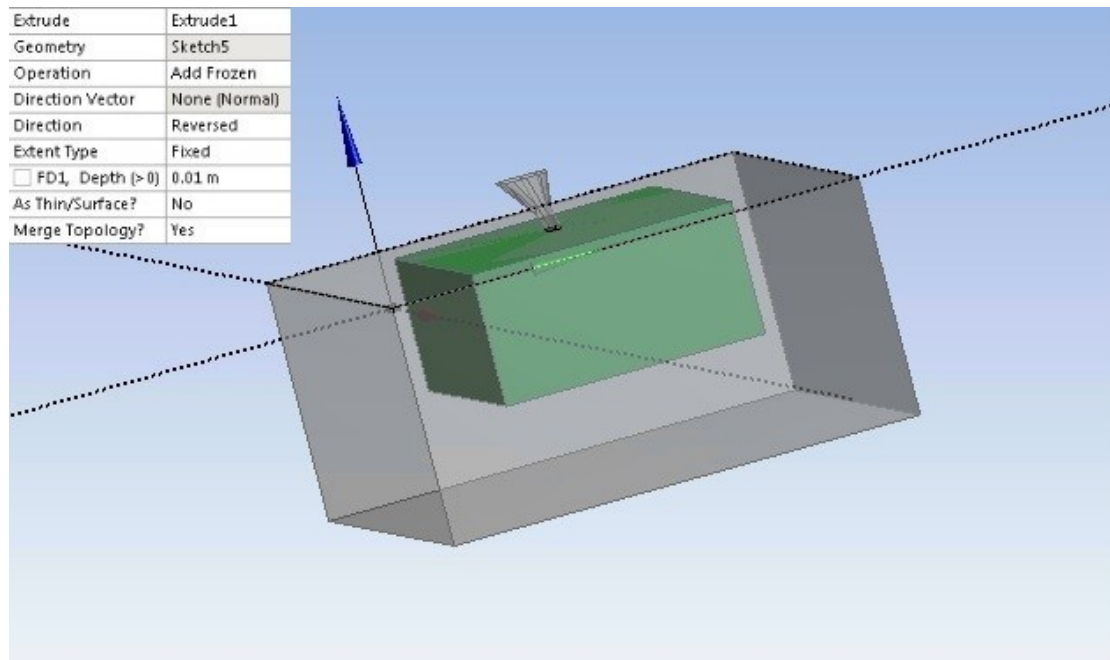
Fig. 3.9: *Cooling flow volume extrude.*
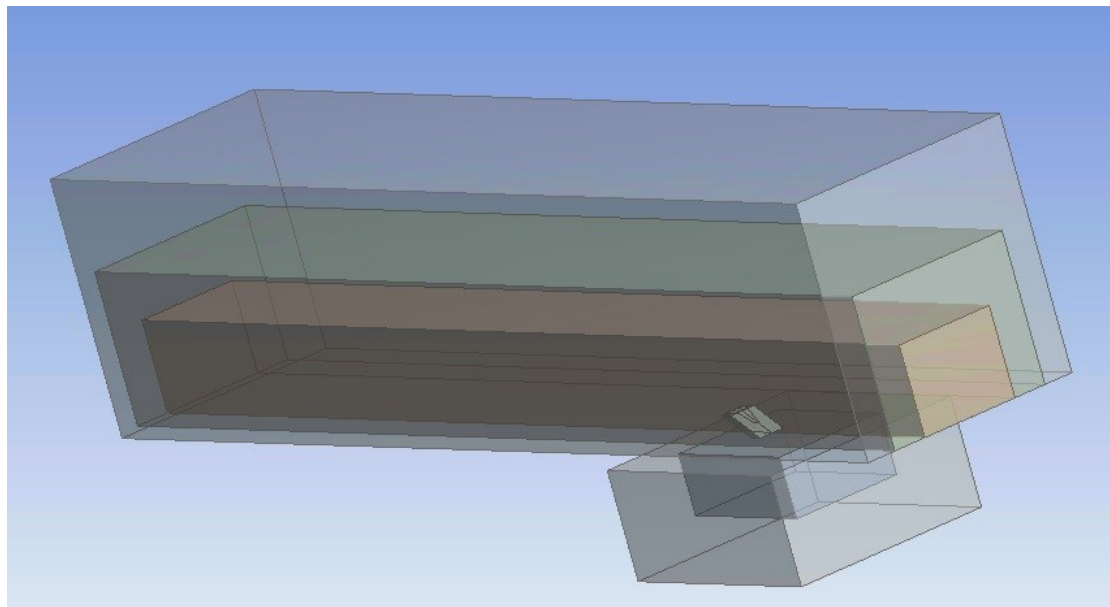
Fig. 3.10: *Final domain.*
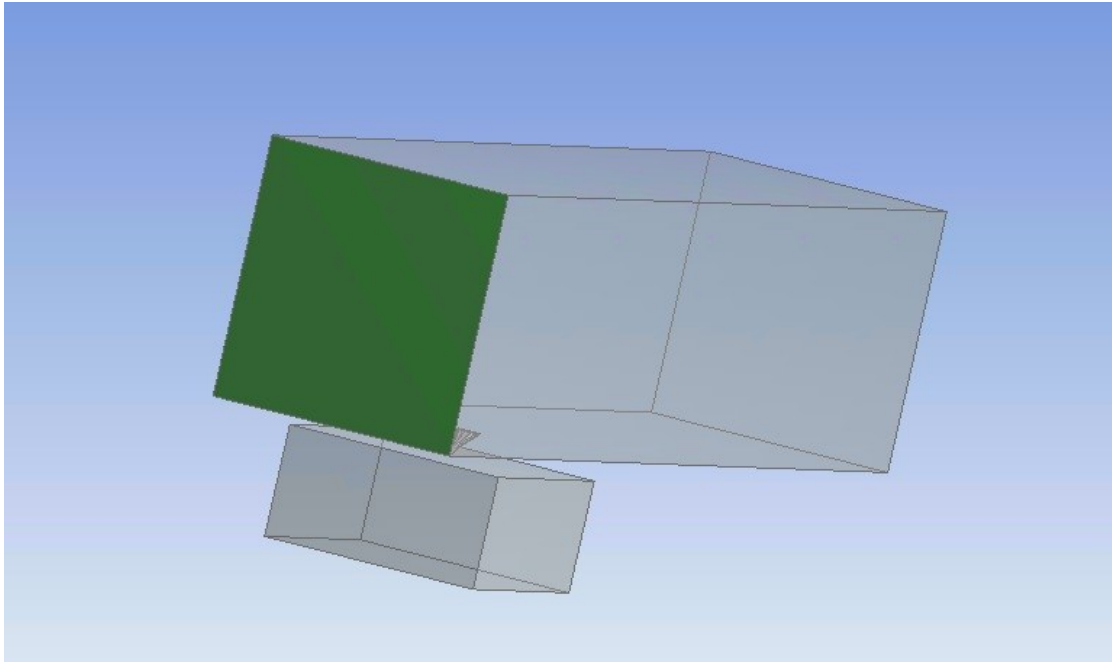
Fig. 3.11: Inlet mainflow surface definition.
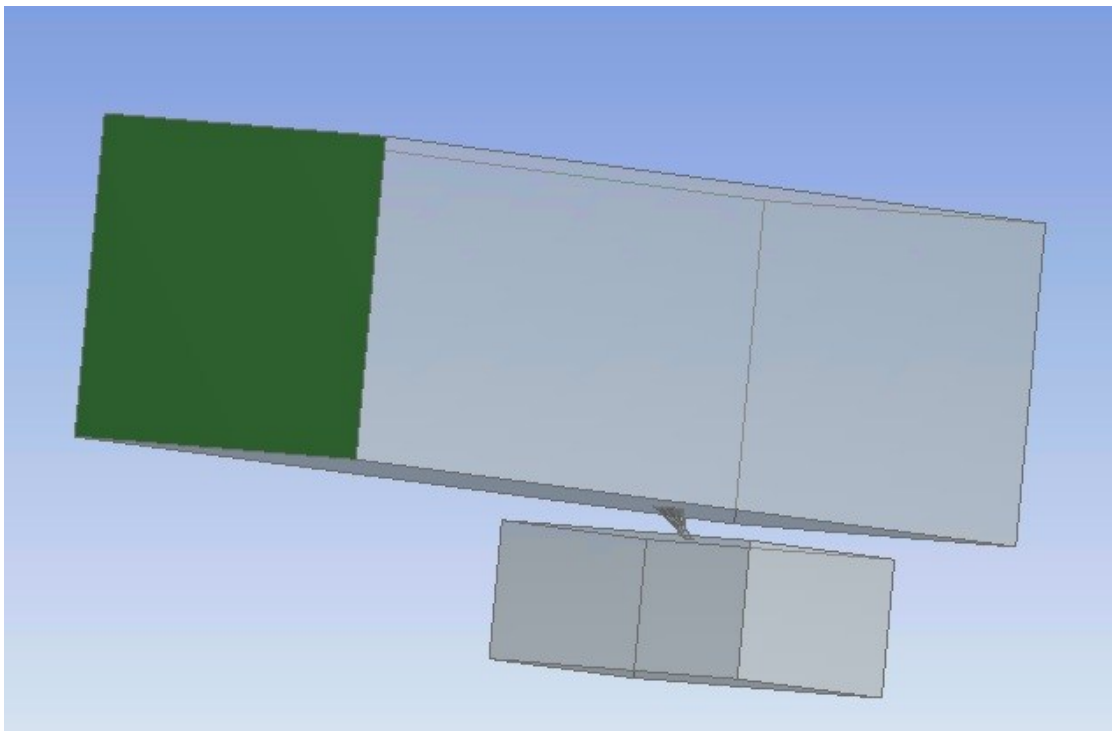
Fig. 3.12: Outlet mainflow surface definition.
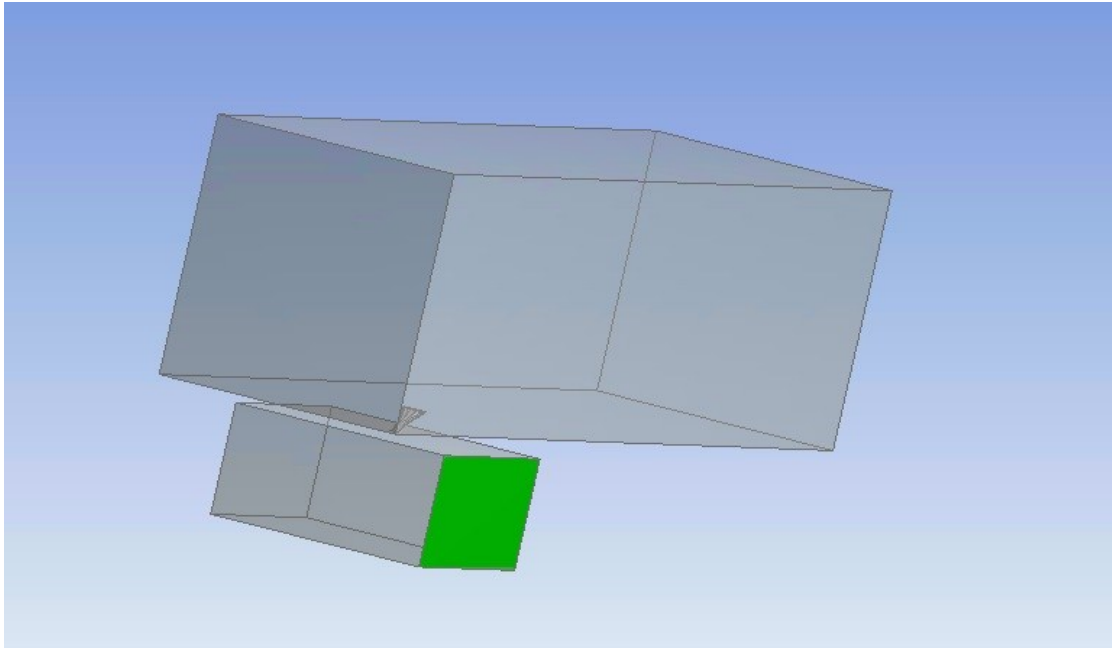
Fig. 3.13: *Inlet cooling flow surface definition.*
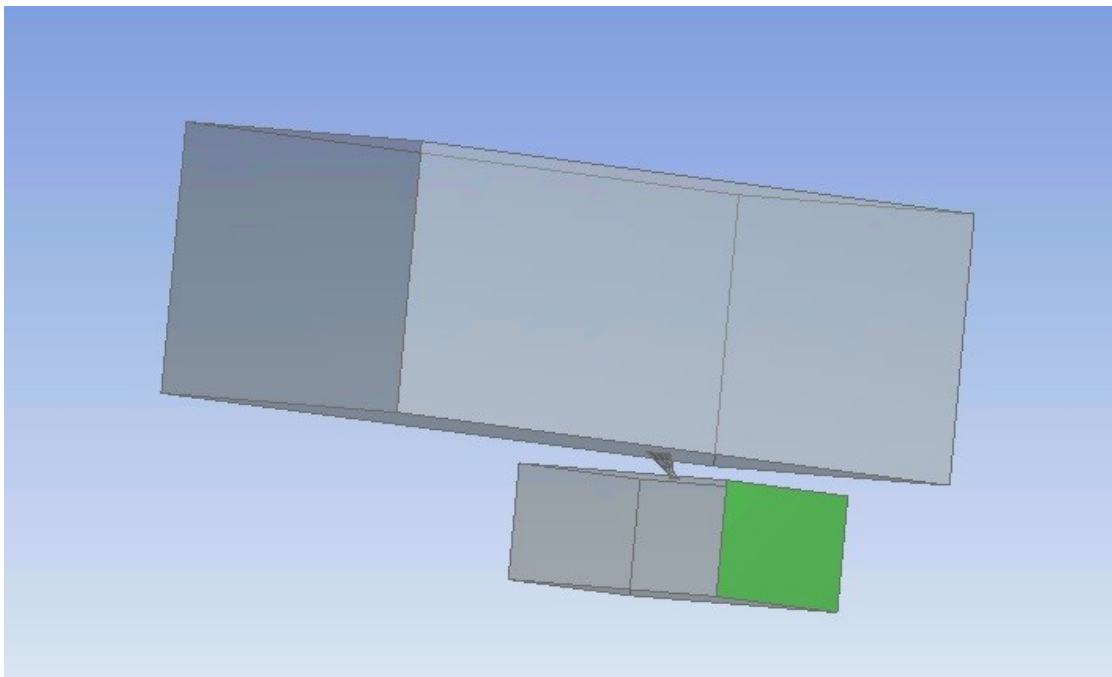
Fig. 3.14: *Outlet cooling flow surface definition.*
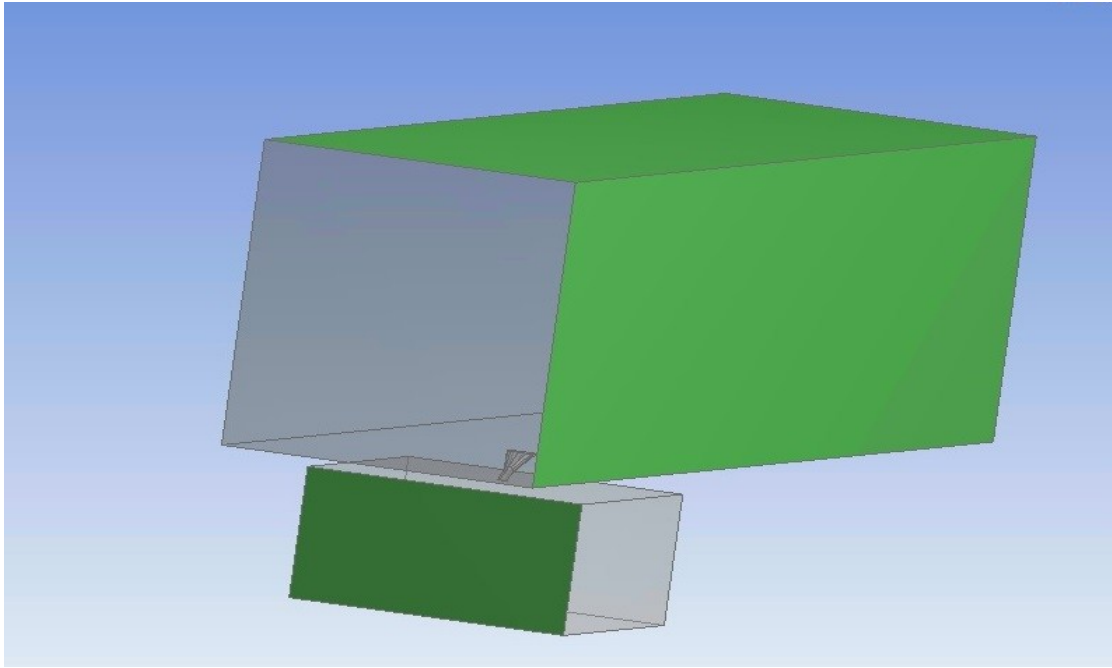
Fig. 3.15: "Surface" surface definition.
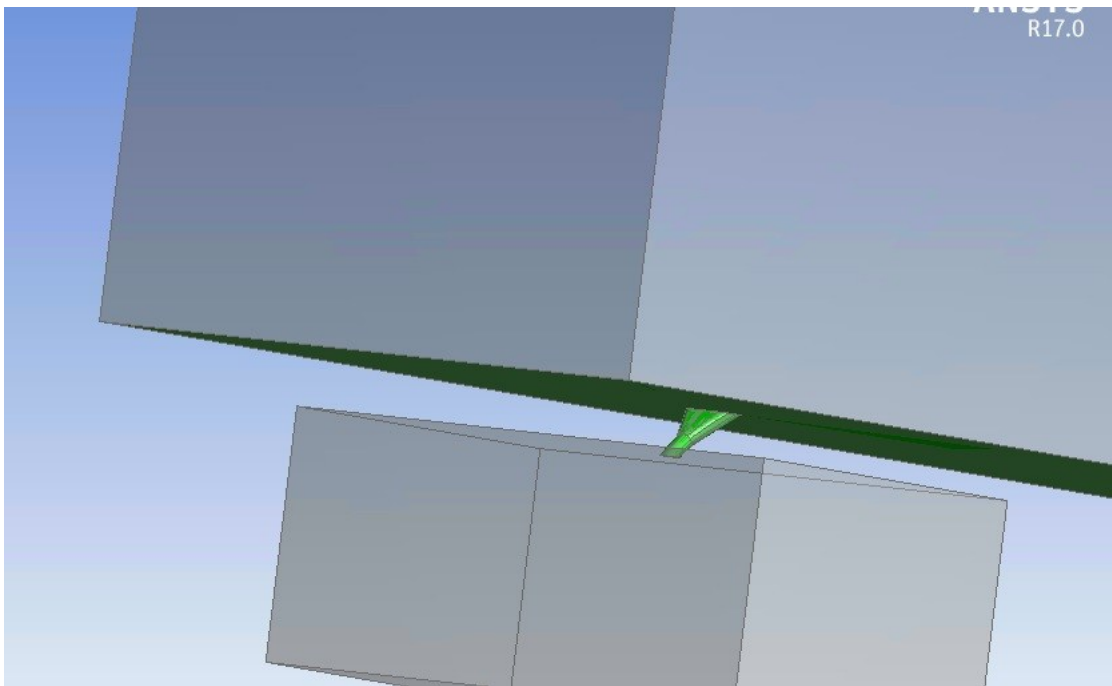
Fig. 3.16: Wall surface definition.

3.6 Mesh Generation

After opening the Mesh generation tool in ANSYS CFX, the first step is to adjust the element size, that is, the thickening of the four volumes designed with DM.

The process followed for the cooling hole volume is the one below:

- By right- clicking *Mesh*, selecting **Insert** and then the **Sizing** command, a new sizing tab is created (Fig.3.17).

- Then, the cooling hole volume is selected as **Geometry.**

- In *Type* tab, the domain is selected as **Body of influence**.

- The **Element size** is adjusted to 0.038 mm (Fig. 3.18).

Similarly, sizing for the remaining volumes is created (Fig. 3.19, Fig. 3.20, and Fig. 3.21). The sizing of the domain is determined using the default options and the growth rate set by the software (Fig. 3.22). Last, the procedure below was followed for the inflation:

- By selecting the *Mesh* tab, and expanding the *Inflation* tab, the named selection *Wall* is selected as **All faces in named selection**.

- A **Smooth Transition** is selected as *Inflation option*, and the **Transition ratio**, **Maximum layers**, **Growth rate**, are adjusted to **0.6**, **16** and **1.25** respectively (Fig. 3.23).

The mesh is created by clicking **Generate Mesh** (Fig. 3.24 - 3.29). For a more detailed mesh observation, the **New Section Plane** command was used for the "cut" of the domain at various "critical" points.
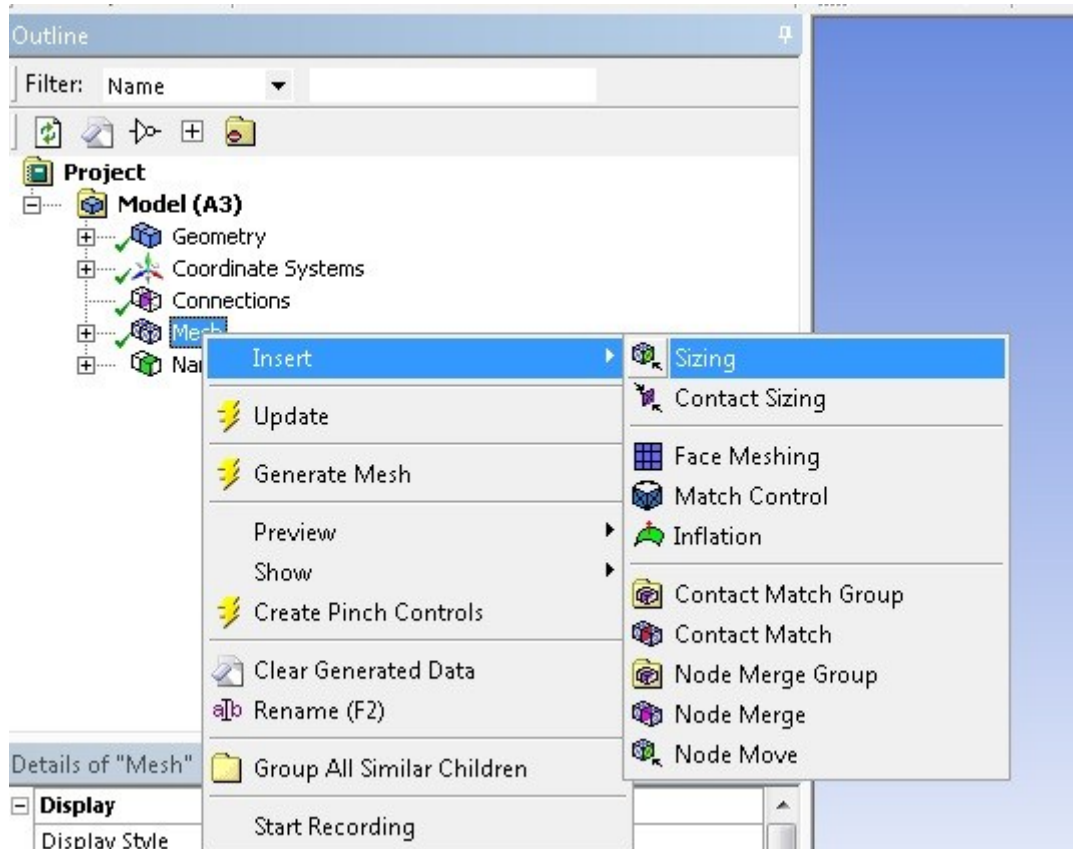
Fig. 3.17: *Sizing command.*
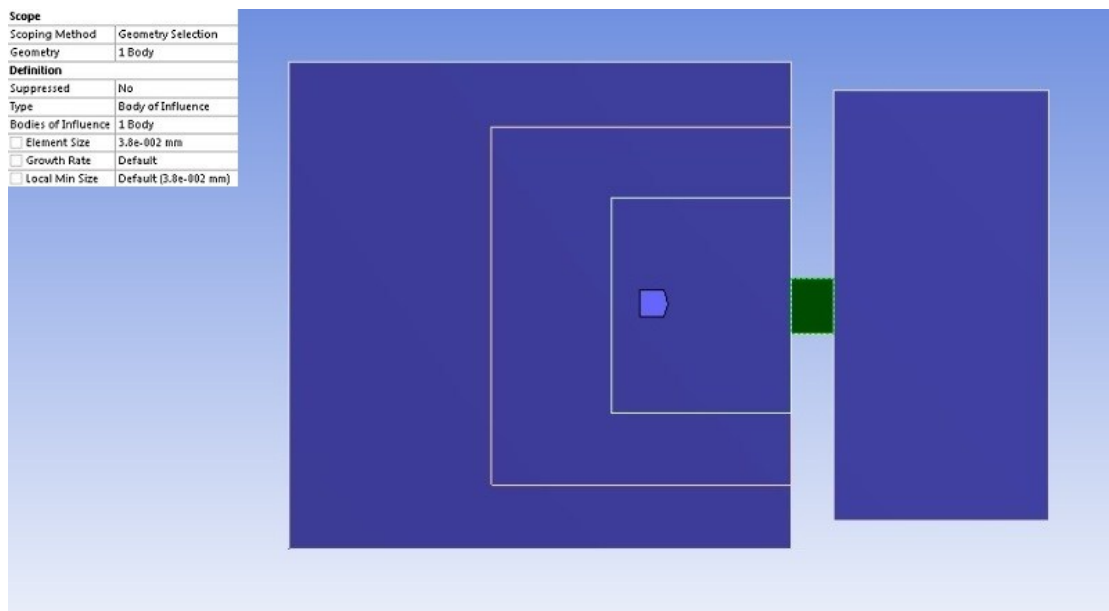
Fig. 3.18: *Cooling hole volume sizing.*
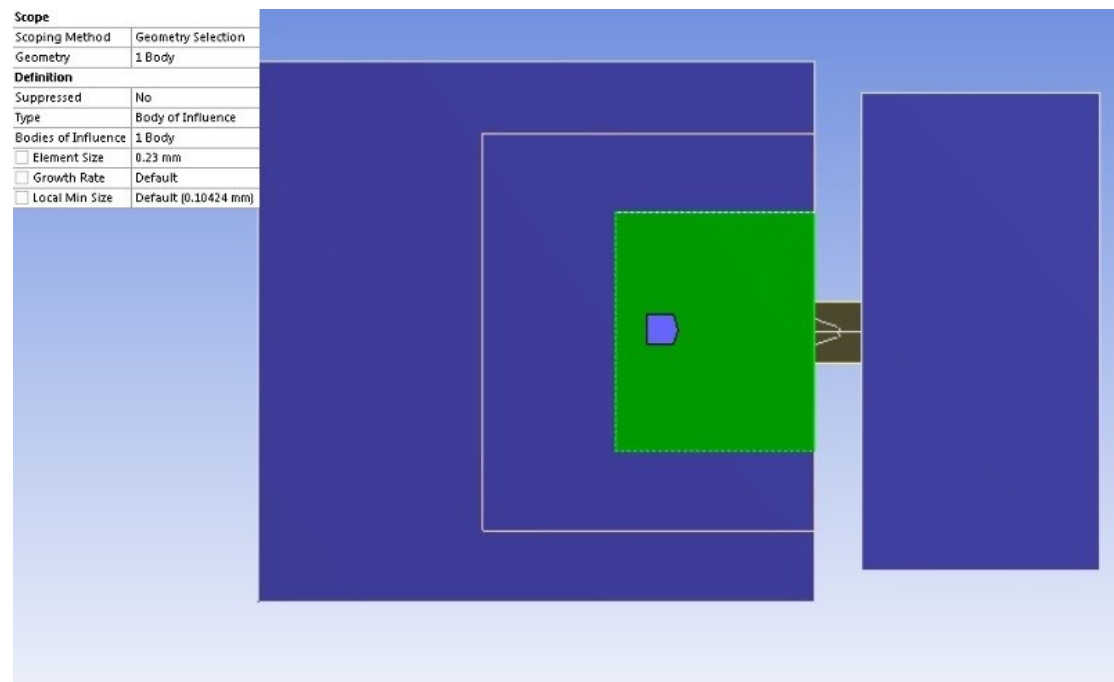
Fig. 3.19: *Mainflow small volume sizing.*
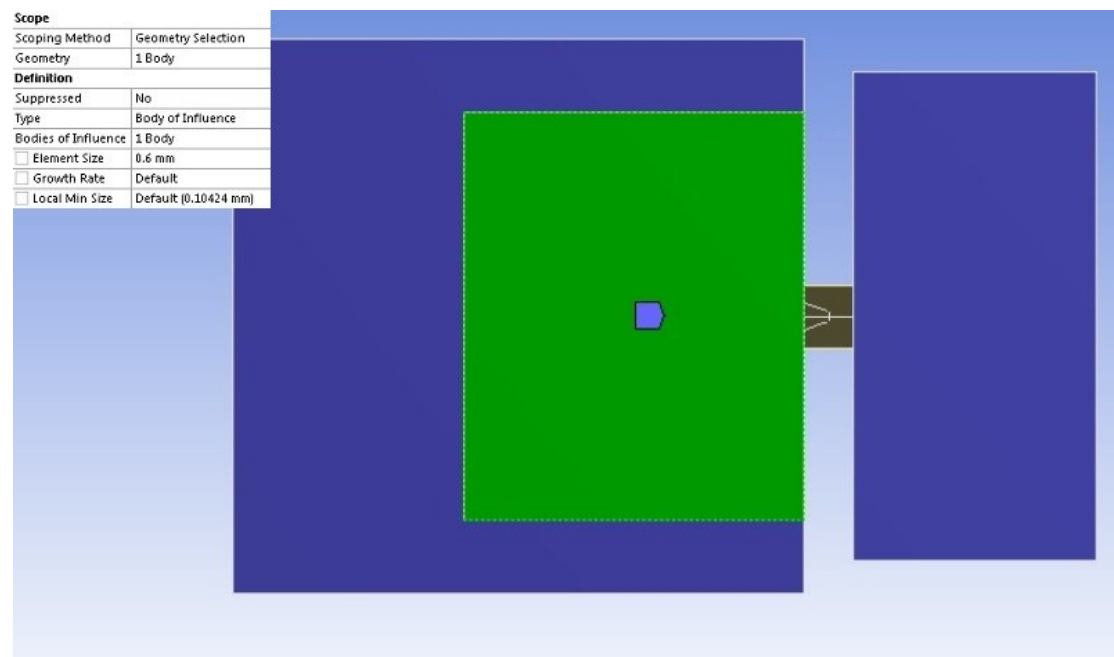
Fig. 3.20: *Mainflow large volume sizing.*
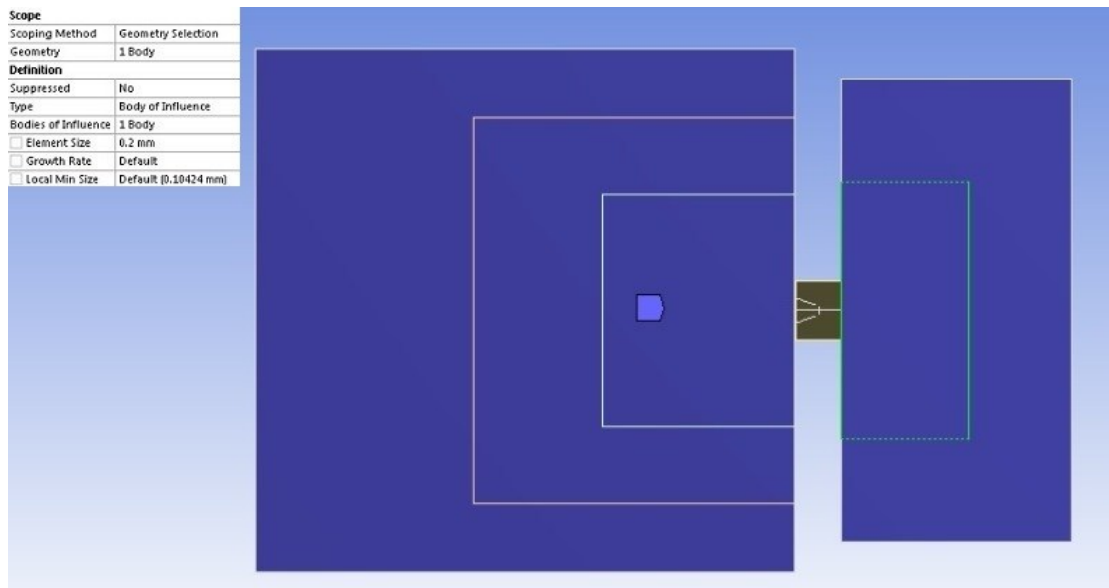
Fig. 3.21: *Cooling flow volume sizing.*

Fig. 3.22: *Mesh sizing and inflation details.*
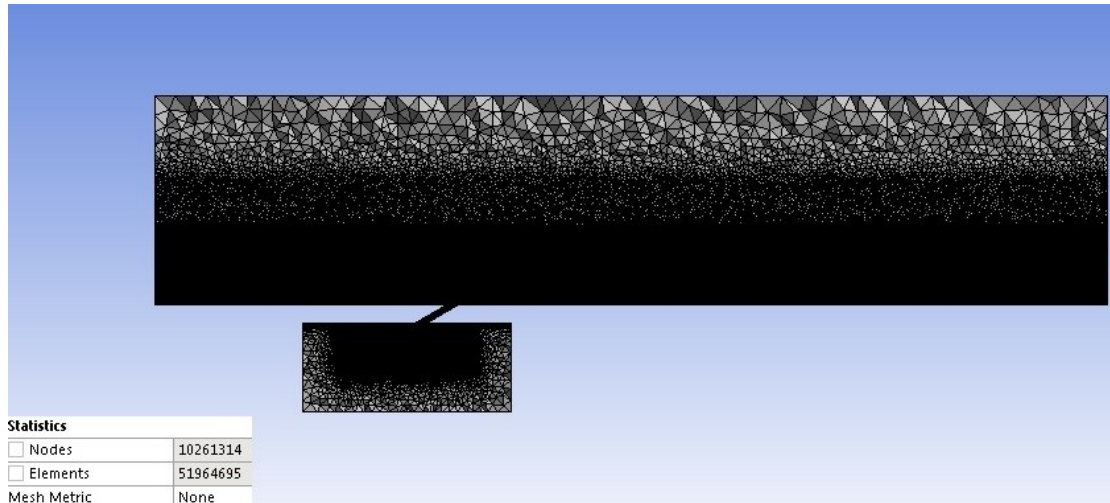
Fig. 3.23: *Final mesh and details.*
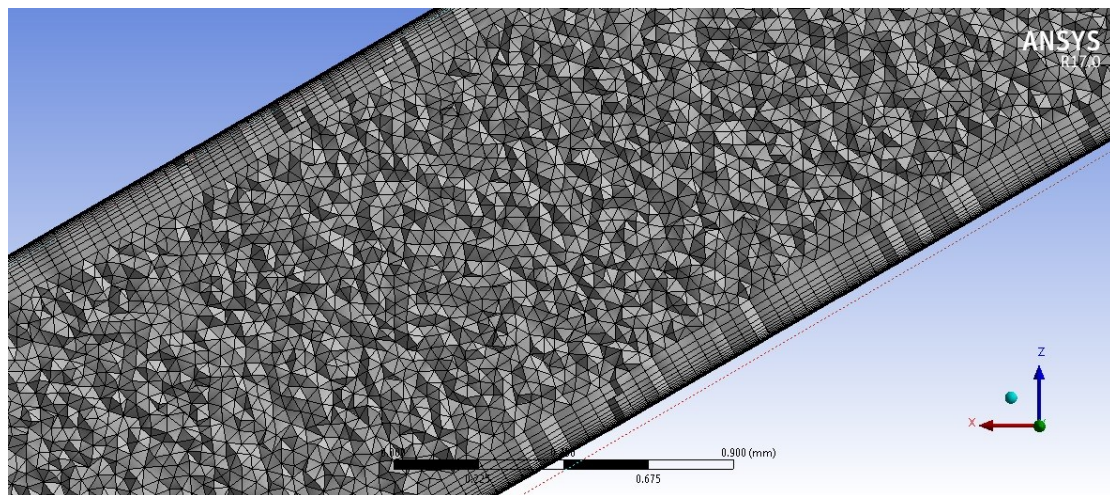
Fig. 3.24: *Cooling hole mesh details.*
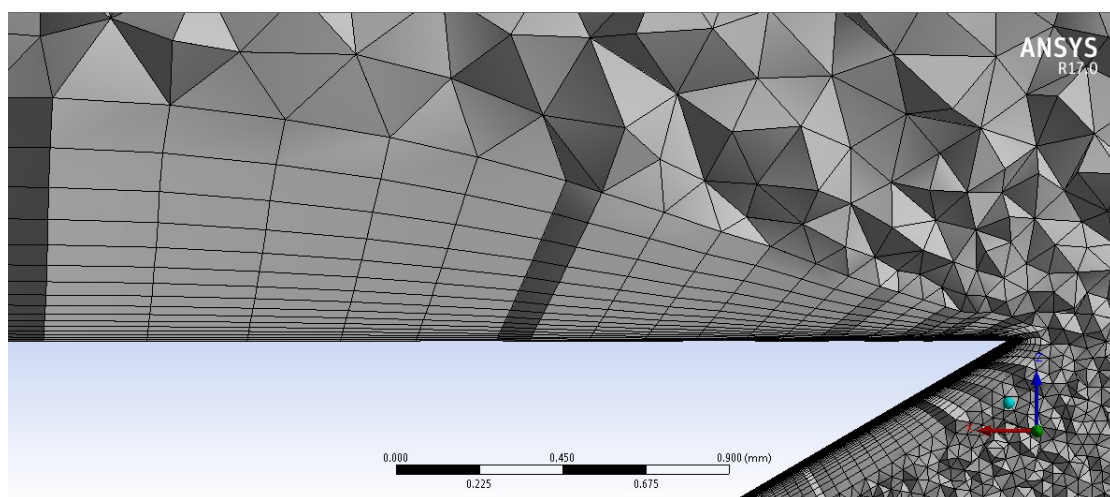
Fig. 3.25: *Cooling hole exit mesh details (1 of 2).*
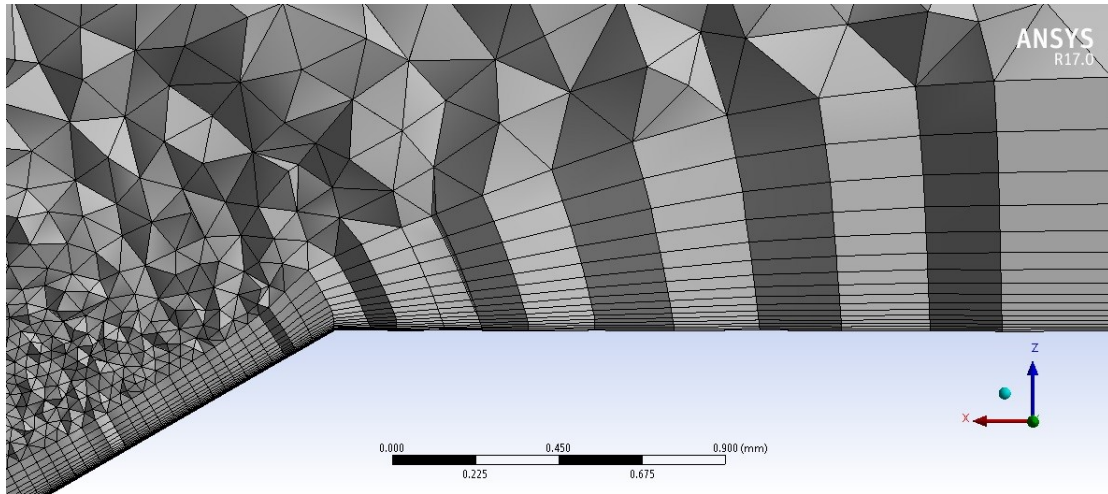
Fig. 3.26: *Cooling hole exit mesh details (2 of 2).*
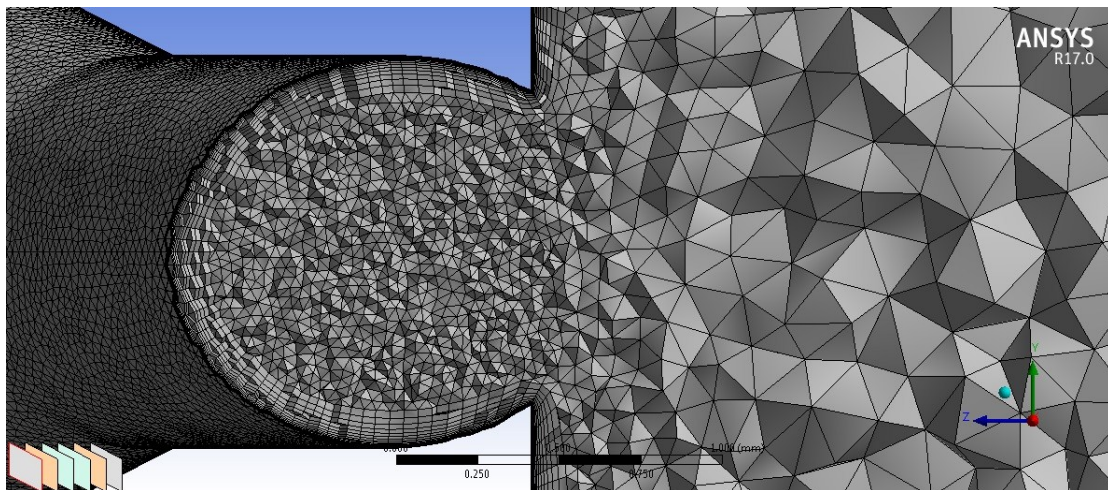
Fig. 3.27: *Cooling hole entrance mesh details.*
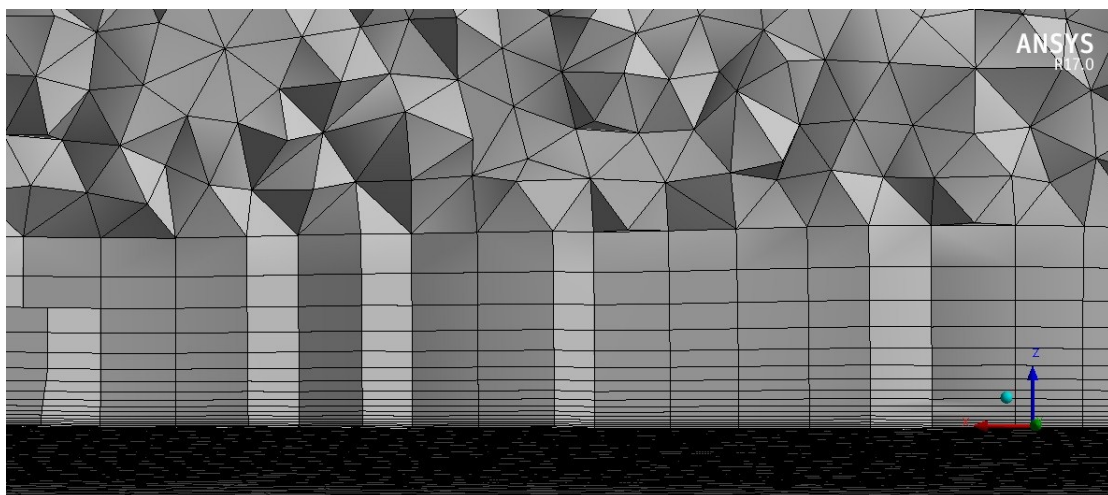
Fig. 3.28: *Mainflow mesh.*
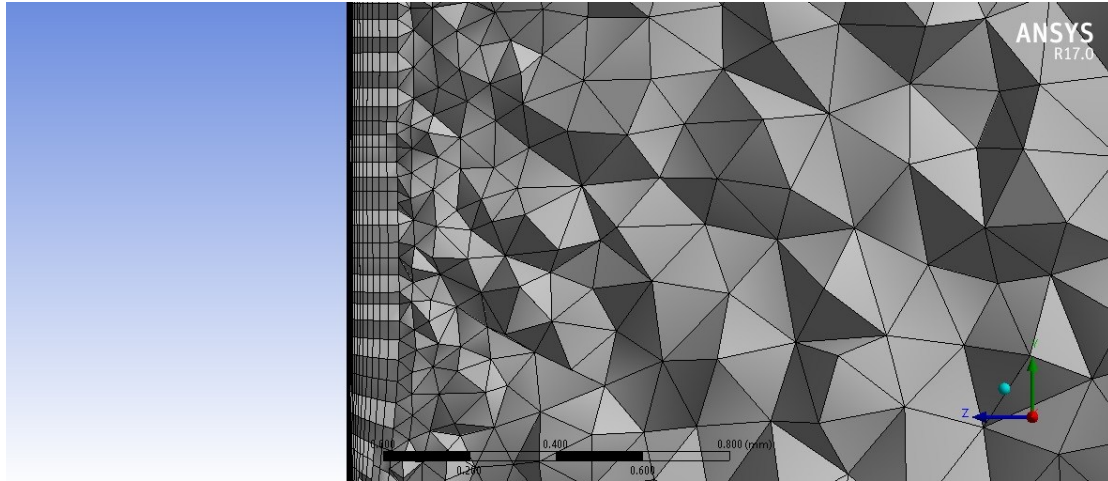
Fig. 3.29: *Cooling flow mesh.*

3.7 Simulation setup

Before conducting the simulation, the boundary conditions of the problem, as well as the heat transfer models, the turbulent models and the residual target levels should be defined.

Initially, by selecting the **Quick setup mode** Quick Setup Mode. option, the following were defined (Fig. 3.30):

- A **single phase** problem, using air **ideal gas** as a liquid, was selected.
- A **steady state** simulation was selected, with *reference pressure* value set to **0 Pa**.
- The **Total Energy equation** was selected as a *heat transfer model*.
- The *turbulence model* selected was the **Shear Stress Transport** model.
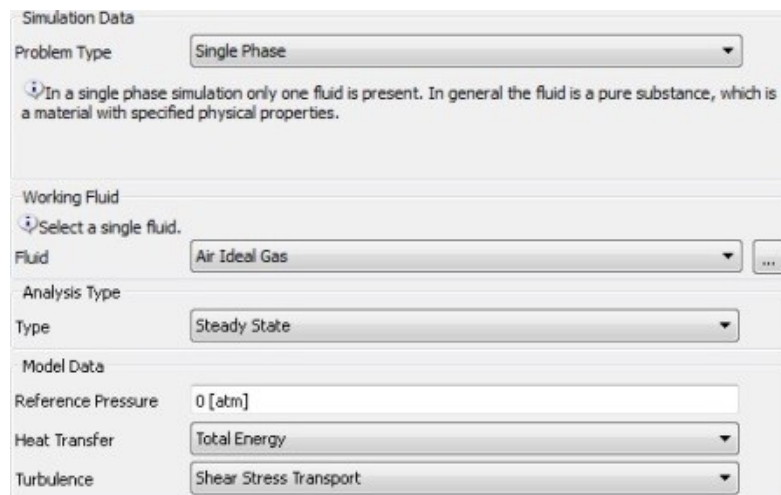
Fig. 3.30: *Simulation data and equation models definition.*

After determining the above, the next step is to define the boundary conditions for the simulation. Six boundaries were defined (one boundary surface for each named selection in Design Modeler):

- The *inlet boundaries* were *Inlet coolant flow* and *inlet Mainflow*, where **Total pressure** and **Total Temperature** were defined.
- The *outlet boundaries* were *outlet Cooling flow* and *outlet Mainflow*, where **static pressure** was defined.
- The *Wall* boundary was selected as **No slip wall,** with **Smooth Wall roughness** and **adiabatic** option was defined.
- The *Surface* boundary was selected as **Free slip wall**.

Four test cases were simulated in total (Table 3.1). The first test case was conducted for validation study purposes, based on the experimental results in [Saumweber, et al., 2008], and the other three simulations were conducted using data from [Han, et al., 2013]. The final boundary conditions for each one of the four cases were generated through the "trial and error" process, with the aim of achieving the desired blowing ratio and density ratio. Further details for the calculation of the boundary conditions is given in Appendix A.

The residual target was set to 10^{-6}, the parallel process procedure was defined, with 8 processors working (Fig. 3.31, Fig. 3.32).

Table 3.1: *Test cases boundary conditions.*

Test case	Mainflow Total Pressure (Pa)	Cooling flow Total Pressure (Pa)	Mainflow Total Temperature (K)	Cooling flow Total Temperature (K)	Mainflow Mach Number	Cooling flow Mach Number
1	1 bar	0.96 bar	500	290	0.3	0
2	3,150,000	3,339,000	1700	1037	0.3	0.29
3	3,150,000	3,559,500	1700	1105	0.3	0.29
4	3,150,000	4,189,500	1700	1292	0.3	0.29
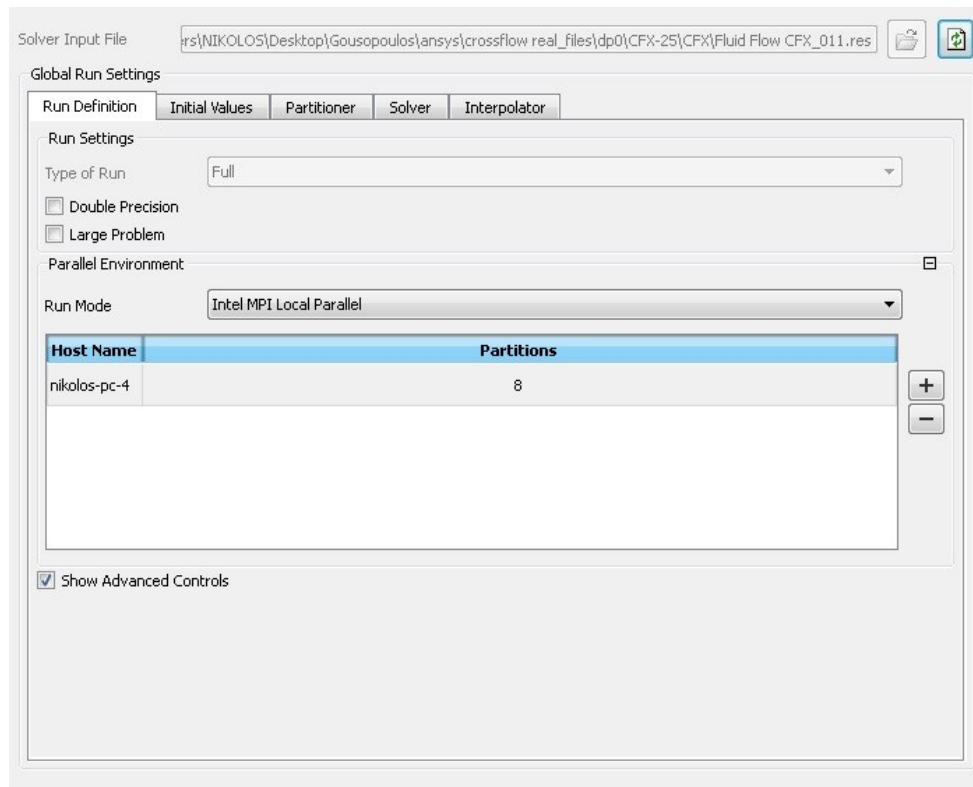
Fig. 3.31: *Simulation details.*
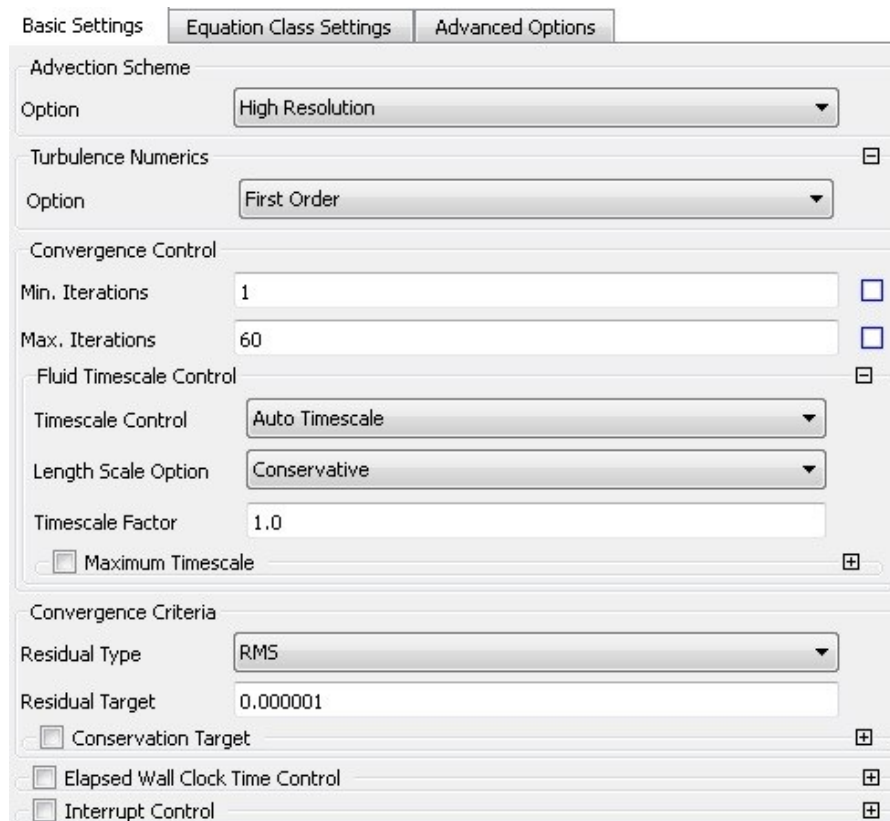
Fig. 3.32: *Solution setup details.*

Chapter 4: Simulation Results

4.1 Numerical Method Validation

The test case 1 convergence is shown in Fig. 4.1. As it can be seen, the convergence is satisfactory. Various contours and graphs were created in the following locations:

- A calculated 2D velocity field was created 2xD downstream of the cooling hole entrance (Fig. 4.2).

- A combination of Temperature contour and calculated velocity field was created 2xD downstream of the cooling hole exit (Fig. 4.3).

- Velocity and Mach number contours in the domain's symmetry plane (Fig. 4.4).

- An adiabatic effectiveness contour in the mainflow wall surface (Fig. 4.5).
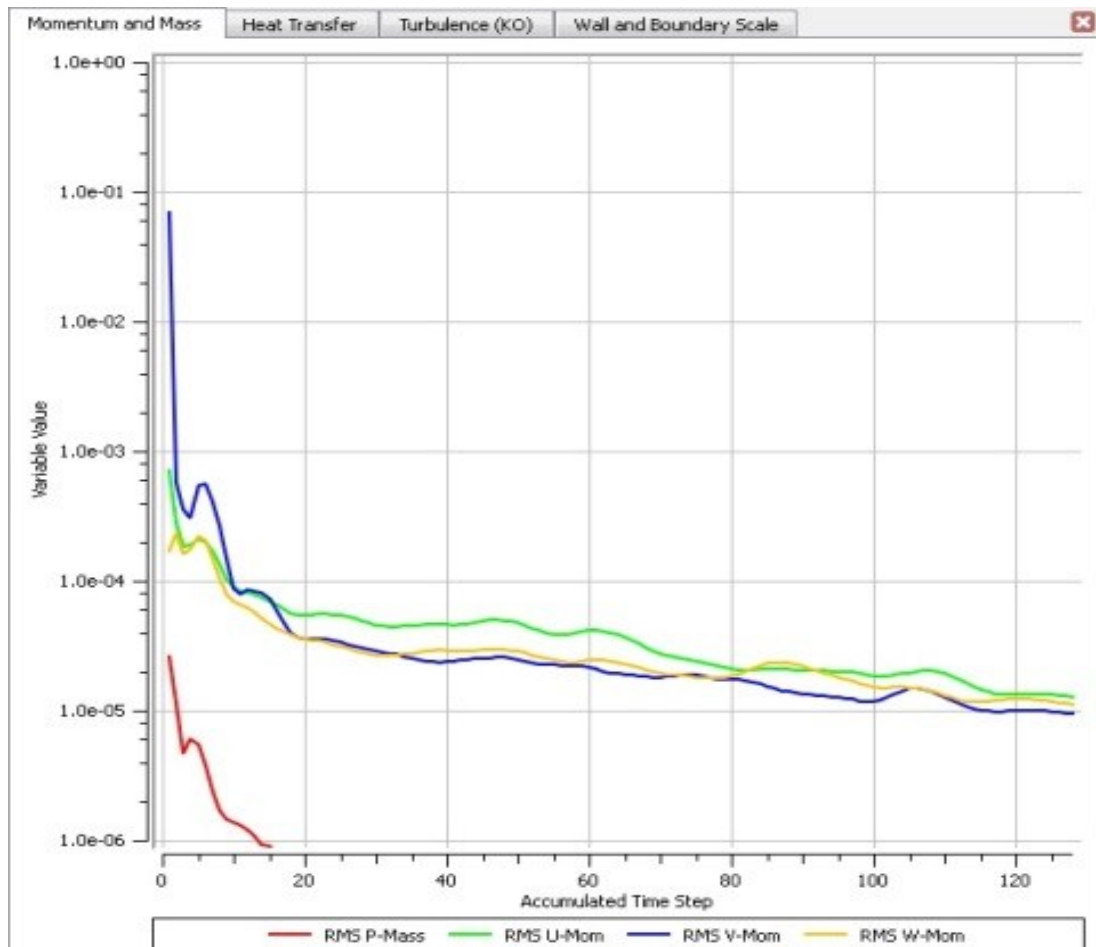
Fig. 4.1: *Test case residuals graph (M=0.5). After this number of iterations, unsteadiness was observed; therefore the run was terminated.*

Fig. 4.2: *Calculated velocity field 2xD downstream of the cooling hole entrance (M=0.5).*

Fig. 4.3: *Temperature and calculated velocity field 2xD downstream of the cooling hole exit (M=0.5).*

Fig. 4.4: *a) velocity, and b) Mach number contours in the domain's symmetry plane*
(M=0.5).
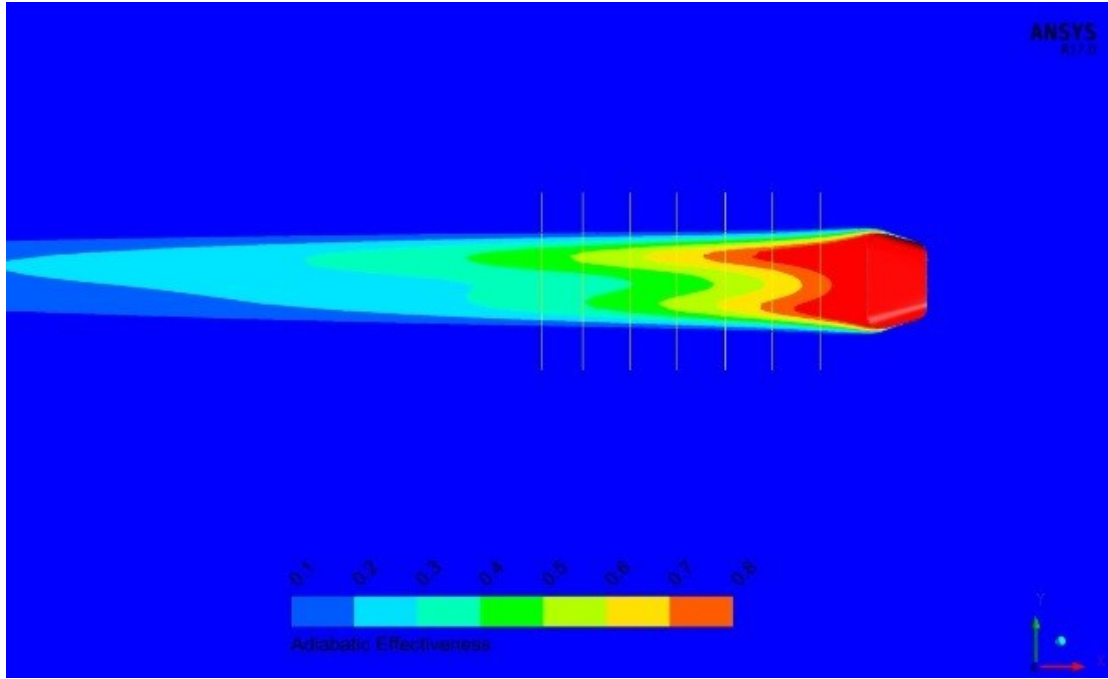
Fig. 4.5*: Adiabatic effectiveness contour in the mainflow wall surface (M=0.5).*

From the figures shown above, it is evident that the simulation's results come to an agreement with [Saumweber, et al., 2008] results. For a more detailed comparison, however, the adiabatic effectiveness versus x/D (distance from cooling hole exit, divided by hole's diameter) graph was constructed (Fig. 4.6). The analytical method of calculating adiabatic efficiency, blowing ratio and density ratio, is presented in Appendix B. The average deviation, from the aforementioned paper results in Fig. 4.6, is below 5% (Appendix B).
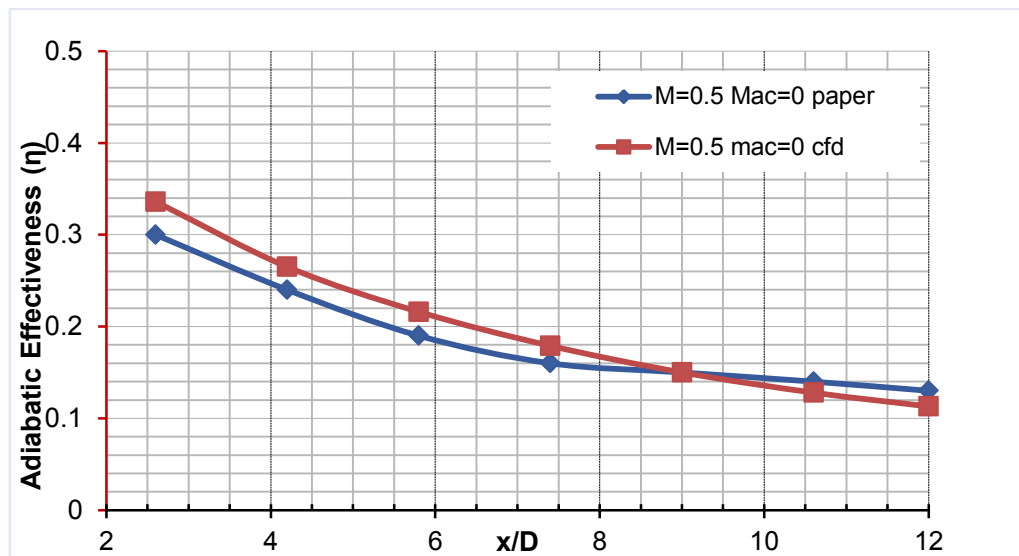
Fig. 4.6: *Adiabatic effectiveness – x/D graph (M=0.5).*

4.2 Operational conditions test cases

Since it has been established that the phenomena of the experiment can be simulated satisfactorily, the next step is to run simulations in similar conditions. Specifically, three more test cases were simulated based on data from [Lee, et al., 2009] and [Han, et al., 2013], so that the operating conditions of a twin-spool low bypass turbofan engines can be simulated. Due to the fact that the data contained in sources from open literature are incomplete for the specific type of jet engine, some assumptions were made, in order to simplify the simulation. Hence, the results obtained were also compared with those in [Saumweber, et al., 2008], in order to assure that the results were not altered due to the assumptions made (Fig. 4.7- 4.22). The results from the three test cases are presented below:

Test Case 2 (Blowing Ratio M=1)
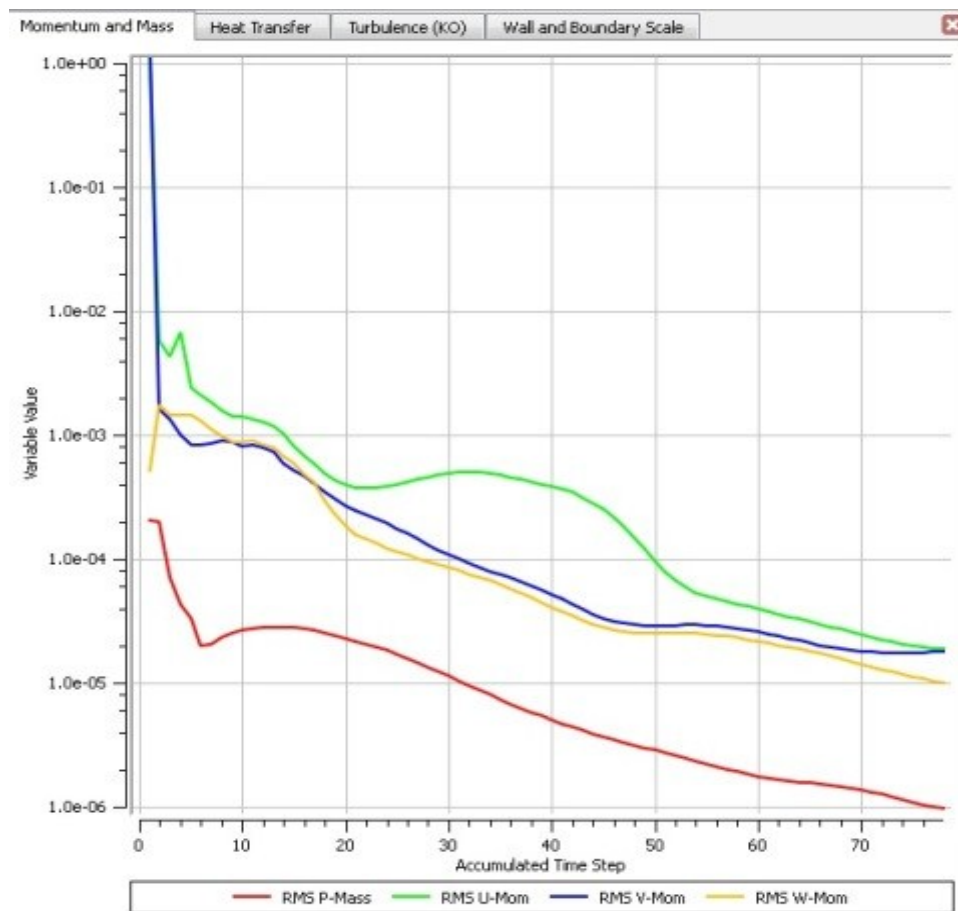
Fig. 4.7: *Test case residuals graph (M=1).*
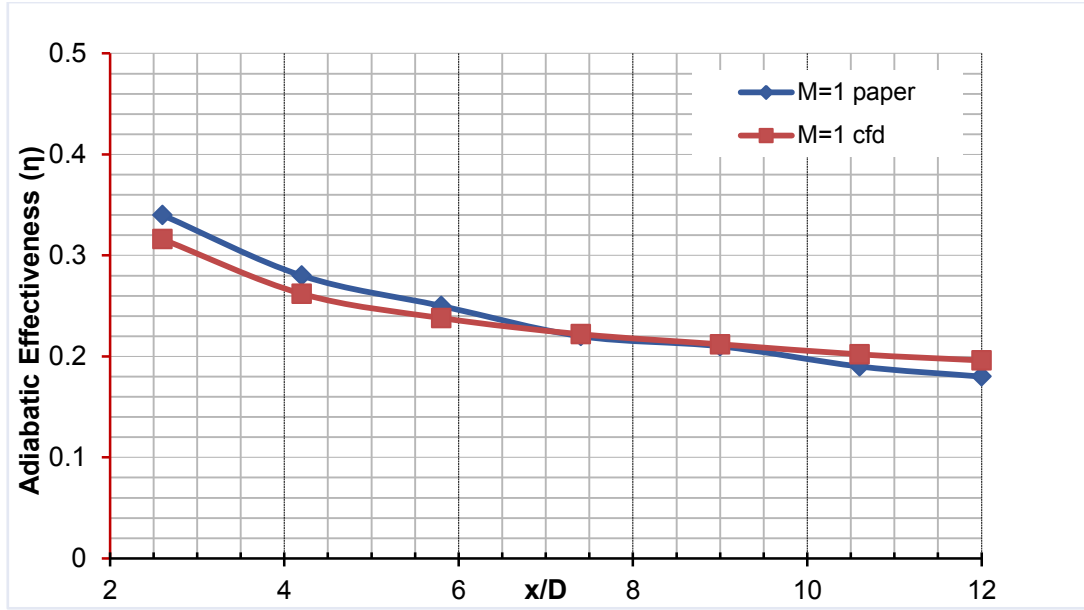
Fig. 4.8: *Adiabatic effectiveness versus x/D (M=1).*
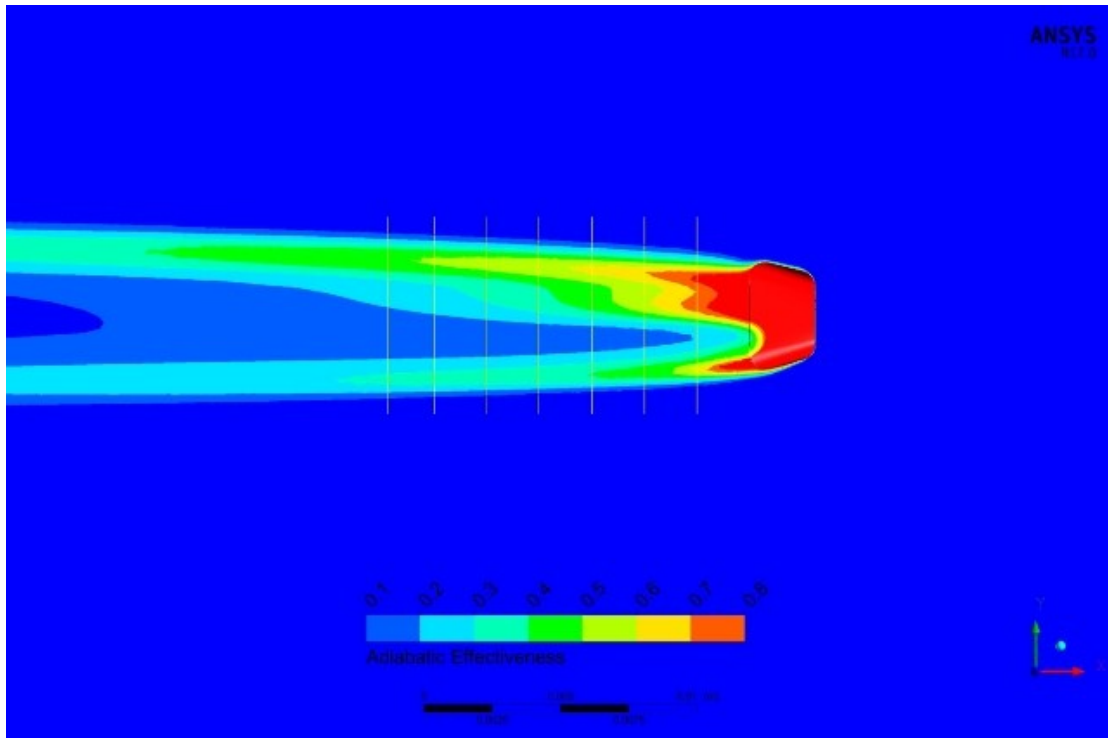
Fig. 4.9: *Adiabatic effectiveness contour in the mainflow wall surface (M=1).*
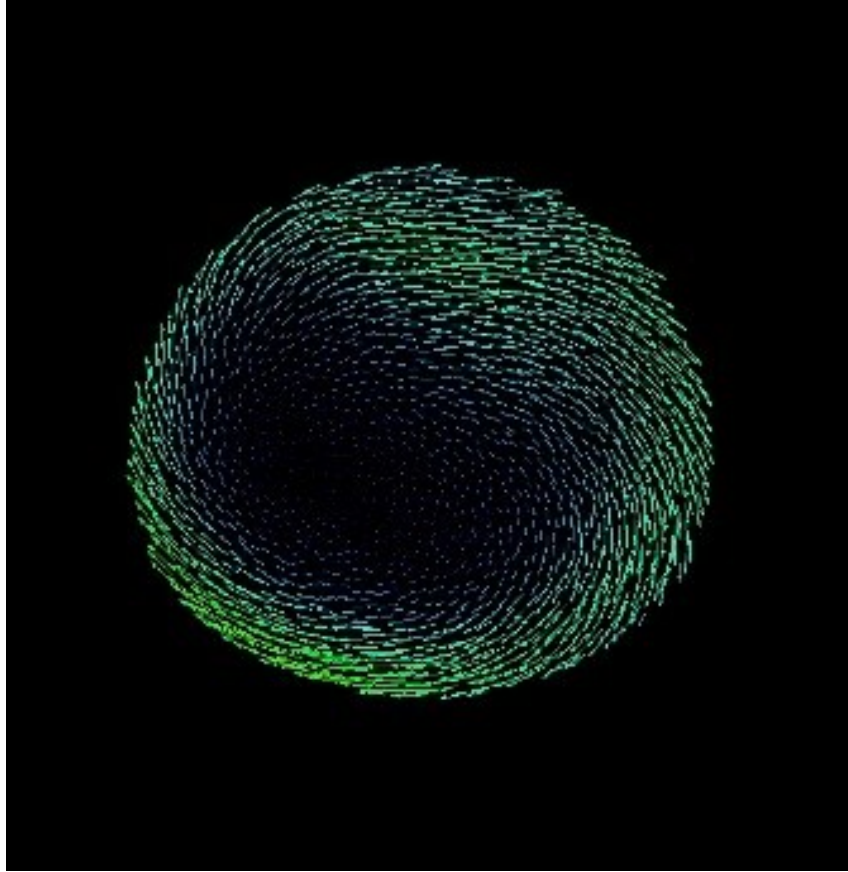
Fig. 4.10: *Calculated velocity field 2xD downstream of cooling hole entrance (M=1).*
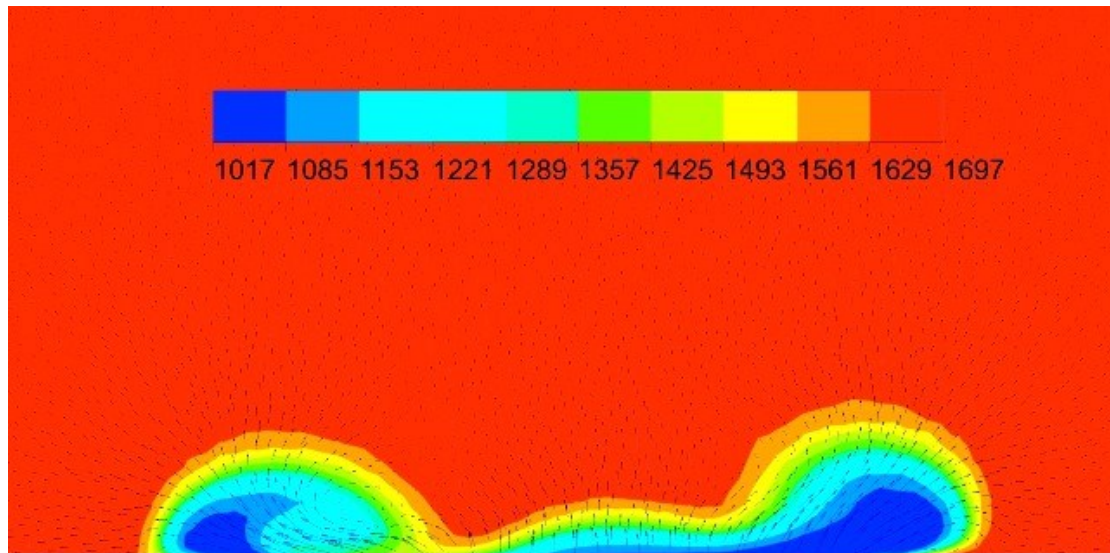
Fig. 4.11: *Temperature and calculated velocity field 2xD downstream of the cooling hole exit (M=1).*
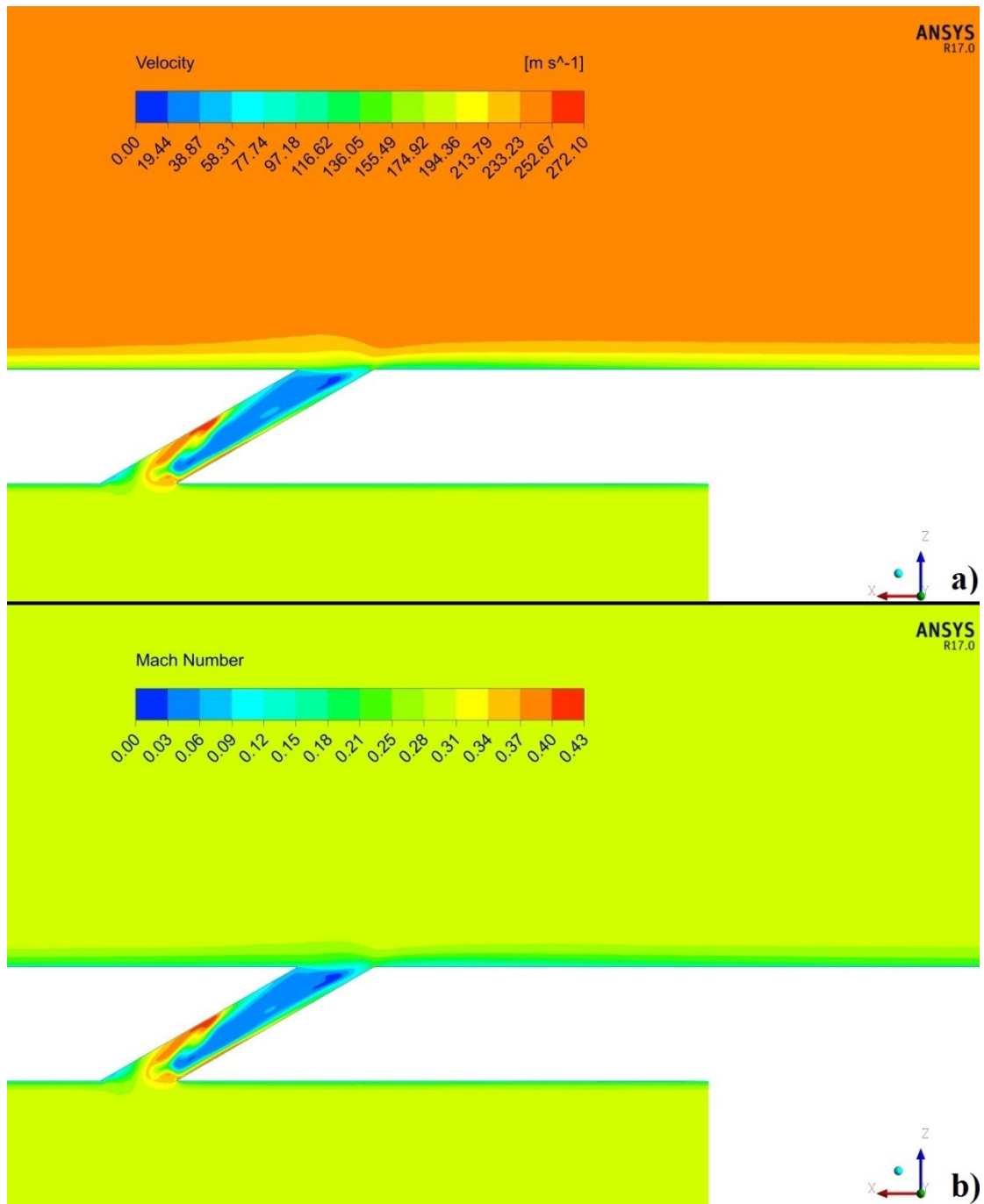
Fig. 4.12: *a) velocity and b) Mach number contours in the domain's symmetry plane (M=1).*

Test Case 3 (Blowing Ratio M=1.5)
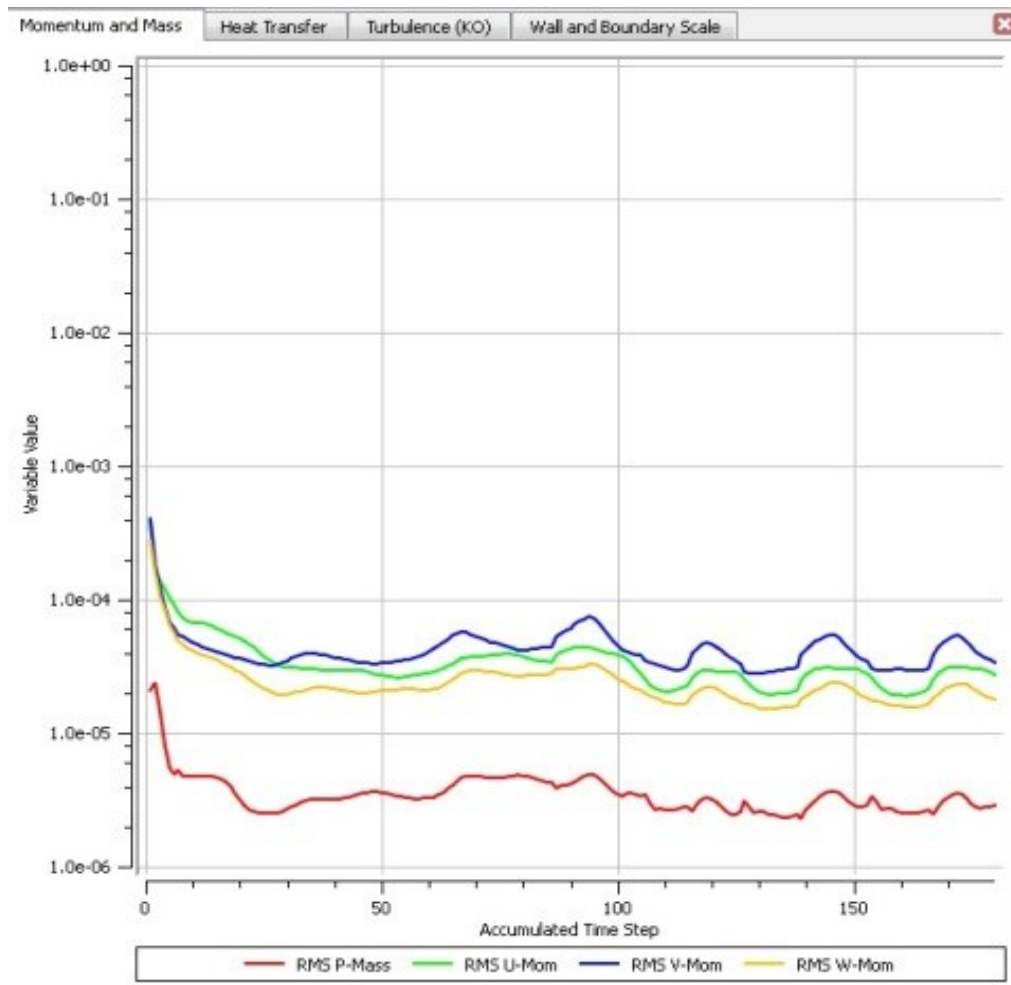
Fig. 4.13: *Test case residuals graph (M=1.5). The test case has not completely converged, due to unsteadiness.*
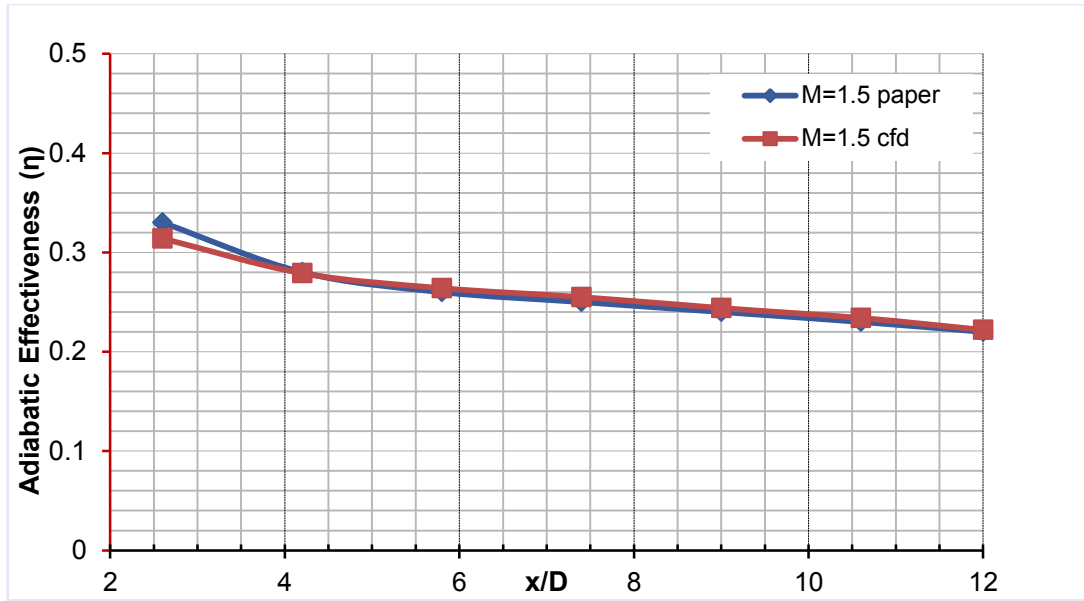
Fig. 4.14: *Adiabatic effectiveness – x/D graph (M=1.5).*
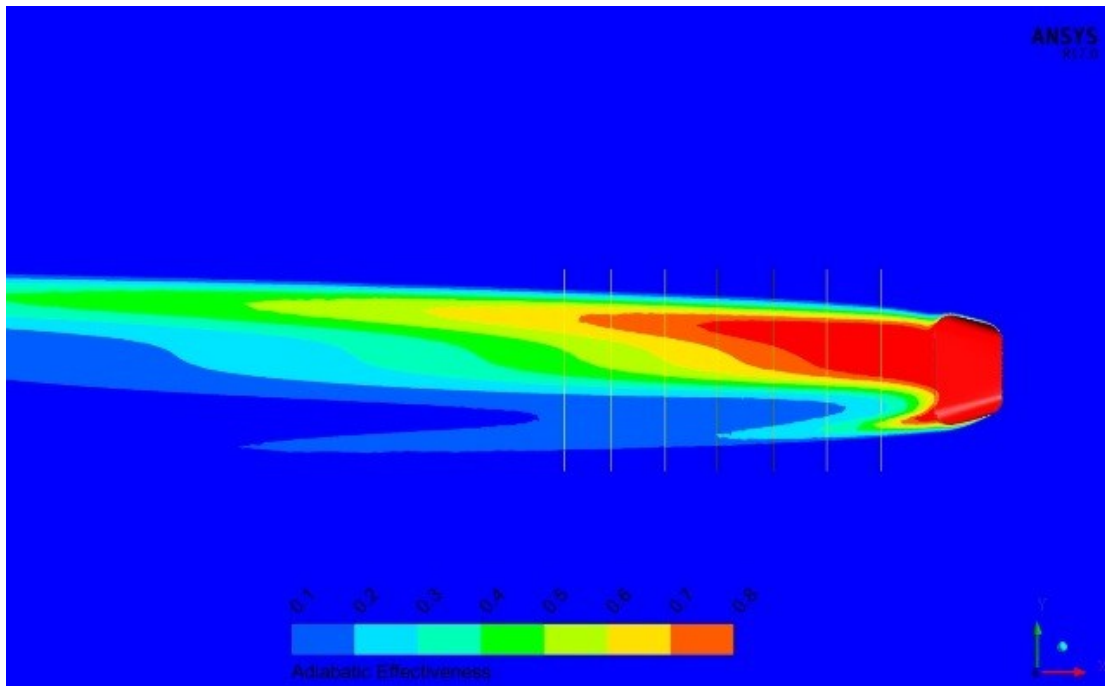
Fig. 4.15: *Adiabatic effectiveness contour in the mainflow wall surface (M=1.5).*
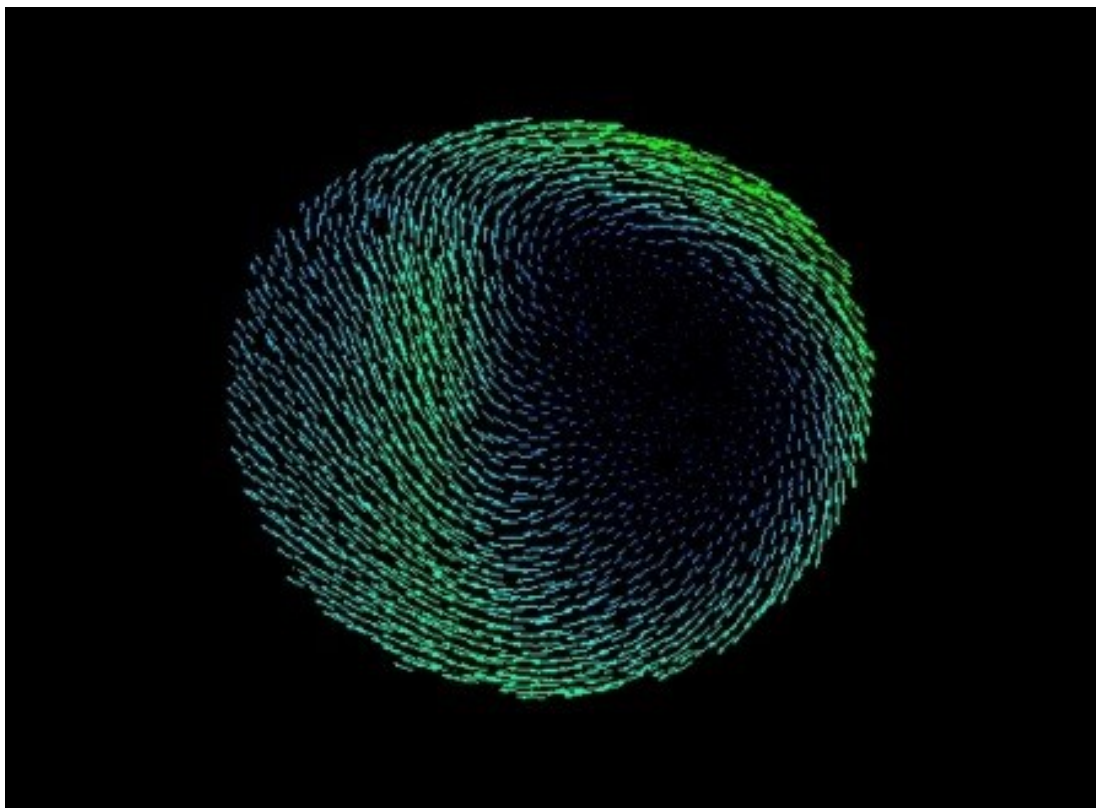
Fig. 4.16: *Calculated velocity field 2xD downstream of the cooling hole entrance (M=1.5).*
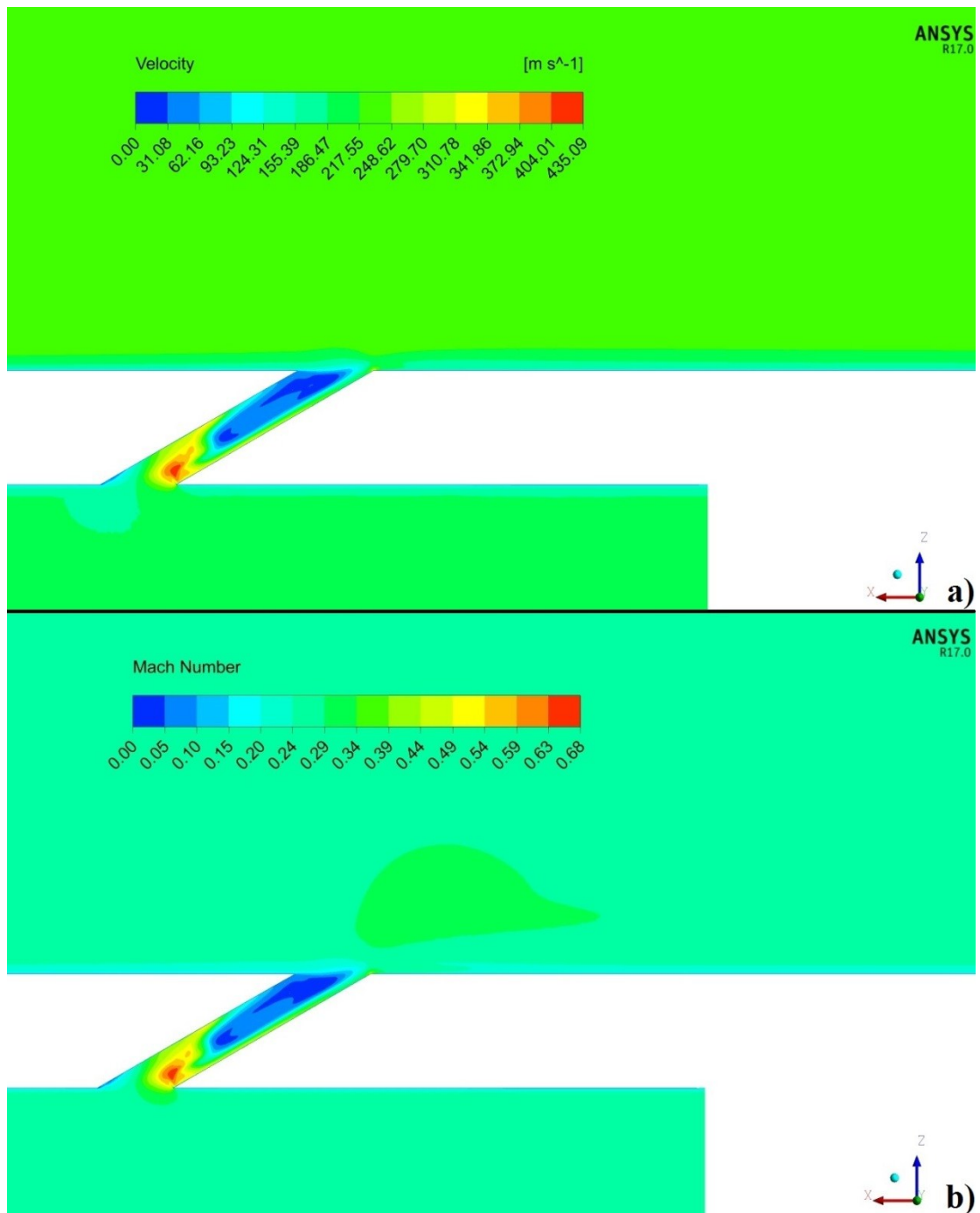
Fig. 4.17: *a) velocity and b) Mach number contours in the domain's symmetry plane (M=1.5).*
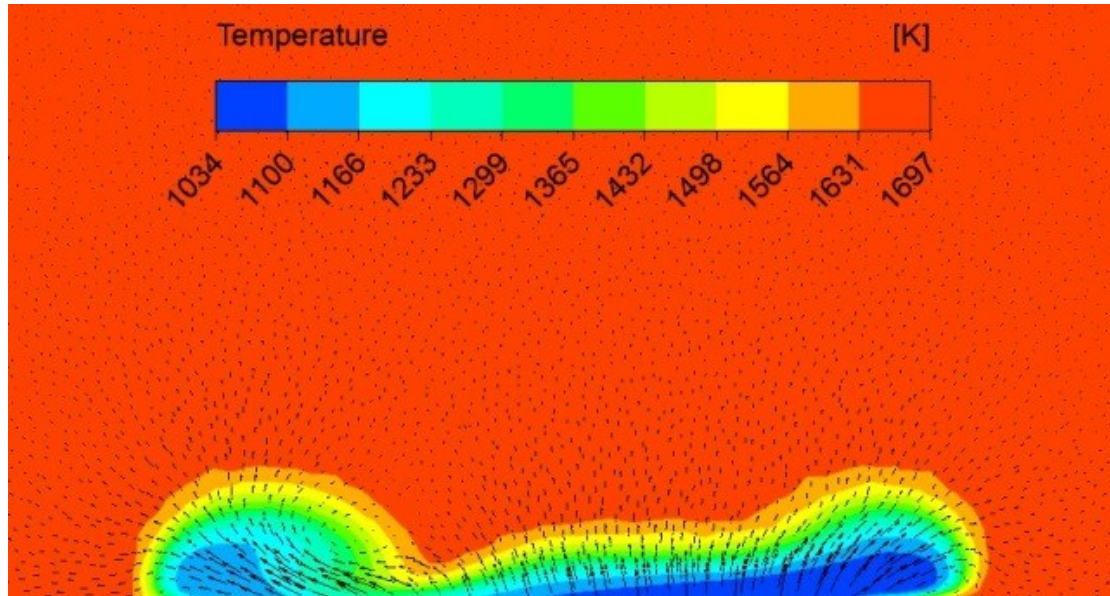
Fig. 4.18: *Temperature and calculated velocity field 2xD downstream of the cooling hole exit (M=1.5).*

Test case 4 (Blowing Ratio M=2.5)
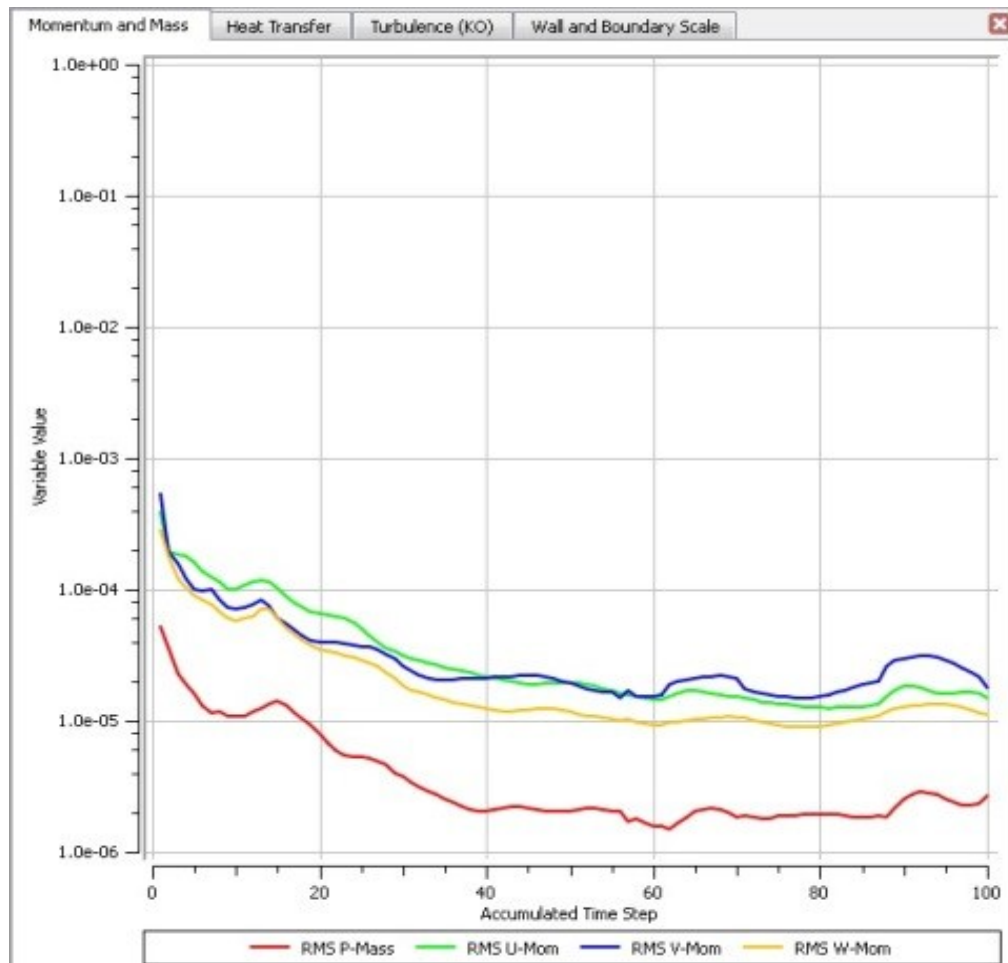
Fig. 4.19: *Test case residuals graph (M=2.5). The test case has not completely converged, due to unsteadiness.*
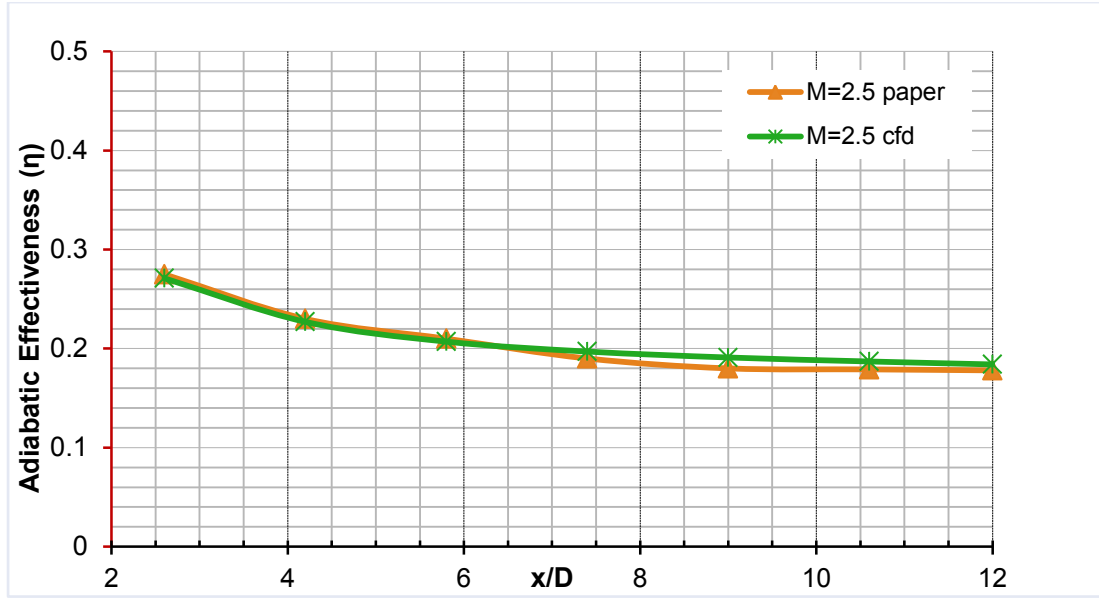
Fig. 4.20: *Adiabatic effectiveness – x/D graph (M=2.5).*
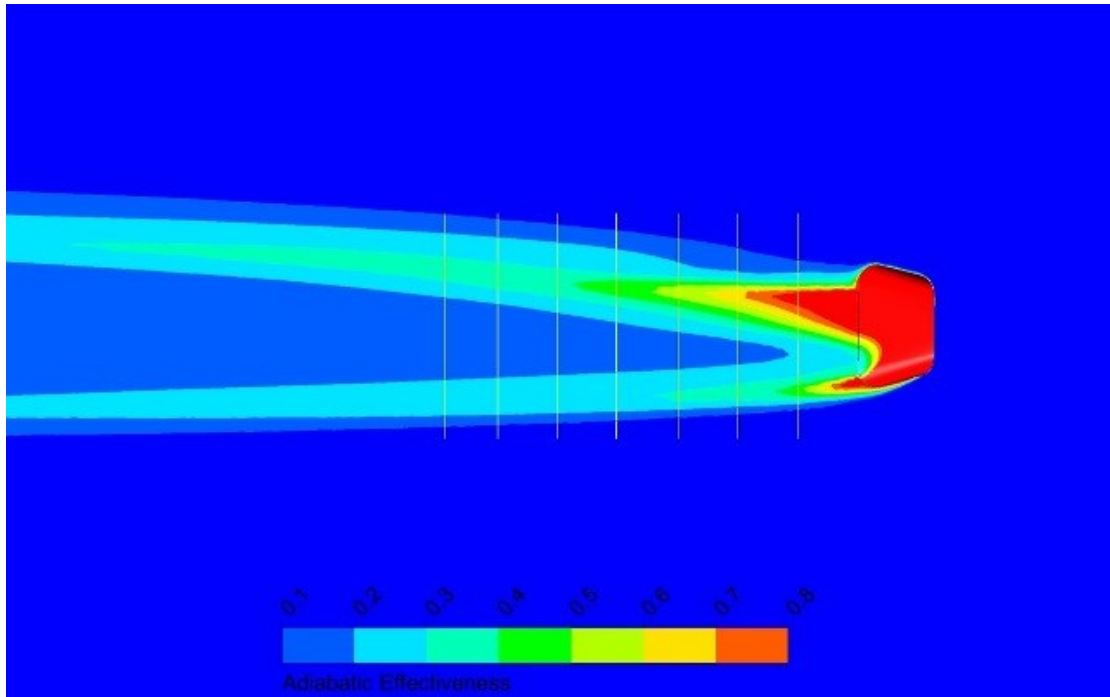
Fig. 4.21: *Adiabatic effectiveness contour in the mainflow wall surface (M=2.5).*
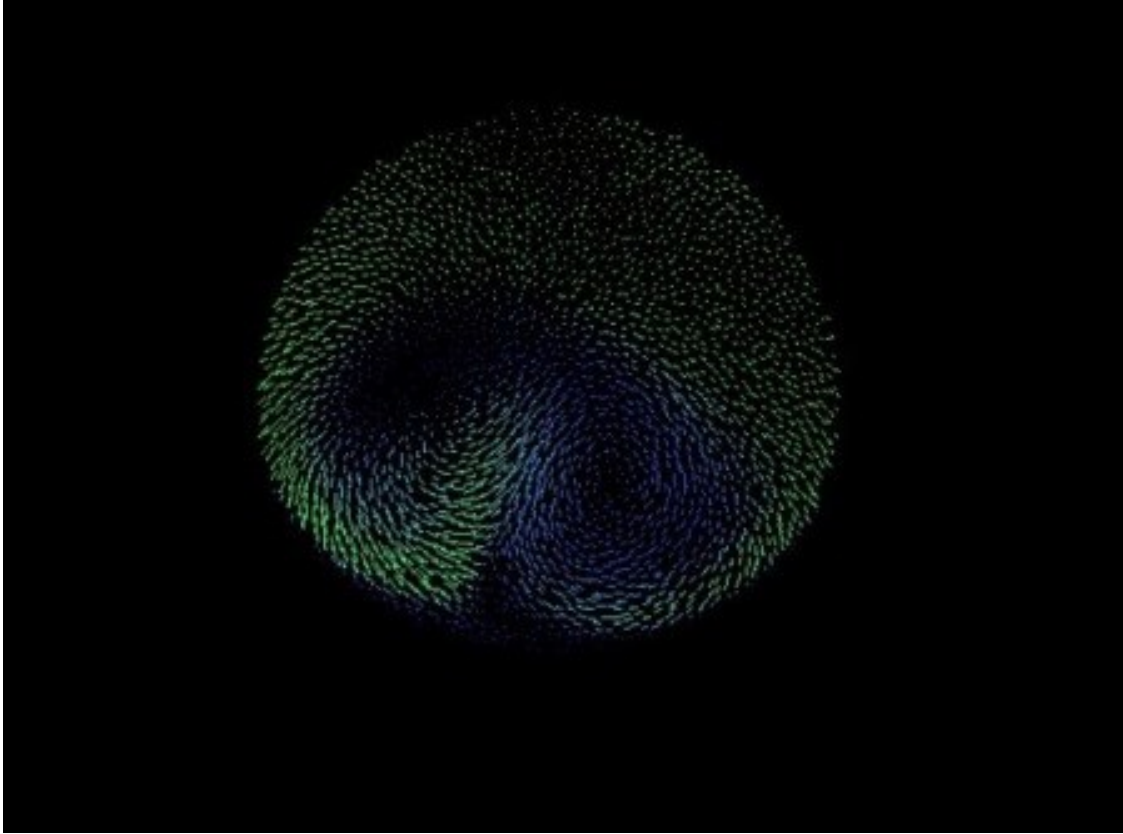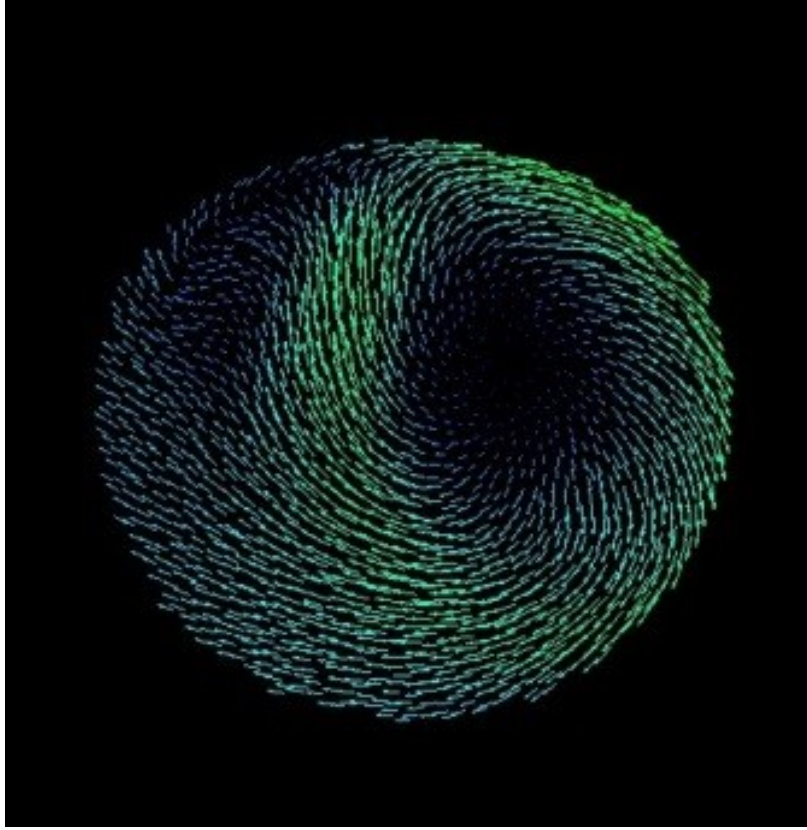
Fig. 4.22: *Calculated velocity field 2xD downstream of the cooling hole entrance (M=2.5).*
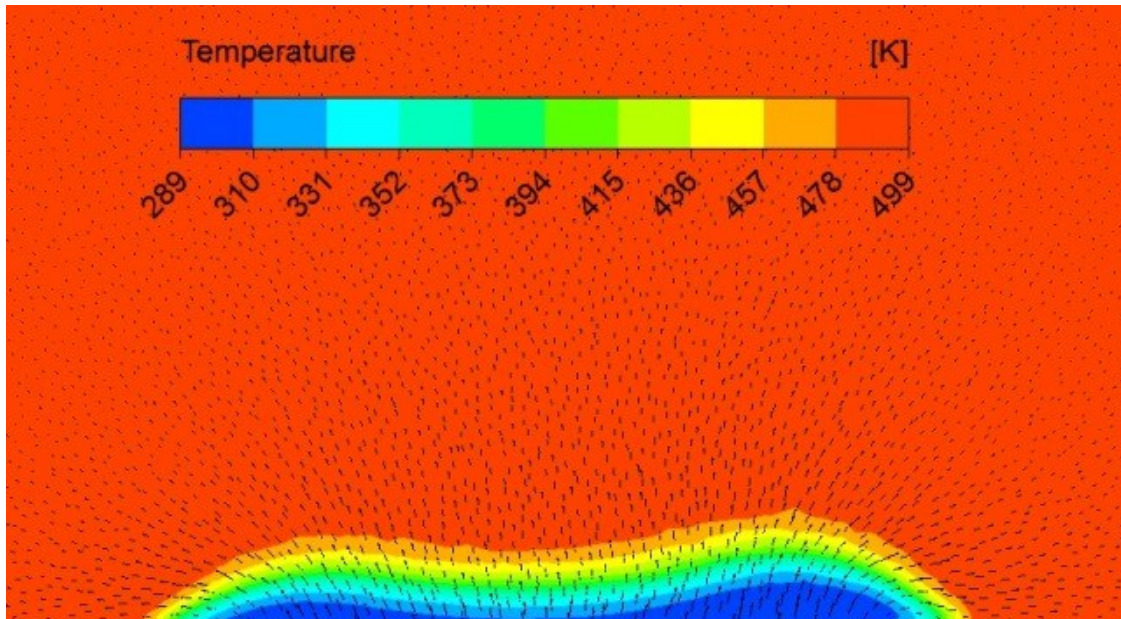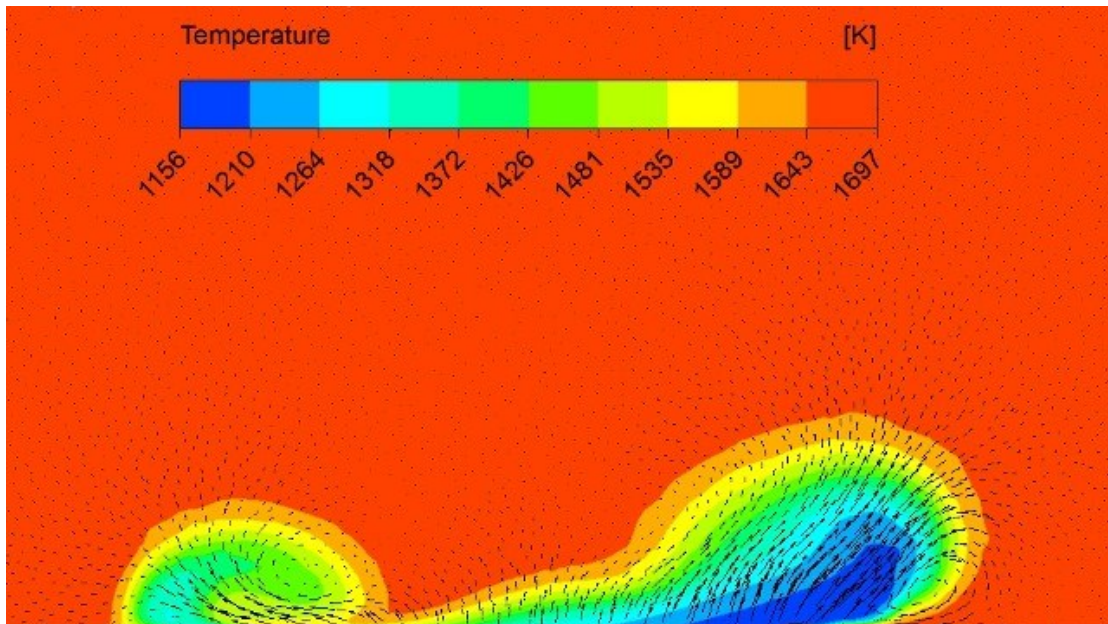

Fig. 4.23: *Temperature and calculated velocity field 2xD downstream of the cooling hole exit (M=1.5).*
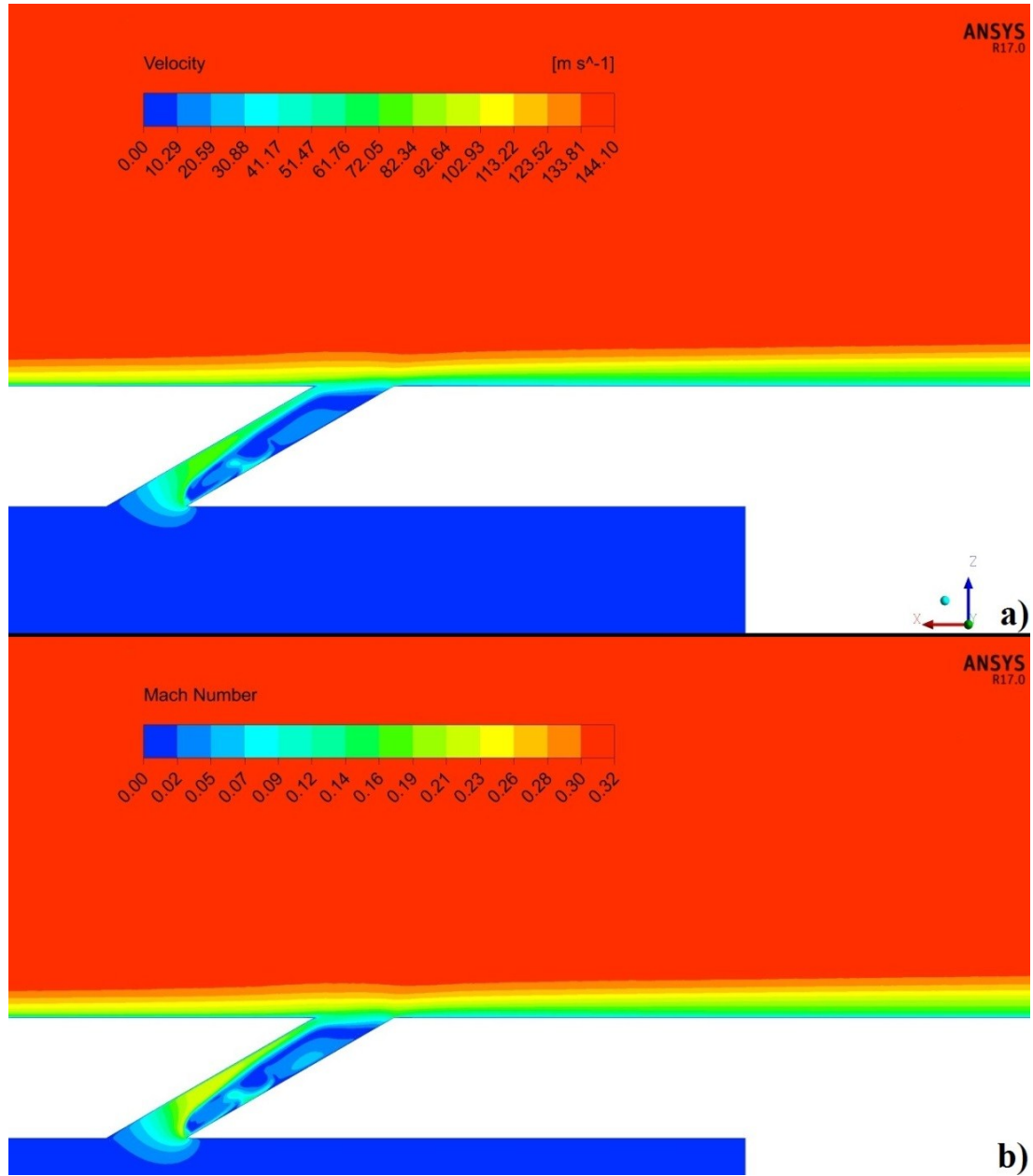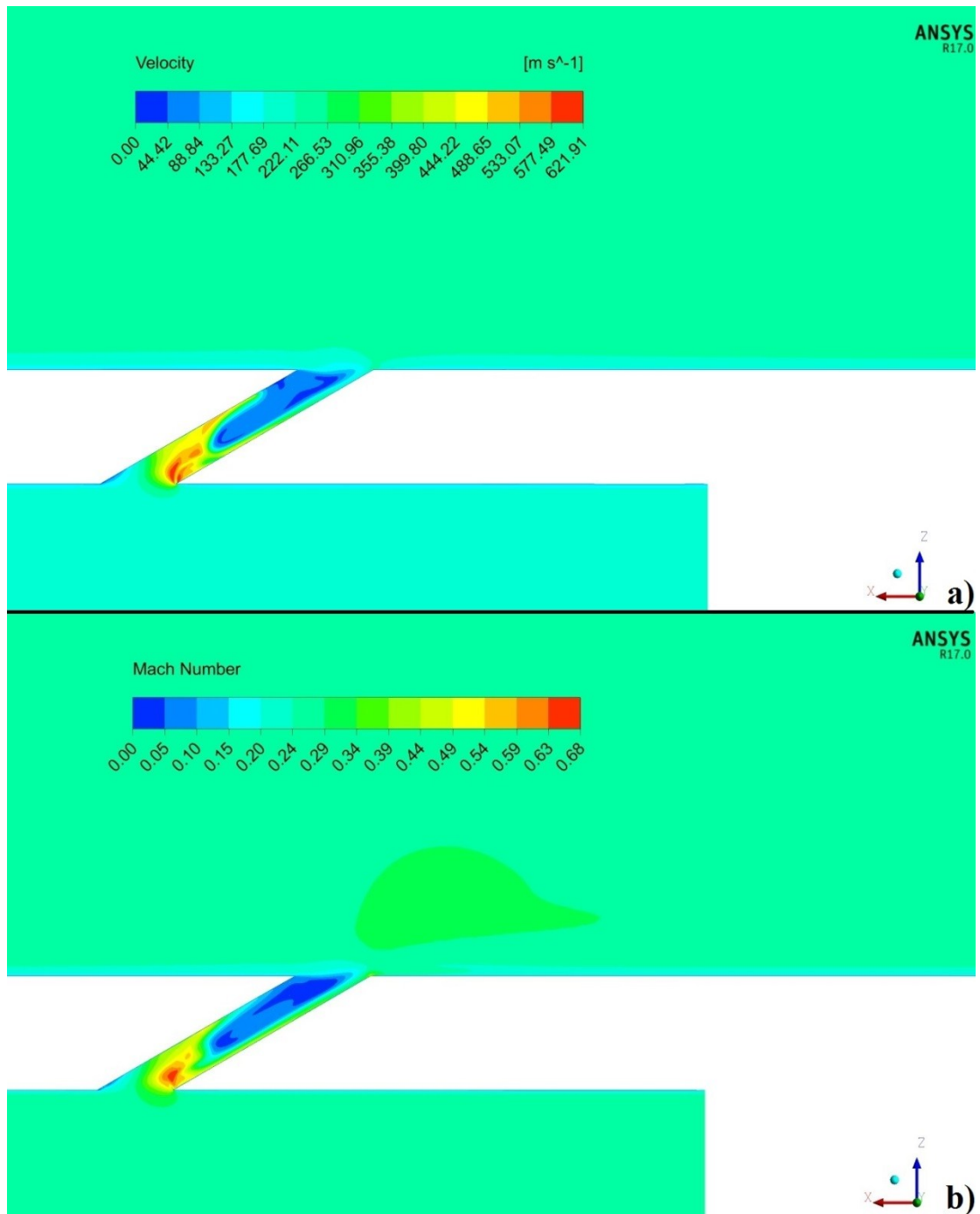
Fig. 4.24: *a) velocity and b) Mach number contours in the domain's symmetry plane (M=2.5).*

Chapter 5: Conclusions

In this work, firstly a review of the erosion effect was presented, an effect which is created in the jet engines' turbines. Secondly, a flow simulation study was conducted (using CFD) for a typical fan-shaped cooling hole geometry, for different air blowing ratios.

The literature study showed that the erosion effect is directly connected to the increase of Turbine Entry Temperature (which is constantly increasing through new available technologies, making engines more efficient). The study also showed that the particles ingested by the engine inlet, or fuel impurities, are able to decrease the cooling effectiveness of the turbine cooling system, making erosion formation easier to spread. Plugging of cooling holes and TBC degradation through surface roughness, are the main damage erosion causes on blades. Due to the fact that there still haven't been invented solutions that can completely diminish the problem, the best way of "dealing" with it, is preventing erosion formation. The most popular ways are internal washing (online and offline) of the engine in specific time schedules and the filtration of the environmental air before ingested.

Thereinafter, the flow in a cooling hole was studied, for 4 different blowing ratios (M=0.5, 1.0, 1.5, 2.5) and the correctness of the results was evaluated by comparing them to the experimental results of [Saumweber, et al., 2008]. The results came in good agreement (the difference was generally below 10%).

Last, it is recommended that in the future, a flow simulation using a mix of fluid and impurities particles should be conducted (for different cooling hole geometries and orientation angles), in order to form a complete view of the turbine blades cooling system efficiency degradation.

References

Ai, W., Murray, N., Fletcher, T. H., Harding, S., Lewis, S., Bons, J. P. (2012). "Deposition Near Film Cooling Holes on a High Pressure Turbine Vane", *ASME Journal of Turbomachinery*, Vol. 134(4), 041013-1.

Albert, J. E., Bogard, D. G. (2013). "Experimental Simulation of Contaminant Deposition on a Film-Cooled Turbine Vane Pressure Side With a Trench", *ASME Journal of Turbomachinery*, Vol. 135(5), 051008-1.

Albert, J. E., Bogard, D. G. (2012). "Experimental Simulation of Contaminant Deposition on a Film Cooled Turbine Airfoil Leading Edge", *ASME Journal of Turbomachinery*, Vol. 134(5), 051014-1.

Szczepankowski, A., Szymczak, J., Przysowa, R. (2017). *The Effect of a Dusty Environment Upon Performance and Operating Parameters of Aircraft Gas Turbine Engines*, NATO S&T Organization, STO-MP-AVT-272.

ANSYS Inc. (2013). *ANSYS CFD User's Guide*.

Basendwah, A., Pilidis, P., Li, Y. G. (2006). "Turbine off- line water wash optimization approach for power generation", *ASME Turbo Expo 2006: Power for Land, Sea and Air*, Barcelona, Spain, May 8-11.

Bogard, D. G., Schmidt, D. L., Tabbita, M. (1998). "Characterization and Laboratory Simulation of Turbine Airfoil Surface Roughness and Associated Heat Transfer", *ASME Journal of Turbomachinery*, Vol. 120, pp. 337-342.

Bons, J. P. (2010). "A Review of Surface Roughness Effects in Gas Turbines". *ASME Journal of Turbomachinery*, Vol. 132(2), 021004-1.

Cardwell, N. D., Thole, K. A., Burd, S. W. (2010). "Investigation of Sand Blocking Within Impingement and Film-Cooling Holes", *ASME Journal of Turbomachinery*, Vol. 132(2), 021020-1.

Casari, N., Pinelli, M., Suman, A., Montomoli, F., Luca di Mare (2017). "EBFOG: Deposition, erosion and detachment on high pressure turbine vanes", *Proceedings of ASME Turbo Expo 2017: Turbomachinery Technical Conference and Exposition*, Charlotte, NC, USA, June 26-30.

Crosby, J. L., Lewis, S., Bons, J. P., Ai, W., Fletcher, T. H. (2008). "Effects of Temperature and Particle Size on Deposition in Land Based Turbines", *ASME Journal of Engineering for Gas Turbines and Power*, Vol. 130(5), 051503-1.

Ghenaiet, A. (2014). "Study of particle ingestion through two-stage gas turbine", *Proceedings of ASME Turbo Expo 2014: Turbine Technical Conference and Exposition*, Düsseldorf, Germany, June 16-20.

Goulding, C. H., Rasmussen M. G., Fritz, F. M. Jr. (1990). "Technical and Other Considerations for the Selection of Inlet Air Filtration Systems for High-Efficiency Industrial Combustion Turbines", *ASME Gas Turbine and Aeroengine Congress and Exposition*, Brussels, Belgium, June 11-14.

Hamed, A. A., Tabakoff, W., Rivir, R. B., Das, K., Arora, P. (2004). "Turbine Blade Surface Deterioration By Erosion", *Proceedings of ASME Turbo Expo 2004 Power for Land, Sea, and Air*, Vienna, Austria, June 14-17.

Han, J.-C. (2013). "Fundamental Gas Turbine Heat Transfer", *ASME Journal of Thermal Science and Engineering Applications*, Vol.5(2), 021007-1.

Haub, G. L., Hauhe, W. E. Jr. (1990). "Field Evaluation of On-Line Compressor Cleaning in Heavy Duty Industrial Gas Turbines", *ASME Gas Turbine and Aeroengine Congress and Exposition*, Brussels, Belgium, June 11-14.

Kistenmacher, D. A., Davidson, F. T., Bogard, D. G. (2014). "Realistic Trench Film Cooling With a Thermal Barrier Coating and Deposition", *ASME Journal of Turbomachinery,* Vol. 136(9), 091002-1.

Lau, S. C., Cervantes J., Han, J. C., Rudolph, R. J. (2008). "Internal Cooling Near Trailing Edge of a Gas Turbine Airfoil With Cooling Airflow Through Blockages With Holes", *ASME Journal of Turbomachinery*, Vol. 130(3), 031004-1.

Lawson, S. A., Thole, K. A. (2011). "Effects of Simulated Particle Deposition on Film Cooling", *ASME Journal of Turbomachinery*, Vol. 133(2), 021009-1.

Lawson, S. A., Thole, K. A. (2012). "Simulations of Multiphase Particle Deposition on Endwall Film-Cooling", *ASME Journal of Turbomachinery*, Vol. 134(1), 011003-1.a

Lawson, S. A., Thole, K. A. (2012). "Simulations of Multiphase Particle Deposition on Endwall Film-Cooling Holes in Transverse Trenches", *ASME Journal of Turbomachinery*, Vol. 134(5), 051040-1.b

Lawson, S. A., Thole, K. A., Nakamata, C. (2012). "Simulations of Multiphase Particle Deposition on a Showerhead With Staggered Film-Cooling Holes", *ASME Journal of Turbomachinery*, Vol. 134(5), 051041-1.c

Madsen, S., Bakken, L. E. (2014). "Gas Turbine Operation Offshore; On-Line Compressor Wash Operational Experience", *Proceedings of ASME Turbo Expo 2014: Turbine Technical Conference and Exposition*, Düsseldorf, Germany, June 16-20.

Maikell, J., Bogard, D., Piggush, J., Kohli, A. (2011). "Experimental Simulation of a Film Cooled Turbine Blade Leading Edge Including Thermal Barrier Coating Effects", *ASME Journal of Turbomachinery*, Vol. 133(1), 011014-1.

Murata, A., Nishida, S., Saito, H., Iwamoto, K., Okita, Y., Nakamata, C. (2012). "Effects of Surface Geometry on Film Cooling Performance at Airfoil Trailing Edge", *ASME Journal of Turbomachinery*, Vol. 134(5), 051033-1.

Murugan, M., Ghoshal, A., Walock, M., Nieto, A., Bravo, L., Barnett, B., Pepi, M., Swab, J., Pegg, R. T., Rowe, C., Zhu, D., Kerner, K. (2017). "Microstructure based material-sand particulate interactions and assessment of coatings for high temperature turbine blades", *Proceedings of ASME Turbo Expo 2017: Turbomachinery Technical Conference and Exposition*, Charlotte, NC, USA, June 26-30.

Nikuradse, J. (1950). *Laws of flow in rough pipes*, Washington: NACA TM 1292.

Ogiriki,E. A., Li, Y. G., Nikolaidis, T., Isaiah, T. E., Sule, G. (2015). "Effect of fouling, thermal barrier coating degradation and film cooling holes blockage on gas turbine engine creep life", *Procedia CIRP 38*, Vol. 38, pp. 228 – 233.

Pulimood, M. K. (1981). "Field Experience With Gas Turbine Inlet Air Filtration", *ASME Gas Turbine Conference & Products Show*, Houston, USA, March 9-12.

Roupa, A., Pilidis, P., Allison, I, Lambart, P. (2013). "Study Of Wash Fluid Cleaning Effectiveness On Industrial Gas Turbine Compressor Foulants", *Proceedings of the ASME Turbo Expo 2013: Turbine Technical Conference and Exposition GT2013*, San Antonio, Texas, USA, June 3-7.

Rutledge, J. L., Robertson, D., Bogard, D. G. (2006). "Degradation of Film Cooling Performance on a Turbine Vane Suction Side due to Surface Roughness", *ASME Journal of Turbomachinery*, Vol. 128(3), pp. 547-554.

Schroth, T., Cagna, M. (2008). "Economical Benefits Of Highly Efficient Three-Stage Intake Air Filtration For Gas Turbines", *Proceedings of ASME Turbo Expo 2008: Power for Land, Sea and Air*, Berlin, Germany, June 9-13.

Shi, X., Long, F., Yan, Z., Tang, J. (2016). "A Review of Aero-engine Blade Fouling Mechanism", *2016 IEEE/CSAA International Conference on Aircraft Utility Systems (AUS)*, Beijing,China, October 10-12.

Sigal, A., Danberg, J. E. (1990). "New Correlation of Roughness Density Effect on the Turbulent Boundary Layer", *AIAA Journal*, Vol. 28(3), pp. 554-556.

Somawardhana, R. P., Bogard, D. G. (2009). "Effects of Obstructions and Surface Roughness on Film Cooling Effectiveness With and Without a Transverse Trench", *ASME Journal of Turbomachinery*, Vol. 131(1), 011010-1-8.

Stalder, J. P. (2001). "Gas Turbine Compressor Washing State of the Art: Field Experiences", *ASME Journal of Engineering for Gas Turbines and Power*, Vol. 123(2), pp. 363- 370.

Stripf, M., Schulz, A., Wittig, S. (2005). "Surface Roughness Effects on External Heat Transfer of a HP Turbine Vane", *ASME Journal of Turbomachinery*, Vol. 127(1), pp. 200-208.

Sundaram, N., Barringer, M. D., Thole, K. A. (2008). "Effects of Deposits on Film Cooling of a Vane Endwall Along the Pressure Side", *ASME Journal of Turbomachinery*, Vol. 130(4), 041006-1.

Sundaram, N., Thole, K. A. (2007). "Effects of Surface Deposition, Hole Blockage, and Thermal Barrier Coating Spallation on Vane Endwall Film Cooling", *ASME Journal of Turbomachinery*, Vol. 129(3), pp. 599-607.

Syverud, E., Bakken, L. E. (2007). "Online Water Wash Tests of GE J85-13", *ASME Journal of Turbomachinery*, Vol. 129(1), pp. 136-142.

Tabakoff, W. (1988). "Turbomachinery Alloys Affected by Solid Particles", *ASME Gas Turbine and Aeroengine Congress*, Amsterdam, The Netherlands, June 6-9.

Webb, J., Casaday, B., Barker, B., Bons, J. P., Gledhill, A. D., Padture, N. P. (2013). "Coal Ash Deposition on Nozzle Guide Vanes Part I: Experimental Characteristics of Four Coal Ash Types", *ASME Journal of Turbomachinery*, Vol. 135(2), 021033-1.

Wilcox, M., Baldwin, R., Garcia-Hernandez, A., Brun, K. (2010). *Guideline For Gas Turbine Inlet Air Filtration Systems*, Gas Machinery Research Council Southwest Research Institute.

Yun, Y. I., Park, I. Y., Song, S. J. (2005). "Performance Degradation due to Blade Surface Roughness in a Single-Stage Axial Turbine", *ASME Journal of Turbomachinery*, Vol. 127(1), pp. 137-143.

Wylie, S., Bucknell, A., Forsyth, P., McGilvray, M., Gillespie, D. R. H. (2016). "Reduction in Flow Parameter Resulting From Volcanic Ash Deposition in Engine Representative Cooling Passages," *ASME Paper No. GT2016- 57296*.

Yang, H., Xu, H. (2014). "Numerical Simulation Of Gas-Solid Two Phase Flow In Fouled Axial Flow Compressor", *ASME Turbo Expo 2014: Turbine Technical Conference and Exposition*, 2014:V02BT39A027.

Kurz, R., Brun, K. (2000). "Degradation in gas turbine systems", *Proceeding of ASME TURBOEXPO 2000*, May 8-11, Munich Germany.

Suman, A., Morini, M., Ald,i N., Casari, N., Pinelli, M., Spina, P. R., (2017). "A Compressor Fouling Review Based on an Historical Survey of ASME Turbo Expo Papers", *ASME Journal of Turbomachinery*, Vol. 139(4), 041005.

Narayan, K. L. (2008). *Computer Aided Design and Manufacturing*, New Delhi: Prentice Hall of India.

Duggal, V. (2000). *Cadd Primer: A General Guide to Computer Aided Design and Drafting-Cadd, CAD*, Mailmax Pub.

Madsen, D. A. (2012). *Engineering Drawing & Design*, Clifton Park, NY: Delmar.

Farin, G., Hoschek, J., Kim, M.-S. (2002). *Handbook of computer aided geometric design*, Elsevier.

Pottmann, H., Brell-Cokcan, S., Wallner, J. (2007). "Discrete surfaces for architectural design", in P. Chenin, T. Lyche, L.L. Schumaker (Eds.), *Curves and Surface Design: Avignon 2006*, Nashboro Press, pp. 213–234. ISBN: 978-0-9728482-7-5.

Saumweber, C., Schulz, A. (2008). "Comparison the Cooling Performance of Cylindrical and Fan-Shaped Cooling Holes With Special Emphasis on the Effect of Internal Coolant Cross-Flow", *ASME Turbo Expo 2008: Power for Land, Sea, and Air*, Berlin, Germany, June 9–13.

Han, J. C., Dutta, S., and Ekkad, S. V., (2013). *Gas Turbine Heat Transfer and Cooling Technology,* 2nd ed., Taylor & Francis, Inc., New York.

Lee, A. S., Singh, R., Probert, S. D., (2009). "Modelling of the Performance of a F100-PW229 Equivalent Engine under Sea-level Static Conditions", *45th AIAA/ASME/SAE/ASEE Joint Propulsion Conference & Exhibit,* 2 - 5, Denver, Colorado.

Appendix A: Boundary Conditions

Test case 1 (Numerical method validation)

In Table A.1, it is shown that the boundary conditions are changed in such a way as to achieve the desired blowing ratios. The only variable that is constant is $\frac{\rho_c}{\rho_m} = 1.75$. Due to the fact that the fluid in the simulation was chosen to be an ideal gas, the equation of state can be used:

$$\frac{P_{sm}}{P_{sc}} = \frac{\frac{\rho_m * R * T_{sm}}{M_\Gamma}}{\frac{\rho_c * R * T_{sc}}{M_\Gamma}} \Rightarrow \frac{P_{sm}}{P_{sc}} = \frac{\rho_m}{\rho_c} * \frac{T_{sm}}{T_{sc}} \Rightarrow \frac{P_{sc}}{P_{sm}} * \frac{T_{sm}}{T_{sc}} = 1.75 \qquad (A.1)$$

From equations (A.1), (A.2) and (A.3), by adjusting $\frac{T_{sc}}{T_{sm}}$ and $\frac{P_{sc}}{P_{sm}}$, the desired blowing ratio can be obtained. Also, it is given from [Saumweber, et al., 2008] that $T_{tc} = 290 \text{ K}$ and, additionally, it was assumed that the cooling flow Total Pressure was $P_{tc} = 1 \; bar$ (a reasonable value for the temperature above) and the mainflow Mach number $Ma_m = 0.3$, [Saumweber, et al., 2008]. Last, cooling flow Mach number was set to $Ma_c = 0$, therefore cooling flow Static Pressure was set equal to cooling flow Total Pressure $P_{sc} = P_{tc}$. The mainflow Total Pressure and Total Temperature, can be calculated using the isentropic process equations for Mach number $Ma_m = 0.3, \gamma = 1.333, \frac{\gamma}{\gamma-1} = 4,$:

$$\frac{P_{tm}}{P_{sm}} = (1 + \frac{\gamma - 1}{2} * Ma_m{}^2)^{\frac{\gamma}{\gamma-1}} \Rightarrow \frac{P_{tm}}{P_{sm}} = 1.015^4 \Rightarrow P_{sm} = \frac{P_{tm}}{1.015^4} \qquad (A.2)$$

$$\frac{T_{tm}}{T_{sm}} = (1 + \frac{\gamma - 1}{2} * Ma_m{}^2) \Rightarrow \frac{T_{tm}}{T_{sm}} = 1.015 \Rightarrow T_{sm} = \frac{T_{tm}}{1.015} \qquad (A.3)$$

By adjusting the variables based on the above equations, the final boundary conditions were calculated (Table A.1).

Test cases 2, 3 and 4 (Operational conditions)

The following test cases were set using the same method, as in Test Case 1. The data used came from [Lee, et al., 2009], along with some calculations.
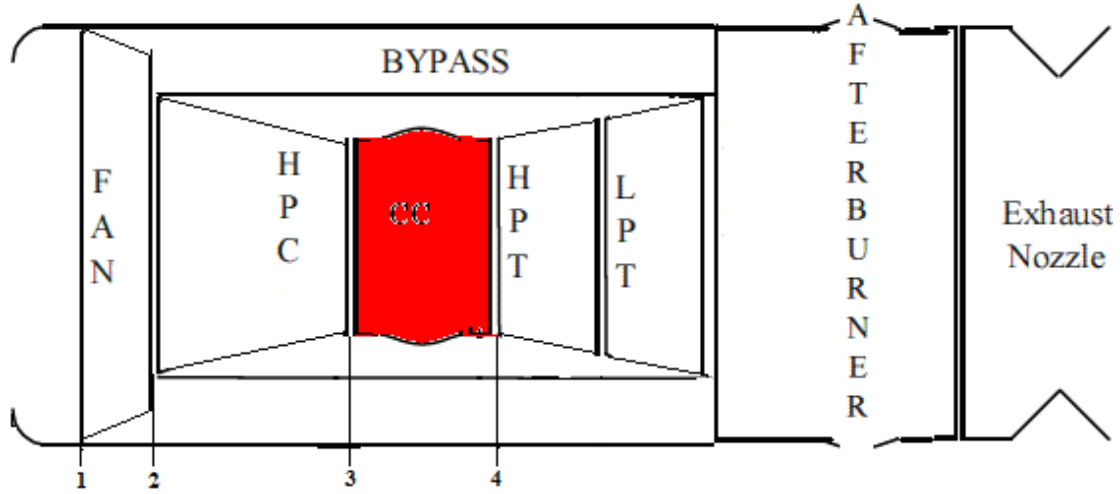
Fig A.1*: Simplified Schematic diagram of F100-EQ engine's layout [Lee, et al., 2009].*

Data from Lee [Lee, et al., 2009]:

OPR = 32.4

FPR = 3.55

η_{fan} *= 0.83*

η_{hpc} *= 0.895*

Π_{mb} *= 0.96*

T_4 *= 1700 K*

FAN

$$\frac{P_2}{P_1} = 3.55 \implies \boldsymbol{P_2 = 359,703.75\ Pa}$$

Based on isentropic process equations, T_2 is calculated:

$$T_2 - T_1 = \frac{T_1}{\eta_{fan}} * \left[\left(\frac{P_2}{P_1}\right)^{\frac{\gamma-1}{\gamma}} - 1 \right] \implies \boldsymbol{T_2 = 417.5194\ K}$$

HPC

$$\frac{OPR}{FPR} = \frac{32.4}{3.55} = \boldsymbol{9.1268}$$

$$\frac{P_3}{P_2} = 9.1268 \implies \boldsymbol{P_3 = 3,282,944.186\ Pa}$$

$$T_3 - T_2 = \frac{T_2}{\eta_{hpc}} * \left[\left(\frac{P_3}{P_2} \right)^{\frac{\gamma-1}{\gamma}} - 1 \right] \implies \boldsymbol{T_3 = 761.8537\ K}$$

HPT

Π_{mb} equals to 0.96 , therefore:

$$P_4 = P_3 * \Pi_{mb} = 3,282,944.186 * 0.96 \implies \boldsymbol{P_4 \simeq 3,150,000\ Pa}$$

Hence, the Mainflow Total Pressure was set to **3,150,000 Pa** and the mainflow Total Temperature to **1700 K**.

Based on the research conducted by [Han, et al., 2013], it is known that the range of Pressure ratio $\frac{P_{sc}}{P_{sm}}$ values varies from 1.02 to 1.10, Temperature ratio $\frac{T_{sc}}{T_{sm}}$ varies from 0.5 to 0.85 and Density ratio $\frac{\rho_c}{\rho_m}$ from 1.5 to 2.0. A constant DR value of 1.75 was selected (the same values as in [Saumweber, et al., 2008]), so that the results can be compared to the [Saumweber, et al., 2008] test cases.

Cooling flow Static Pressure ($Ma_c = 0.29$) was calculated as follows:

$$\frac{P_{tc}}{P_{sc}} = (1 + \frac{\gamma - 1}{2} * Ma_c{}^2)^{\frac{\gamma}{\gamma-1}} \Rightarrow \frac{P_{tc}}{P_{sc}} = 1.014^4 \Rightarrow \boldsymbol{P_{sc}} = \frac{\boldsymbol{P_{tc}}}{\boldsymbol{1.014^4}} \qquad (A.4)$$

Table A.1: *Boundary conditions.*

Test Cases	1	2	3	4
P_{tm} *(Pa)*	1 bar	3,150,000	3,150,000	3,150,000
P_{sm} *(Pa)*	0.94 bar	2,967,880	2,967,880	2,967,880
P_{tc} *(Pa)*	0.96 bar	3,339,000	3,559,500	4,189,500
P_{sc} *(Pa)*	0.96 bar	3,158,382	3,366,954	3,962,875
P_{sc}/P_{sm}	1.02	1.06	1.13	1.34
T_{tm} *(K)*	500	1700	1700	1700
T_{sm} *(K)*	492	1675	1675	1675
T_{tc} *(K)*	290	1037	1105	1292
T_{sc} *(K)*	290	1023	1090	1274
T_{sm}/T_{sc}	1.70	1.64	1.54	1.31
DR_{target}	**1.75**	**1.75**	**1.75**	**1.75**
DR_{actual}	**1.73**	**1.74**	**1.74**	**1.76**
Ma_m	0.3	0.3	0.3	0.3
Ma_c	0	0.29	0.29	0.29
M (Results)	0.5	1.0	1.5	2.5

Table A.2: *Adiabatic effectiveness measurements.*

x/D	2.6	4.2	5.8	7.4	9	10.6	12
M = 0.5 **Paper**	0.3	0.24	0.19	0.16	0.15	0.14	0.13
M = 0.5 **CFD**	0.336	0.265	0.216	0.179	0.15	0.128	0.113
M = 1.0 **Paper**	0.34	0.28	0.25	0.22	0.21	0.19	0.18
M = 1.0 **CFD**	0.316	0.262	0.238	0.222	0.212	0.202	0.196
M = 1.5 **Paper**	0.33	0.28	0.26	0.25	0.24	0.23	0.22
M = 1.5 **CFD**	0.314	0.279	0.264	0.255	0.244	0.234	0.222
M = 2.5 **Paper**	0.275	0.23	0.21	0.19	0.18	0.179	0.178
M = 2.5 **CFD**	0.271	0.227	0.207	0.197	0.191	0.187	0.184

Table A.3: *Adiabatic effectiveness percentage difference between paper and CFD results.*

x/D	2.6	4.2	5.8	7.4	9	10.6	12	Average (%)
M = 0.5	0.12	0,104	0,137	0,119	0	0,086	0,131	9.946
M = 1.0	0.071	0,064	0,048	0,009	0,01	0,063	0,089	5.051
M = 1.5	0.048	0,004	0,015	0,02	0,017	0,017	0,009	1.866
M = 2.5	0.015	0,013	0,014	0,037	0,061	0,045	0,034	3.118

Appendix B: Test cases calculations

The following procedures were used to calculate the blowing ratio:

• A plane was created at the cooling hole exit with the name *Uc* (Fig. B.1).

• A new plane named Um surface was created, with a $49xD$ distance from the cooling hole outlet surface (Fig. B.2).

• Mainflow and cooling flow fluid densities were calculated using the function calculator, so as to ascertain if their quotient had the desired value ($DR = 1.75$).

• *Uc* was calculated, using massflowAve function (massflowAve was used because there was a mixture of 2 fluids of different densities at the point) (Fig. B.3).

• *Um* was calculated from the Um surface.

• *M* was calculated, based on equation:

$$M = \frac{\rho_c * U_c}{\rho_m * U_m} \qquad (B.1)$$

For the calculation of adiabatic effectiveness:

• A *Taw* variable was created (Fig. B.4).

• The *Trec* mainflow variable was created, with the value of the gas flow temperature in the mainflow before mixing with the cooling flow.

• *Ttc*, the Total Temperature value defined by the boundary conditions was considered, since after measurements, it was found that it remained constant throughout the cooling flow domain.

• The Adiabatic Effectiveness variable was created, according to equation (2) (Fig. B.4).
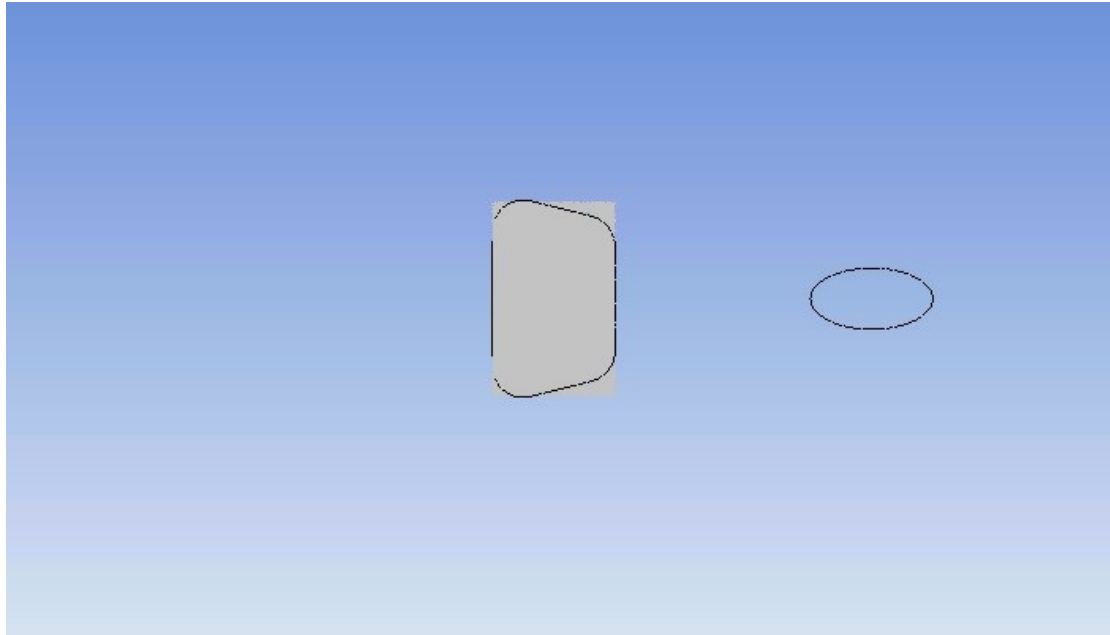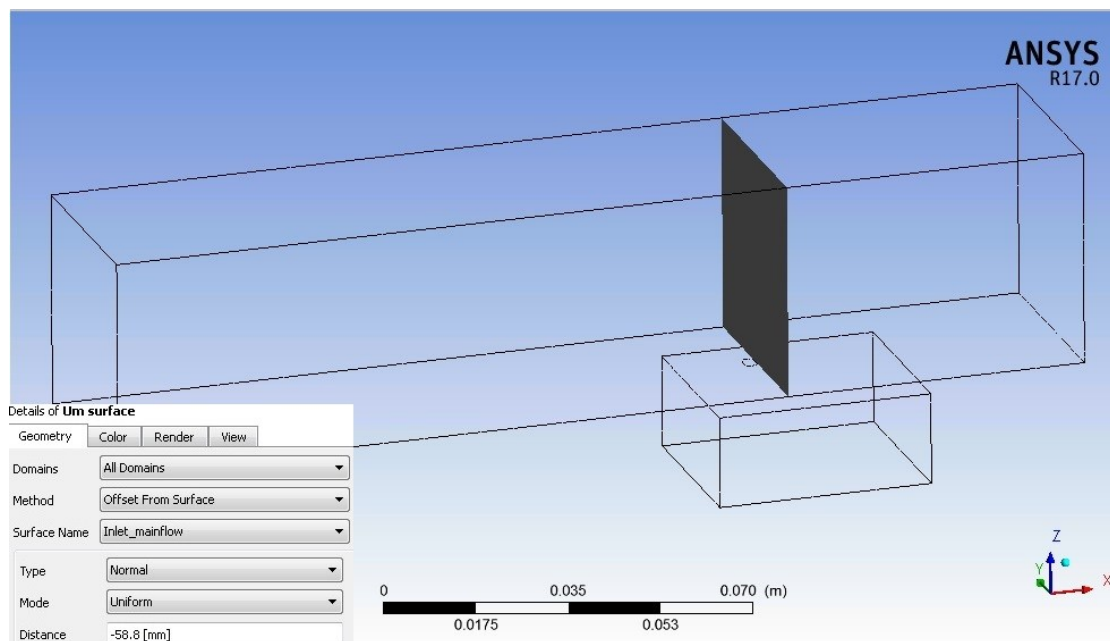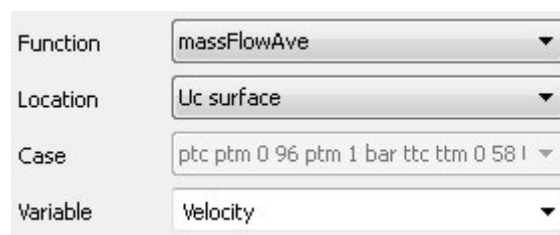
Fig. B.1: *Uc surface.*

Fig. B.2: *Um surface.*

Fig. B.3: *Uc calculation details.*

Fig. B.4: *Calculation details.*

In order create the adiabatic effectiveness versus x/D chart, seven lines were created, with specific spacing from the cooling hole exit, as in [Sauweber, et al. 2008]. The first line was created by measuring the distance from the cooling hole exit, not the point zero (Fig. B.5). The remaining distances were calculated with reference point line 1 (Table B.1).
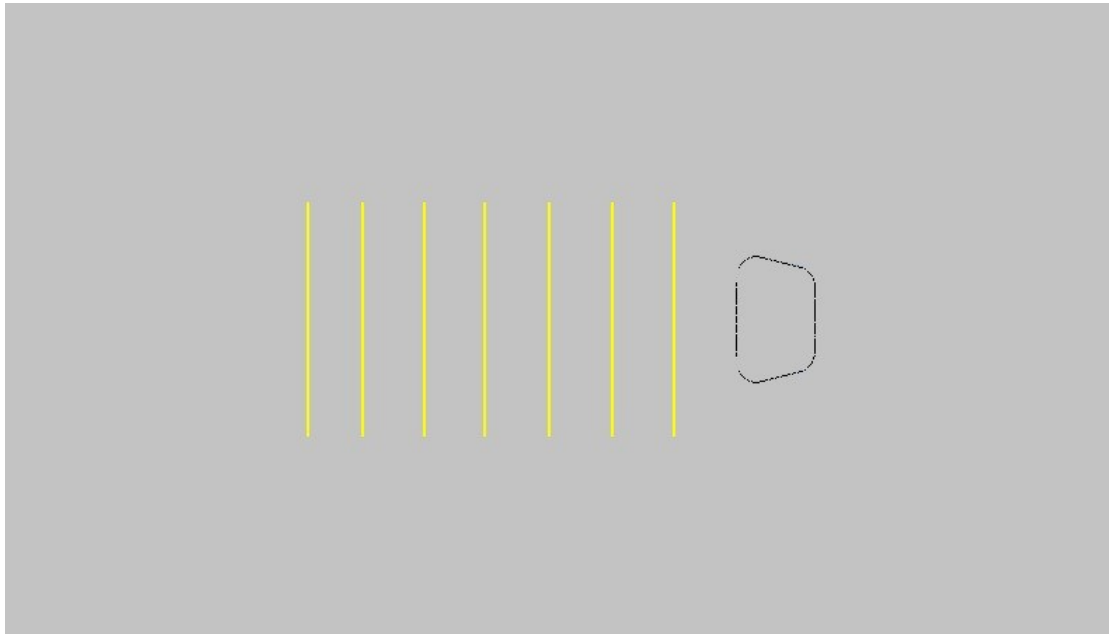

Fig. B.5: *Adiabatic effectiveness measurement lines.*

Table B.1*: Adiabatic effectiveness measurement lines definition.*

Line	x/D	y/D
1	1.6	[-3,3]
2	3.2	[-3,3]
3	4.8	[-3,3]
4	6.4	[-3,3]
5	8	[-3,3]
6	9.6	[-3,3]
7	11	[-3,3]

With the creation of the lines, adiabatic effectiveness was able to be calculated and the results of the simulation with the experiments could be compared. It is worth noting, however, that by calculating the adiabatic effectiveness with $T_{rec,m}$ main flow recovery temperature equal to the mainflow temperature before the mixing of cooling flow and mainflow, all the charts generated were similar to those of the corresponding experimental, but shifted in the y-axis. It was estimated that this shift was due to some inaccuracy in the calculation of $T_{rec,m}$ (main flow recovery temperature). Therefore, by modifying this temperature by some degrees C (the maximum change of $T_{rec,m}$ was 4.6%), the final charts resulted, so as to eliminate the shift between the computed results and the reference ones.